UNIVERSITÀ DEGLI STUDI DI TORINO
Dipartimento di Fisica Sperimentale

Dottorato in Fisica Fondamentale, Applicata ed Astrofisica

XX ciclo

Thesis

The ALICE muon spectrometer: trigger detectors and quarkonia detection in p-p collisions

SETTORE SCIENTIFICO-DISCIPLINARE: FIS/04
A.A da 2004-2005 a 2006-07

Relatore:
Prof. Ermanno Vercellin

Candidato:
Martino Gagliardi

Referee esterno:
Dr. Hervé Borel

Coordinatore:
Prof. Stefano Sciuto

Contents

Introduction

This work was carried out in the context of the optimisation of the performances of the muon spectrometer of the forthcoming ALICE experiment at the Large Hadron Collider (LHC, CERN). The aim of ALICE is the study of nuclear matter at the highest energy densities ever accessed experimentally. More in detail, the focus is on the expected phase transition to a deconfined phase of matter where the degrees of freedom are those of quarks and gluons: the Quark-Gluon Plasma. The conditions for QGP formation are expected to be achieved in highly relativistic heavy ion collisions. The energy in the centre of mass of Pb-Pb collisions at the LHC will be 5.5 TeV per nucleon pair. The ALICE physics program also includes data-taking in p-p collisions at the centre-of-mass-energy of 14 TeV.

The ALICE muon spectrometer has been designed for the detection of heavy quarkonia through their muon decay: both theoretical predictions and experimental data obtained at SPS and RHIC indicate that the production of these resonances should be strongly affected by the nature of the medium formed in the collision. A high resolution measurement of the charmonium and bottomonium spectra, with significant statistics, is expected to provide crucial information to test different theoretical predictions.

The work presented in this thesis consists of two different items.

The first item is the testing of the final production of the trigger detectors for the spectrometer. The trigger system will perform a selection of muon tracks according to their transverse momentum. It consists of 72 Resistive Plate Chambers, arranged in two stations of two detection planes each. The RPCs have been tested in Torino with a dedicated test station, providing a complete characterisation (including high granularity efficiency maps) of all produced detectors and selective criteria for the validation of the final RPCs, which are now installed in ALICE.

The second item consists in the development of two different strategies for the normalisation of quarkonia yield in Pb-Pb collisions with respect to the p-p yield at the same centre-of-mass energy (5.5 TeV). This is a crucial issue

for quarkonia suppression studies. The first strategy is the direct measurement of quarkonia in p-p at 5.5 TeV: the performance of the spectrometer and the J/ψ and Υ statistics that can be obtained in a 1 month run have been evaluated by means of simulation. The second strategy is the rescaling to 5.5 TeV of the yields measured at 14 TeV, according to parametrisations for the total and differential cross sections. In this case, the uncertainties related to the extrapolation need to be carefully evaluated. The phenomenological framework adopted for the analysis of both strategies is the Color Evaporation Model for quarkonia production.

The thesis is organised as follows:

- In Chapter 1 an introduction is given to the Quark-Gluon Plasma and to the expected suppression of quarkonia resonances in the deconfined medium. An overview on quarkonia phenomenology and on the experimental results obtained by SPS and RHIC experiments on J/ψ suppression is also given.

- In Chapter 2 the ALICE experiment is described, with particular regard to the muon spectrometer and its trigger system.

- In Chapter 3 the general characteristics of Resistive Plate Chambers are described, as well as the specific options adopted for the muon trigger detectors by the ALICE collaboration in order to meet the requirements for both heavy ion and p-p data-taking.

- In Chapter 4 the tests carried out in Turin are described in detail; an analysis of the result is presented, together with the criteria adopted for the validation of the final detectors.

- In Chapter 5 the results of the efficiency tests of detectors which had previously undergone a long-term test under constant irradiation are presented. The aim of the tests is to detect any permanent effects of ageing on the detectors.

- In Chapter 6 the physics performance of the ALICE muon spectrometer for J/ψ and Υ detection in a p-p run of 10^6 s at the centre-of-mass energy of 5.5 TeV, as obtained from Monte Carlo simulation, are presented. The results obtained for the scaling factors of p-p data at 14 TeV down to 5.5 TeV are also presented, together with an estimation of the theoretical uncertainties arising from the choice of Parton Distribution Function set.

Chapter 1

Heavy quarkonia suppression by QGP in Heavy Ion Collisions

1.1 Quark-Gluon Plasma and Heavy Ion Collisions

1.1.1 The phase transition to QGP

Most of the arguments in this section are adapted from the reviews in Refs. [1, 2] and references therein.

The traditional energy scale for nuclear physics is that of the nuclear energy density:

$$\epsilon_{nuclear} = 0.15 \ \frac{GeV}{fm^3} \tag{1.1}$$

With the onset of relativistic heavy ion accelerators, high energy nuclear physics was born, extending the domain of nuclear physics. In particular, heavy ion physics studies nuclear matter under conditions of extreme density and temperature, with the aim of determining how macroscopic properties and collective phenomena emerge from the microscopic laws of particle physics, in systems with many degrees of freedom.

Matter at low energy densities is composed of protons, neutrons and electrons. If the system is heated, light mass strongly interacting particles such as pions are produced as thermal excitations. If the energy density is high enough, particles such as neutrons and protons overlap, so that their constituents (quarks and gluons) are free to roam the system without being

confined into hadrons (Fig. 1.1). Moreover, due to the asymptotic freedom of strong interactions described by Quantum Chromo-Dynamics (QCD), the interactions between quarks and gluon at this stage get weak: there is deconfinement and the system is called a Quark-Gluon Plasma (QGP).

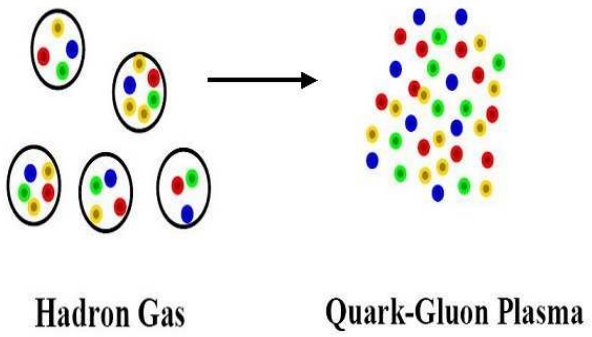

Figure 1.1: Schematic representation of the difference between the hadronic and the QGP phase. Yellow bodies represent gluons, green blue and red bodies represent quarks of the three different colours.

Quark-Gluon Plasma is believed to have existed in the early universe up to about 10^{-5} s after the Big Bang, as the system cooled down from its initial temperature[1] ($\simeq 10^{19}$ GeV) to a temperature of $\simeq 200$ MeV, and nucleons began to form from the original quark and gluon soup (Fig. 1.2).

Moreover, QGP is most likely the state of matter in the core of neutron stars and may be the origin of the phenomenon of gamma ray bursters[2]. For these reasons, the study of the properties of QGP is of great interest not only in theoretical and experimental nuclear physics, but also in cosmology and astrophysics.

The phase diagram of nuclear matter

The energy density at which the transition to QGP occurs is of the order of:

$$\epsilon_{QGP} \simeq 1 \ \frac{GeV}{fm^3} \tag{1.2}$$

[1] Temperature can be expressed in eV by means of the Boltzmann constant k = 8.63×10^4 eV/K .

[2] Gamma ray bursters are starlike objects which convert a considerable fraction of their mass into gamma rays.

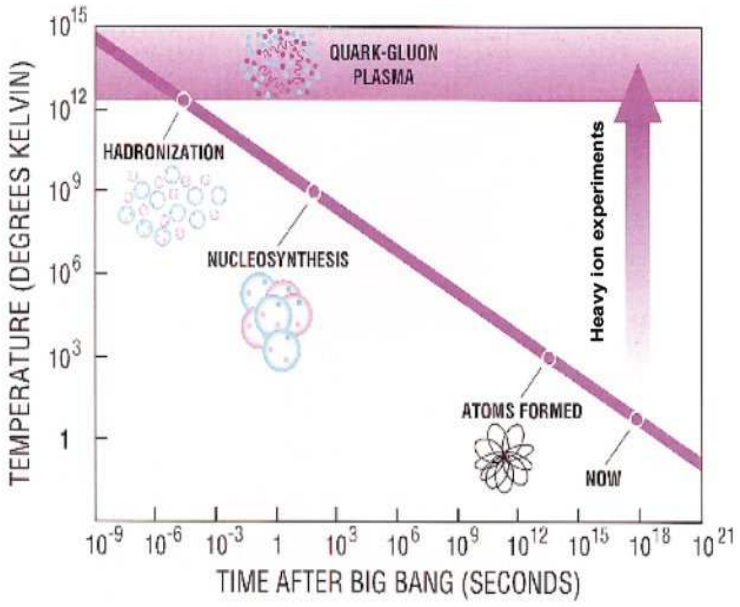

Figure 1.2: Schematic representation of the evolution of the universe from the Big Bang to our days.

At such energy density the strong coupling constant is so weak that a gas of particles can be treated with some approximation as an ideal gas. The way in which deconfinement results in a collective phenomenon such as a phase transition can be intuitively undestood by means of a simple model, called bag model, in which particles (be them hadrons or partons) are treated as a non-interacting (thus ideal) gas, confined in a limited volume[3] by an external pressure B (bag pressure). In such model, the energy density of the gas is:

$$\epsilon(T) = N\frac{\pi^2}{30}T^4 + B \tag{1.3}$$

where N is the number of degrees of freedom of the gas. For a gas of pions (chosen here to represent the confined phase) N equals to three (the possible values for the third component of the isospin), while for a gas of gluons and quarks $N=N_g+\frac{7}{8}N_q$, where:

- $N_g=8\times2$ is the number of gluon degrees of freedom (colour index and helicity);

[3]When applying the model to a heavy ion collision, such volume corresponds to the interaction region.

- N_q=3×2×2 is the number of degrees of freedom (colour, q-$\overline{q}$, spin) for each relevant quark specie (flavour);
- the factor $\frac{7}{8}$ arises from the difference bewteen the Fermi-Dirac statistics (for quarks) and the Bose-Einstein statistics (for gluons).

Thus, $N_{QGP} = 16 + 12\frac{7}{8}N_F$, where N_F is the number of relevant quark species (3 if the temperature is below the charm quark mass). It is clear that there is a difference of more than one order of magnitude between the numbers of degrees of freedom of the confined and the deconfined phase, which results in a steep rise of the ratio ϵ/T^4 in a narrow temperature range, the one in which matter undergoes a phase transition to QGP.

The phase diagram of nuclear matter can be conveniently represented in the T-μ_B plane, where μ_B is the chemical potential of the baryon number, i.e. an index of the net baryon density. Our picture of the phase diagram has evolved with time (Fig. 1.3), according to the developments of theoretical tools and the availability of experimental results. For example, the nature of the phase transition must be established: the solid lines in Fig. 1.3 represent a first order phase transition, while the dashed lines represent a rapid crossover. A n^{th} order phase transition is characterised by a discontinuity in the n^{th} derivative of some state function with respect to some thermodynamic variable, while a rapid crossover is a sudden but continuous transition.

The calculations performed to study the phase diagram of nuclear matter are different in different regions of the diagram.

Along the temperature axis, at μ_B=0, the main tool is lattice QCD, i.e. a non-perturbative theory descending from QCD's first principles such as gauge invariance, whose equations are solved numerically by discretising the space-time on a grid of finite step. According to the latest lattice calculations[3], deconfinement sets in at a temperature $T_C \simeq 190$ MeV: near such value, the ratio ϵ/T^4 increases by an order of magnitude, and at higher temperatures it settles at about 80% of the Stefan-Bolzmann value for a gas of non-interacting quarks and gluons (Fig. 1.4). At present, the phase transition along the temperature axis is believed to be a rapid crossover. For non-zero baryon chemical potential, the expectations rely on models interpolating between low-density hadronic matter, described by effective theories, and high-density QGP, described by QCD. The uncertainties in this regime are larger than those arising from lattice QCD at μ_B=0. The current expectations state that QGP at T=0 can be obtained by compressing nuclear matter to a density of $3 \div 10\rho_0$, where $\rho_0 = 0.15$ fm^{-3} is the nuclear density of ordinary matter. This density range corresponds to values of μ_B around 1 GeV. The phase transition along the μ_B axis is at present believed to be a first order transition. According to expectations, when moving along the

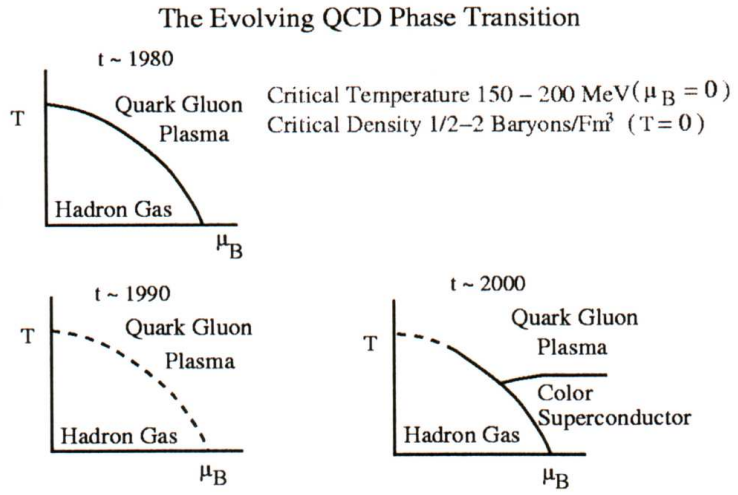

Figure 1.3: A few (time-ordered) hypotheses about the phase diagram of nuclear matter. The solid lines represent a first order phase transition, the dashed lines represent a rapid crossover.

phase transition line, there has to be a critical point at which the transition is of the second order, and beyond which it becomes a crossover (Fig. 1.5). According to the latest theoretical developments, quark matter at high densities and low temperatures should enter a phase other than QGP, analogous to the superconducting phase of solid-state physics.

Chiral symmetry restoration

Together with the transition from confinement to deconfinement, another phenomenon occurs around T_C: the restoration of chiral symmetry. Chiral symmetry is the invariance of the QCD lagrangian with 2 massless flavours (u and d) under axial transformations:

$$\psi \rightarrow e^{-i\gamma_5 \frac{\vec{\tau}\cdot\vec{\Theta}}{2}}\psi \tag{1.4}$$

One of the consequences of such a symmetry is the ρ and a_1 particles having the same mass, since they are rotated into one another by transformations of the kind 1.4. Given the very small mass of u and d quarks, such symmetry should be partially observed in nature. This does not happen[4]. The chiral

[4]The mass of the ρ is 770 MeV, the mass of the a_1 is 1260 MeV.

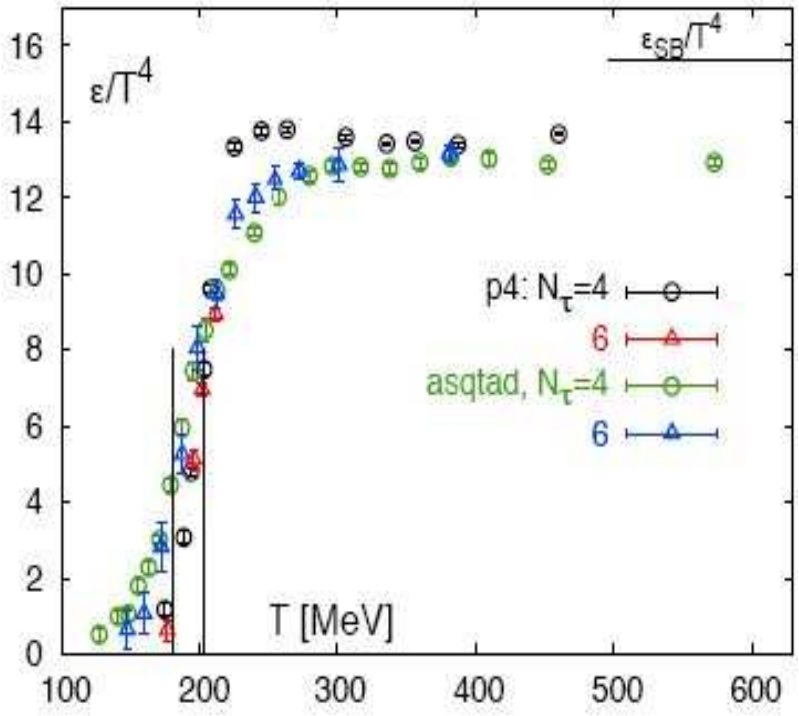

Figure 1.4: Ratio of the energy density to T^4 as a function of T, computed for nuclear matter with 2 degenerate light quarks and a heavier one, for different lattice settings. The two vertical bars mark the interval T = (192±11) MeV, while the horizontal bar marks the Stefan Boltzmann value of ϵ/T^4 for a gas of non interacting quarks and gluons. Figure is taken from Ref. [4].

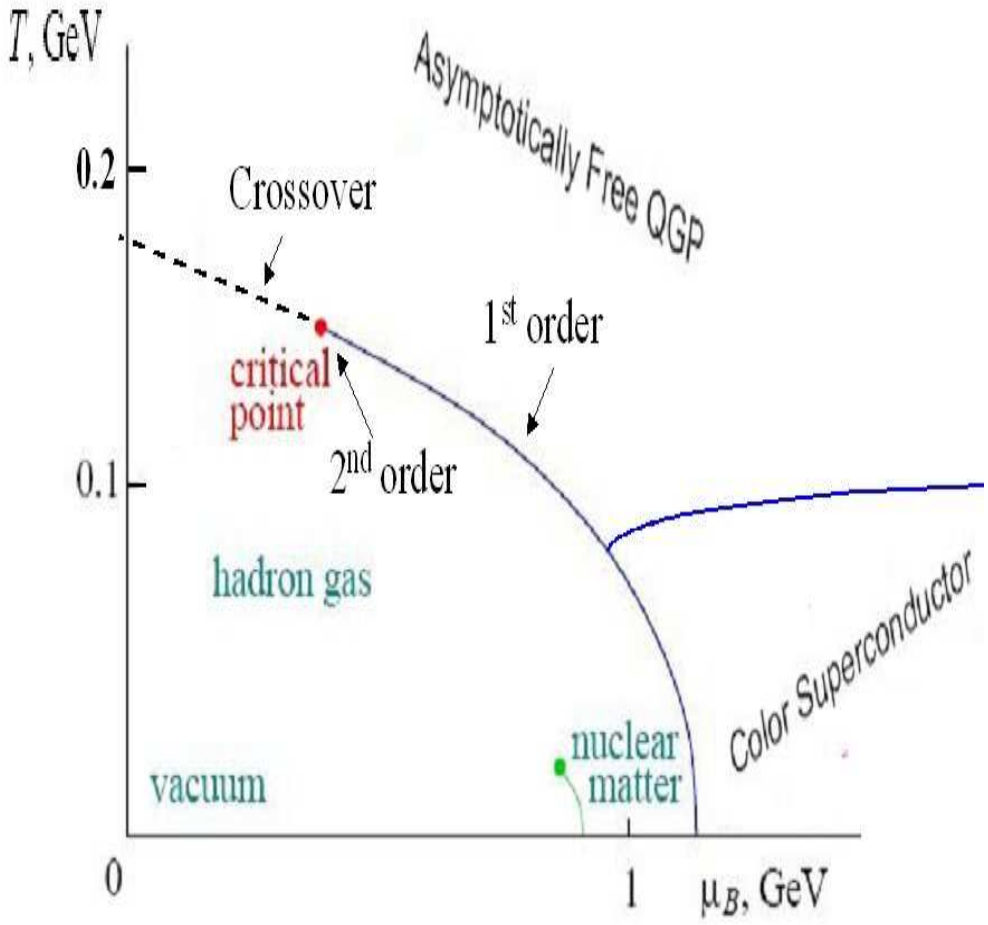

Figure 1.5: Present picture of the phase diagram of nuclear physics, including the nature of the phase transitions.

symmetry is spontaneously broken because the QCD vacuum is not symmetric with respect to chiral transformations: this is usually associated with a nonzero value of the field ψ in the ground state, i.e. at temperatures below T_C and ordinary baryon densities:

$$< \overline{\psi}\psi > \neq 0 \tag{1.5}$$

Such quantity, called the chiral condensate, is expected to vanish at higher

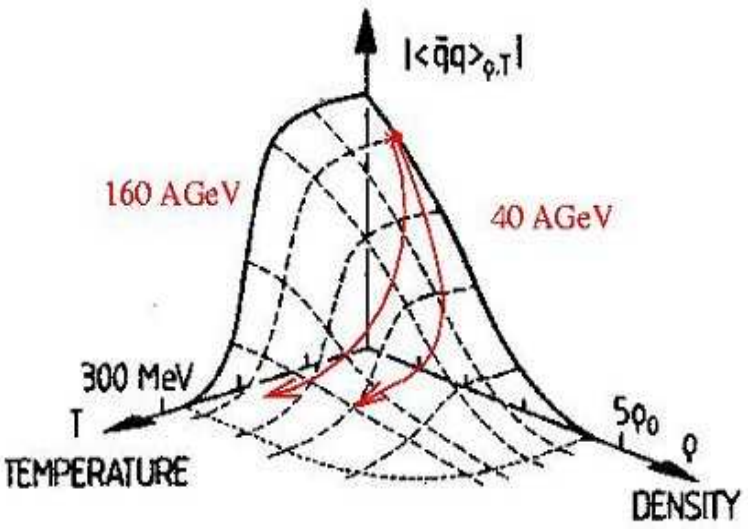

Figure 1.6: Behaviour of the chiral order parameter $< \overline{\psi}\psi >$ in the T-μ_B plane. The expected path of the system in heavy ion collisions at two different energies is also shown.

temperatures or densities (Fig. 1.6), thus restoring the chiral symmetry. Chiral symmetry restoration is expected to affect the spectral characteristics (mass and/or width) of mesons such as ρ, ω and ϕ.

1.1.2 QGP in Heavy Ion Collisions

The conditions needed to study experimentally the Quark-Gluon Plasma may be realised in central ultra-relativistic heavy ion collisions. These conditions are:

- the number of constituents of the system must be large, so that the system can be described by means of macroscopic variables; for the same reason, the size of the system must be larger than the range of strong nuclear interaction ($\simeq$ 1fm);

- the system must reach equilibrium, so that thermodynamical variables are well defined: this implies a lifetime of the system larger than the typical time-scale of strong nuclear interaction ($\simeq$ 1fm/c);
- the critical conditions for the transition to QGP are realised and held until thermalisation occurs.

Evolution of the system

The evolution in time of a high energy heavy ion collision is pictured in Fig. 1.7. It can be summarised as follows[5]:

- the two Lorentz-contracted nuclei collide: matter in an ultra-relativistic nucleus is believed to behave as a Colour Glass Condensate[5];
- pre-equilibrium (t $<$ 1 fm/c): partons scatter among each other and give rise to an abundant production of deconfined quarks and gluons;
- thermalisation and QGP: (1 fm/c $<$ t $<$ 10 fm/c): matter reaches equilibrium, QGP forms: the degrees of freedom here are those of quarks and gluons;
- mixed phase: the system, while expanding, begins to convert into a hadron gas;
- hadronisation: (t $\simeq$ 20 fm/c): quarks and gluons are again confined into hadrons;
- chemical freeze-out: inelastic interactions bewteen hadrons cease, relative abundances are fixed;
- thermal freeze-out: elastic interactions between hadrons cease, kinematical spectra are fixed.

Energy density

The determination of the energy density reached in the stages mentioned above is not straightforward; the most used definition was given by Bjorken in 1983[6]:

$$\epsilon_{Bj} = \frac{1}{Ac\tau_f}\frac{dE_T}{dy} \tag{1.6}$$

[5]The timescales reported should be considered indicative, since their precise determination is still uncertain and model-dependent.

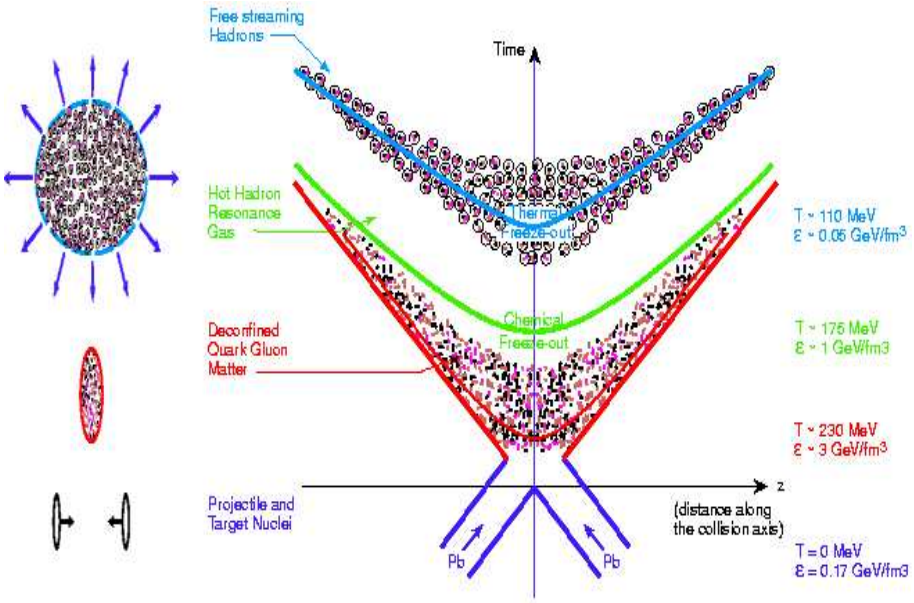

Figure 1.7: Space-time evolution of a Pb-Pb collision.

where A is the transverse area of the interaction region, dE_T/dy is the transverse energy per rapidity unit at mid-rapidity (i.e. an experimentally accessible quantity) and τ_f is the formation time of secondary particles. Such formula gives an estimate for the energy density in a central Au-Au collision at $\sqrt{s} = 200$ GeV per nucleon pair[6] of about 15 GeV/fm^3. It has to be pointed out that this value refers to the the inital energy density, i.e. the one available when secondary particles are formed but matter is not thermalised. A more relevant quantity for the purposes of studying QGP is obtained by inserting in Eq. 1.6, instead of τ_f, a realistic guess for the thermalisation time in the above described conditions, i.e. $\tau_{th} \simeq 1$ fm/c. This leads to an energy density of about 5 GeV/fm^3, still larger than the critical value of 1 GeV/fm^3 (Fig. 1.8): the possibility to reproduce QGP in a laboratory is more than a mere hypothesis.

A very brief review of the main relativistic heavy ion beams

The above considerations represent a simplified picture of how the transition to QGP can be realised in a laboratory, but nevertheless they can be used to compare the main relativistic heavy ion beams that have been running so

[6]This is the energy of Au-Au collisions at the Relativistic Heavy Ion Collider which will be mentioned in the following paragraph.

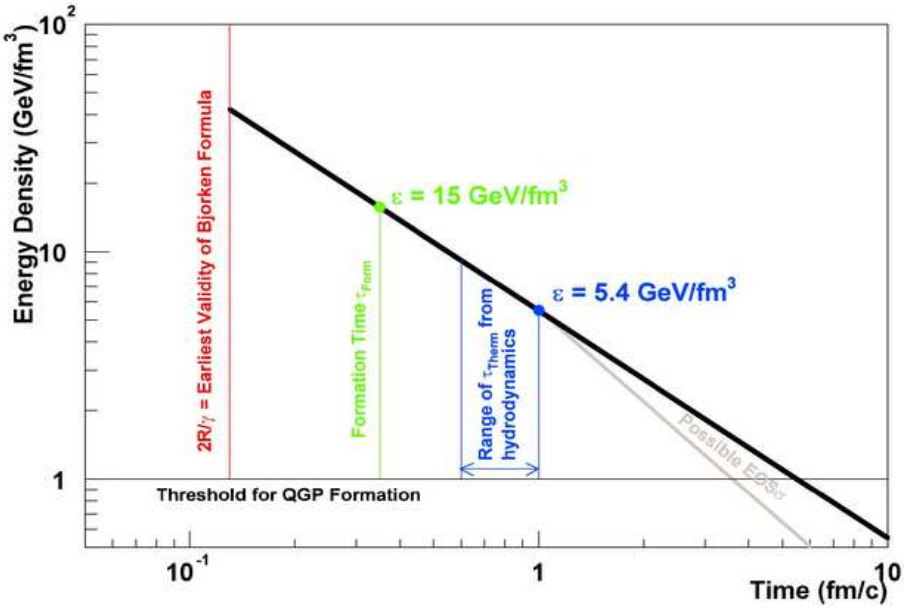

Figure 1.8: Energy density as a function of time in a central Au-Au collision at $\sqrt{s} = 200$ GeV per nucleon pair, according to Eq. 1.6.

far. These are:

- Alternating Gradient Synchrotron (AGS), running from 1986 to 2000 at the Brookhaven National Laboratories. It accelerated Si and Au ions up to 14.6 GeV per nucleon, on a fixed target. The energy per nucleon pair of Au-Au collisions was 5 GeV.

- Super Proton Synchrotron (SPS), running from 1986 to 2003 at CERN (Geneva). It accelerated O, S, In and Pb ions up to 200 GeV per nucleon, on a fixed target. The energy per nucleon pair of Pb-Pb collisions was 17 GeV.

- Relativistic Heavy Ion Collider (RHIC) at the Brookhaven National Laboratories. It has accelerated Cu and Au ions up to 100 GeV per nucleon, in collider mode, so that the energy per nucleon pair in Au-Au collisions is 200 GeV.

While the heavy ion program at AGS and SPS was secondary (in terms of running time) with respect to the proton program for which the machines were designed, RHIC was designed specifically for heavy ion collisions.

The values of the energy density at t=1 fm/c for the three machines, calculated according to Eq. 1.6, are shown in Tab. 1.1. It appears that

in all cases the energy density is higher than 1 GeV/fm^3. This does not automatically mean that the energy density at thermalisation is above the critical value for all systems, since the crossing time of the nuclei at AGS and SPS exceeds 1 fm/c.

Machine	System	$\sqrt{s}_{NN}$ (GeV)	ϵ_{Bj} (GeV/fm^3)
AGS	Au-Au	5	1.5
SPS	Pb-Pb	17	2.9
RHIC	Au-Au	200	5.4

Table 1.1: Energy density at t=1 fm/c for central A-A collisions, according to the Bjorken formula, for different colliding systems.

A discussion of the results obtained by the experiments at these machines is way beyond the scopes of this work. Nevertheless, it is worth mentioning that, while AGS showed no evidence for the formation of the deconfined phase (though the results indicate the creation of strongly interacting nuclear matter), experiments at both SPS and RHIC claimed the discovery of the new state of matter[7, 8, 9]. While the heavy ion community agrees that some form of QGP was seen at RHIC and SPS, there is much debate about what the characteristics of such QGP are: the only way to answer the question is the analysis of the available experimental probes.

1.1.3 Experimental probes of QGP formation

The short lifetime of QGP as created in laboratory (a few fm/c) and the hadronisation of quarks and gluons long before they reach the detectors, make the direct observation of the QGP-phase impossible. The nature of QGP must be investigated by means of observables that retain information about the nature of the medium that was formed during the collision. In this section the main experimental probes of QGP will be briefly reviewed.

The main classification of experimental probes relies on the difference between hard probes (i.e. probes produced during the primary collisions, that are somehow sensitive to the nature of the medium they have to cross before being detected) and soft probes (probes produced during the evolution of the system, which reflect the collective properties of the medium).

Soft probes: flow and the equation of state

As pointed out in Sec. 1.1.1, the phase transition to QGP must imply a sudden change in the behaviour of quantities such as entropy, energy density

and pressure as a function of thermodynamical variables such as the baryon chemical potential or the temperature. To monitor the equation of state, the above mentioned quantities must be inferred from measured quantities. It has already been shown how the energy density can be estimated from an experimental quantity such as the total transverse energy per unit of rapidity of the particles produced in the collision. Information about the evolution of the system can be drawn from the kinematical spectra of particles: these can be fitted according to hydrodynamic models, or integrated to get the total abundancies and relative ratios of particle species, which can be compared to thermal models of particle production to extract parameters such as T and μ_B.

The analysis of particle spectra also gives information about the collective motion of particles (flow), due to the expanding fireball of nuclear matter created in the collision. In particular, due to the asymmetric shape of the fireball in semi-central and peripheral collisions (Fig. 1.9), the expansion is not isotropic and an elliptic flow due to the pressure gradients in the fireball can be observed. The variables related to the elliptic flow are particularly sensitive to the equation of state of the system during the first stage of its evolution, thus can be used to distinguish between hadronic and partonic expansion models (Fig. 1.10) and to estimate the timescale of thermalisation.

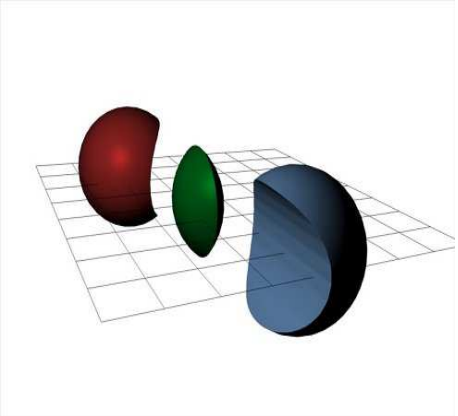

Figure 1.9: The asymmetric initial geometry of the fireball created in a heavy ion collision at nonzero impact parameter.

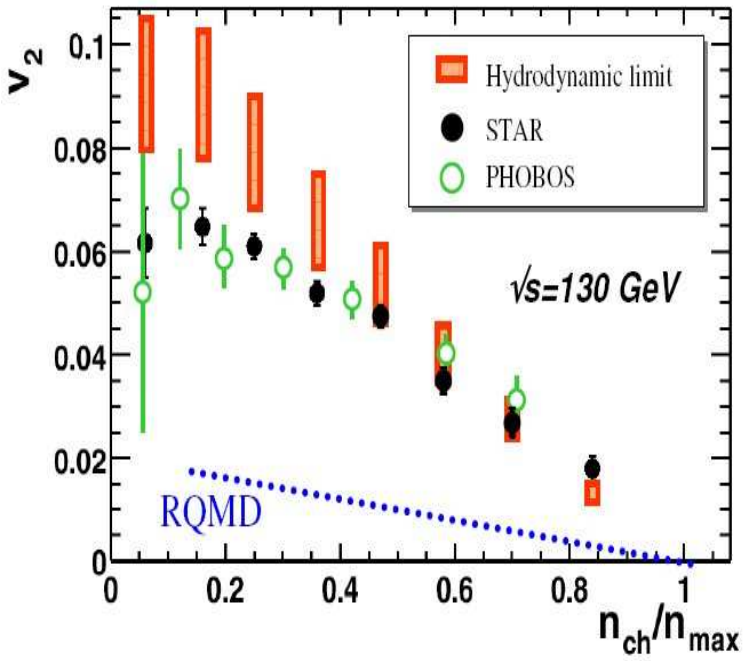

Figure 1.10: Elliptic flow (quantified by the v_2, i.e. the second order coefficient of the Fourier expansion of the azimuthal distribution of the emitted particles) versus number of charged particles (an index of the collision centrality) in Au-Au collisions at RHIC, compared with hydrodynamics expectations and with the RQMD hadronic cascade model.

Soft probes: strangeness enhancement

The production of strange particles in a hadronic environment is strongly suppressed with respect to lighter flavours, due to the higher mass of the s quark[7], which results in higher production thresholds. In a deconfined medium, strange quarks are abundantly produced via the gg$\rightarrow s\overline{s}$ (gluon fusion) process; subsequently, they survive until hadronisation occurs. This results in a higher yield of strange hadrons such as Ξ (qss) and Ω (sss), which can be taken as evidence for deconfinement[10]. Strangeness enhancement is observed already at SPS energies[11]: the yield per event obtained in Pb-Pb collisions is higher than what one would obtain from a simple superimposition of p-Pb collisions (Fig. 1.11).

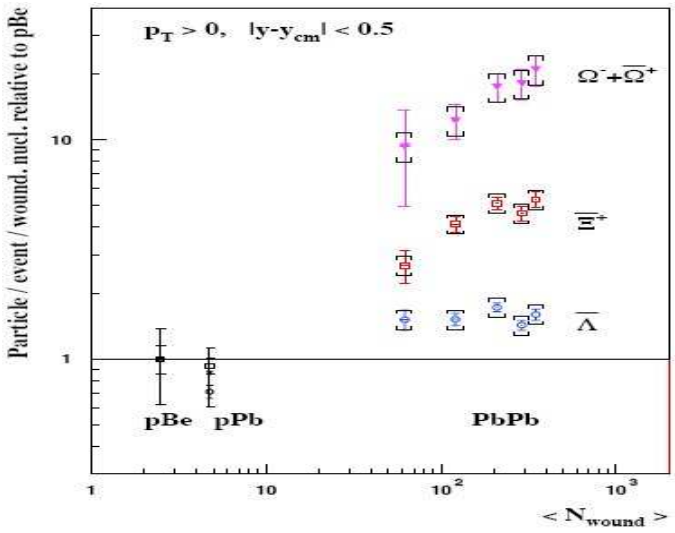

Figure 1.11: Yields of strange particles per event per colliding nucleon, as a function of the number of colliding nucleons, in p-Be, p-Pb and Pb-Pb collisions at 158 GeV per nucleon, normalised to the p-Be yield, as measured by the NA57 experiment.

Electromagnetic probes: photons and dileptons

Electromagnetic probes are of great interest, since they interact very weakly with the medium they cross, thus carrying with them information about the stage at which they were produced.

[7] $m_u \simeq 1.5 \div 4$ MeV/c^2, $m_d \simeq 4 \div 8$ MeV/c^2, $m_s \simeq 80 \div 130$ MeV/c^2.

Photons are produced throughout the whole expansion of the fireball. The main production mechanisms of photons are:

- prompt photons produced in the hard scatterings of parton in the primary collision;
- thermal radiation from the QGP at equilibrium, with an energy spectrum that extends up to the GeV region;
- photons produced by scatterings in the hadron gas, between the hadronisation phase and the chemical freeze-out, with an energy spectrum between a few MeV and several GeV;
- photons produced by resonance decays after freeze-out.

The second kind of photons is the more interesting, since it gives information about the temperature of the deconfined medium. The correct identification of photons of all kinds is mandatory to analyse the thermal emission from QGP. The contribution from final-state decays is usually subtracted from the spectrum to obtain what is defined as direct photon spectrum (Fig. 1.12).

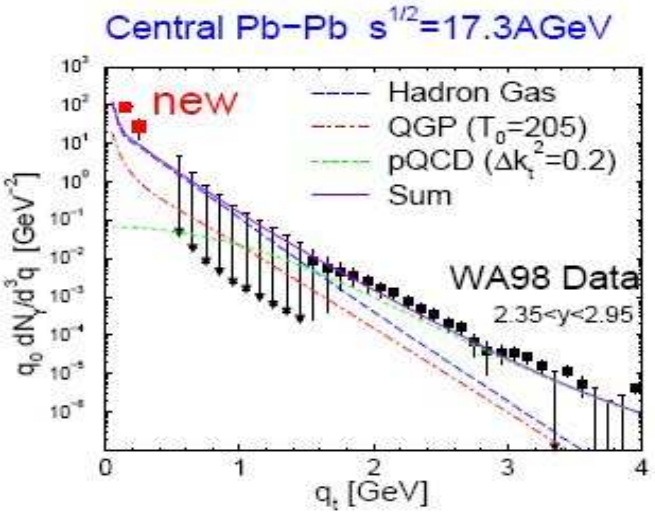

Figure 1.12: Direct photon spectrum in Pb-Pb collisions from the WA98 experiment at SPS, compared to the calculations for thermal emission from an expanding fireball and for prompt (pQCD) photons.

Lepton pair production from the expanding fireball proceeds through similar stages as those mentioned above for photons. While the dilepton spectrum at low invariant masses ($M_{\mu\mu}$ <1 GeV) is dominated by the decays

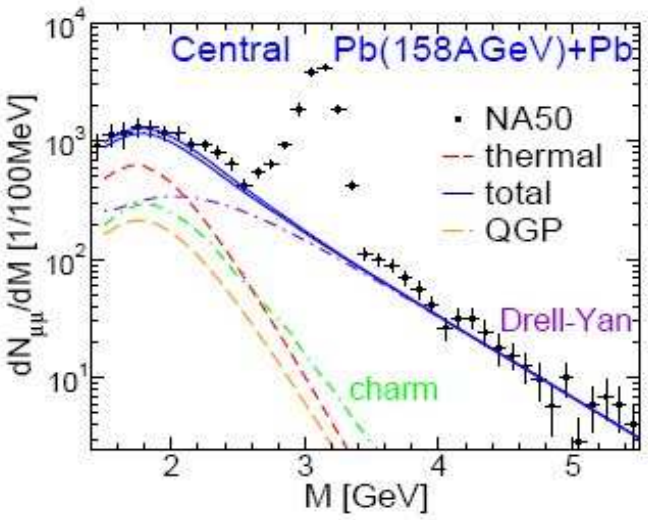

Figure 1.13: Dimuon spectrum in Pb-Pb collisions from the NA50 experiment at SPS, compared to the calculations for the expected sources.

of light vector mesons produced in the hot hadronic phase (which will be discussed in the next paragraph), the spectrum in the intermediate mass region can be fitted according to thermal production mechanisms from both the hadronic and the QGP phase (Fig. 1.13). Another important dilepton source in this region is the decay of open charm mesons. The high mass region ($M_{\mu\mu}$ >2.5 GeV) is dominated by heavy charmonium decays (which will be discussed extensively in the following section) and, at even higher masses, by the decays of open and hidden beauty mesons. Another important source of dileptons in the intermediate and high mass region is the Drell-Yan process, which, since it is an all-electromagnetic process, provides a useful normalisation tool for medium effects.

Probes of chiral symmetry restoration

As it was mentioned in Sec. 1.1.1, the QGP phase is expected to be characterised by chiral symmetry restoration. One of the concrete effects of such phenomenon is the expected change of the spectral characteristics of mesons such as ρ, ω and ϕ. The most interesting among these is the ρ, since:

- it has a well defined partner under chiral transformations (the a_1);
- given its short lifetime (Γ=149 MeV), it mostly decays within the interaction region, so that the dilepton pair originating from the decay car-

ries information about the spectral characteristics of ρ in the medium.

Expectations about the possible effects of chiral symmetry restoration on the ρ width and mass are not univocal. The predictions range from the complete mixing of the ρ with the a_1 to the disappearance of the resonant structures.

The recent results[13] from the NA60 experiment at SPS seem to prefer the Rapp-Wambach hadronic scenario[12], which predicts a broadening of the ρ resonance, with no mass shift (Fig. 1.14).

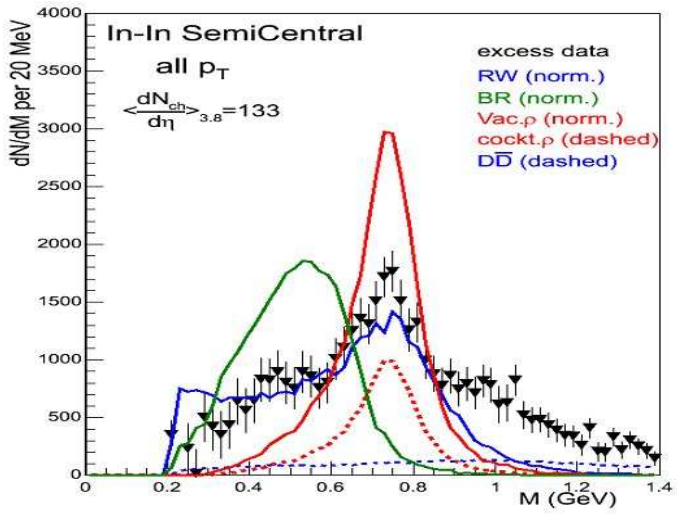

Figure 1.14: Invariant mass spectrum of dimuon pairs in the region of the ρ resonance, as measured by NA60 in In-In collisions at 158 GeV per nucleon.

Hard probes: high p_T hadrons, jets and quarkonia suppression

The presence of the medium affects the production of hadrons from initial parton scatterings. A parton crossing a coloured medium loses energy by means of two mechanisms:

- collisional energy loss due to scattering with other partons;
- radiative energy loss (gluonstrahlung).

The dominant mechanism at high energies is the radiative one.

A parton created in the hard collision, on a timescale short with respect to the evolution of the system (e. g. a heavy or high p_T quark) is slowed

down by energy loss. This results in the quenching of the hadron spectrum at high p_T (Figs. 1.15(a) and 1.15(b)). The RHIC results are compatible with the hypothesis of surface emission, i.e. the only high p_T hadrons are those emitted from the peripheral regions of the fireball, which do not have to cross the entire medium. More information can be obtained by analysing

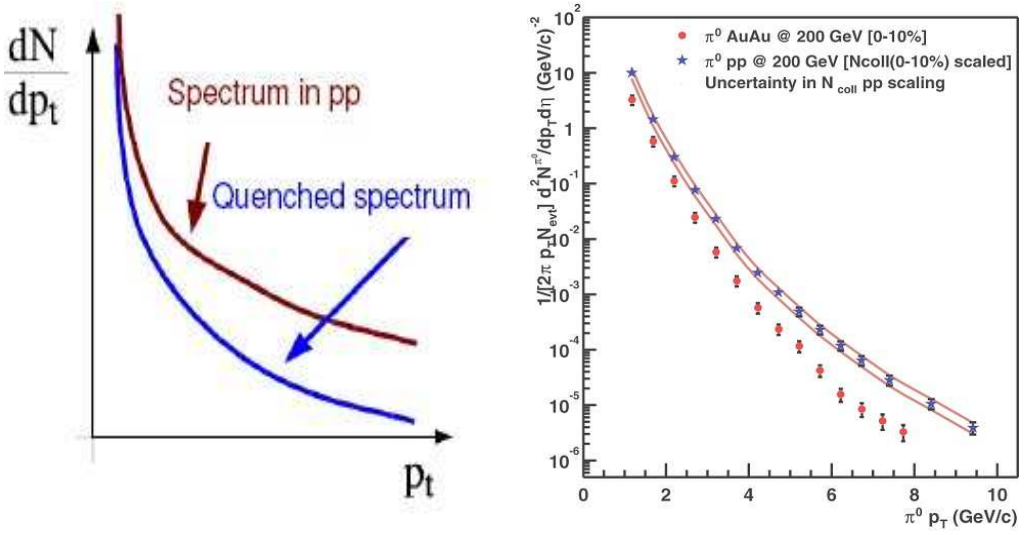

(a) (b)

Figure 1.15: Quenching of high p_T hadronic spectrum in central heavy ion collisions (a); π^0 p_T distribution, as measured by PHENIX in central Au-Au collisions, compared to the one measured in p-p collisions multiplied by the number of binary collisions(b).

azimuthal correlations between the produced particles. When triggering on a high p_T particle, the azimuthal distribution of the other particles with respect to the triggered one should exhibit two peaks at 0 (near-side jet) and π (away-side jet) radians, since, at least at Leading Order, parton pairs are produced back-to-back, and the hadron jets retain information about the direction of the initial parton from which they originated via fragmentation. In a coloured medium, the high p_T particle is most probably emitted from the surface of the fireball, so that the parton from which the away-side jet originates has to cross the whole medium: this results in a suppression of the away-side jet in central nucleus-nucleus collisions (Fig. 1.16).

The presence of a coloured medium affects the bound states of heavy quarks: colour screening of the binding potential by partonic matter results

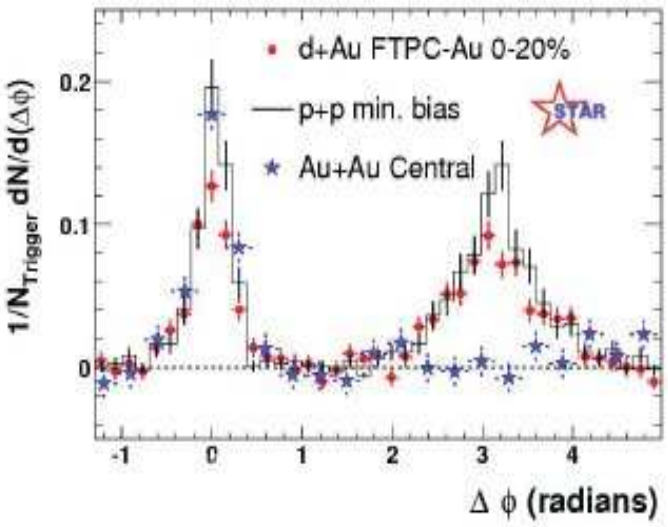

Figure 1.16: Two-particle azimuthal correlations in p-p, d-Au and central Pb-Pb collisions at RHIC.

in the suppression of particles such as J/ψ and Υ. This topic will be covered more in detail in the next section, since the ALICE muon spectrometer at the Large Hadron Collider (CERN), which is the subject of this work, was primarily designed for the detection and analysis of heavy quarkonia.

1.2 Quarkonia suppression as a signature of QGP formation

1.2.1 Charmonium and bottomonium states

Spectroscopy

The ground states of heavy quarkonium vector resonances are rather stable particles: due to their mass below the threshold for open heavy flavoured meson pair production, their decay modes are either electromagnetic (about 30%) or OZI-suppressed (about 70%). The ground state for $c\bar{c}$ vector mesons is the J/ψ (M=3.1 GeV, Γ=91 keV), while the ground state for $b\bar{b}$ vector mesons is the Υ (M=9.5 GeV, Γ=53 keV). The excited states below the open charm (beauty) threshold have widths ranging from a few tens of keV to a few hundreds of MeV. The spectroscopy of heavy vector quarkonium states is shown in Figs. 1.17(a) and 1.17(b).

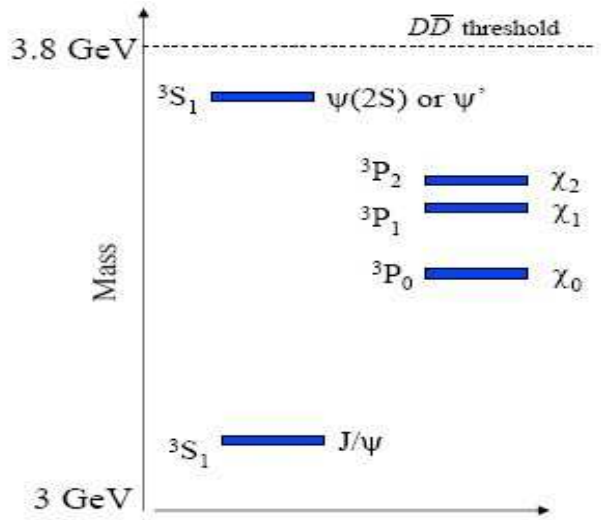

(a)

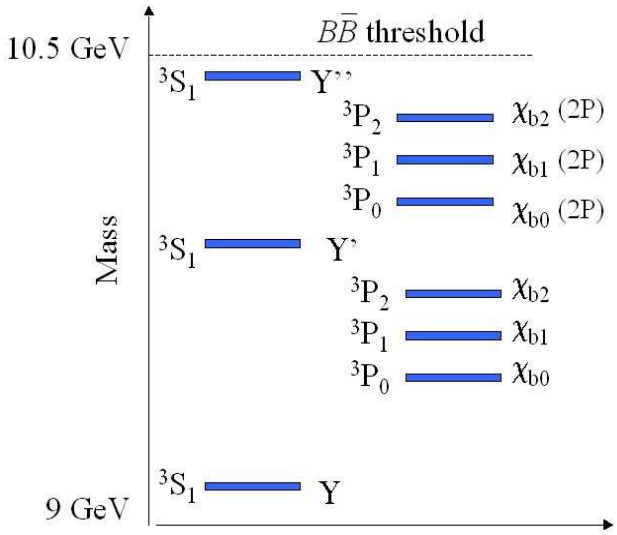

(b)

Figure 1.17: Spectroscopy of charmonium (a) and bottomonium (b) vector resonances below the open heavy flavoured meson pair production threshold.

Given their high mass, the motion of c and b quarks within the bound state is non-relativistic ($\beta \simeq 0.4$) and non-perturbative, hence the difficulties in describing the production mechanism and the dynamics of quarkonium states.

The spectroscopy of quarkonia is phenomenologically described by assuming that the $Q\overline{Q}$ pair is subject to the Cornell potential, consisting of a Coulomb-like term accounting for gluon-exchange between the two quarks and a confining term parametrising the non-perturbative effects:

$$V(r) = -\frac{\alpha}{r} + kr \tag{1.7}$$

The results obtained by solving the Schrödinger equation with the potential 1.7 (and ad-hoc values of the parameters) are in fair agreement with the observed spectra.

Production mechanism

Given the non-perturbative nature of quarkonium production, the issue of quarkonium production mechanism is still an open research field. Earlier experiments ruled out the hypothesis of electromagnetic production via $q\overline{q}$ annihilation, since it was shown that the production rate of J/ψ is identical in π^+-N and π^--N collisions (the difference in electric charge between the u and d quarks should suppress the production in π^+-N collisions by a factor 4). Similarly, the hypothesis of $q\overline{q}$ annihilation into a gluon was rejected after the comparison between p-$\overline{p}$ and p-p collisions (here, the difference between the $\overline{q}$ content of proton and antiproton should lead to a suppression in p-p by a factor $5 \div 10$, which is not observed). Thus, it is an accepted opinion in the scientific community that quarkonium production proceeds mainly via the gluon fusion process (gg$\rightarrow Q\overline{Q}$).

In this section the main theoretical and phenomenological models for quarkonium production developed so far will be briefly recalled. All of the models share the common concept of factorisation, i.e. a procedure that separates the perturbative approach to the hard process leading to the production of a $Q\overline{Q}$ pair from the non-perturbative description of hadronisation into a bound state with given quantum numbers.

The Color Singlet Model was the first to be proposed: it simply states that the production of quarkonia only occurs when the $Q\overline{Q}$ pair generated in the hard collision has the correct quantum numbers: in particular, it must be produced in a color singlet state, so that all color-octet terms in the perturbative expansion must be dropped. CSM was ruled out by theoretical inconsistencies when dealing with P-wave or higher angular momentum

states, and by failure to reproduce the data[14] obtained in 1995 at the Tevatron collider at Fermilab ($\sqrt{s}$ =1.8 TeV): the discrepancy was of more than one order of magnitude.

The Color Evaporation Model[15] is a purely phenomenological model which dates back to the '70s. The basic concept behind CEM is that the number of produced quarkonia is some fraction F_C (different from specie to specie) of the number of $Q\overline{Q}$ pairs produced below the threshold for open heavy flavour production, regardless of spin and colour: the cross section can be obtained from the heavy quark pair production cross section, with a cutoff on the centre-of-mass energy of the hard collision, which must be lower than $2m_H c^2$ (m_H is the mass of the D meson for charmonium and of the B meson for bottomonium). The assumption of the CEM is that the $Q\overline{Q}$ pair neutralises its colour by interacting with soft degrees of freedom in the colour field created during the collision, hence the concept of colour evaporation. The same colour field can supply the energy needed to create open heavy flavoured mesons even when the pair mass is below the threshold: for this reason the value of F_C is quite small, of the order a few percent. In order for the model to have some predictive power, F_C must be independent of the collision energy and of all kinematical variables: this requirement was shown to be respected up to Tevatron energies[16] (Fig. 1.18). More quantitative details about the CEM cross sections will be given in Chap. 6, since such model was chosen to analyse quarkonia detection in the ALICE muon spectrometer.

Non Relativistic QCD[17] couples the usual relativistic field theory for the short-distance processes involving light quarks and gluons with a non-relativistic quantum field theory which describes the long-distance heavy quark-antiquark dynamics. The short-distance process is treated by means of perturbative expansion in $\alpha_S(m_Q)$, which at the c and b mass scales is of the order of 0.2; the non-perturbative part is treated by means of the matrix elements of 4-fermion operators in non-relativistic field theory: the physical meaning of such matrix elements is essentially the probability for a $Q\overline{Q}$ pair with given quantum numbers to produce a given quarkonium state. The matrix elements are organised into a hierarchy according to their scaling with v, the typical velocity of the heavy quark ($v^2 \simeq 0.3c^2$ for charmonium, $v^2 \simeq 0.1c^2$ for bottomonium). NRQCD is more than a phenomenological model, since it is the rigorous limit of QCD when Λ_{QCD}/m_Q gets small. Its predictive power relies on the fact that the matrix elements are universal, i.e. process independent. NRQCD predictions shows good agreement with data up to Tevatron energies. Problems remain in the treatment of quarkonium polari-

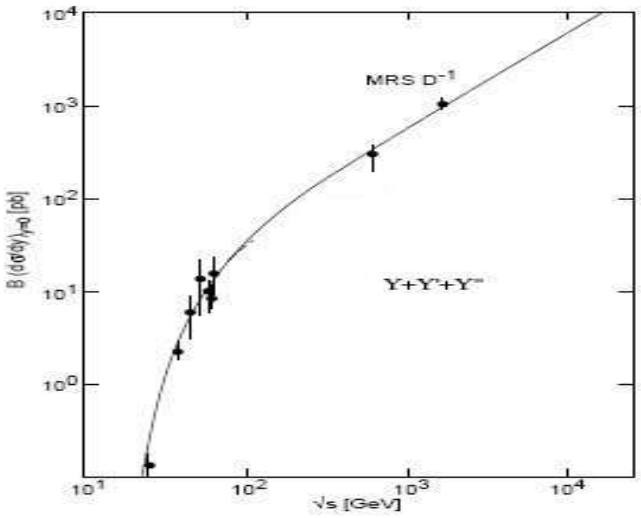

Figure 1.18: Energy dependence of $(\mathrm{d}\sigma/\mathrm{dy})_{y=0}$ for Υ production in p-N collisions. The CEM predictions are compared to data coming from different experiments. The higher energy point is from CDF.

sation by NRQCD.

The Comover Enhancement Scenario is a model which states that the $Q\overline{Q}$ pair acquires its quantum numbers by interaction with the comoving colour field created in the hard collision, on a timescale larger than that of the hard process, but still perturbative and compatible with the DGLAP equation. The introduction of a perturbative time-scale for the neutralisation of the colour of the $Q\overline{Q}$ state is a feature that is not present in all other models cited here.

1.2.2 Quarkonia suppression by QGP

The suppression of heavy quarkonia production in a deconfined medium was first discussed in 1986[18]. The prediction is based on the screening effect of deconfined colour charges on the $Q\overline{Q}$ binding: since the formation of quarkonium resonances happens on timescales compatible with the formation of the plasma, these can not escape the medium before the deconfined phase, thus it makes sense to analyse what the effect of deconfinement is on the quarkonium state.

When the temperature reaches the critical value T_C, deconfinement sets in and the confining term in the Cornell potential 1.7 disappears. Moreover,

the Coulomb-term must be modified to take into account colour screening of the potential, which becomes:

$$V(r) = -\frac{\alpha}{r} e^{-\frac{r}{r_D}} \tag{1.8}$$

where r_D is the Debye screening radius, i.e. a quantity which roughly corresponds to the distance at which the two quarks can not "see" each other because of colour screening. The screening radius decreases with increasing temperature: its estimation is mainly based on Lattice QCD calculations, which indicate a behaviour proportional to $T^{-1/2}$. When minimising the energy of the bound state as a function of the resonance radius, using the potential 1.8, one finds a minimum value of r_D for which there is a solution, i.e. there is a value of R_D below which the resonance can not form, thus a temperature above which the resonance is suppressed (Fig. 1.19) and the two heavy quarks travel in the medium without binding until hadronisation, when they eventually combine with light quarks to form open charm (beauty) mesons.

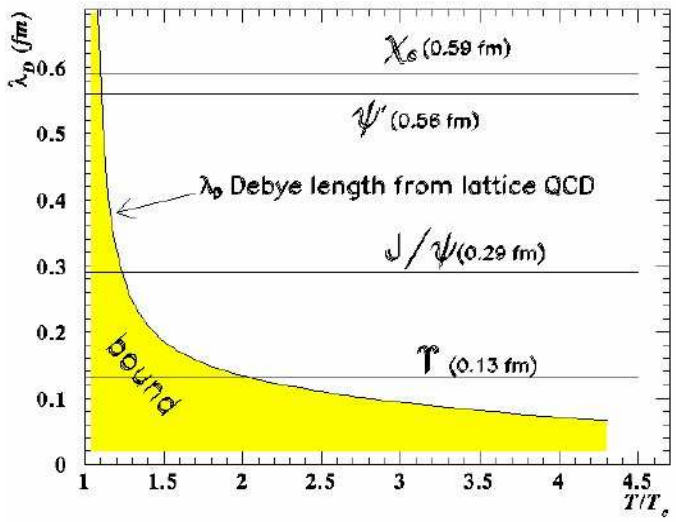

Figure 1.19: Debye screening radius in a deconfined medium, as a function of T/T_C, compared with estimates for the radius of a few quarkonium resonances.

Since different quarkonium resonances have different binding energies, and thus different dimensions, it is expected that those states who are less tightly bound should melt at lower temperatures: the sequential suppression

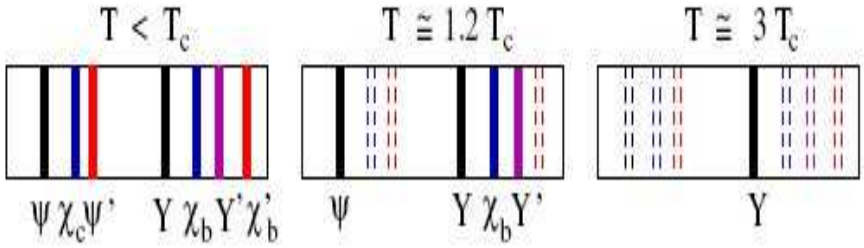

Figure 1.20: Quarkonium spectral lines as a thermometer for the plasma. Dashed lines represent suppressed resonances.

of resonances may be interpreted as a "thermometer" for the plasma[19], as pictured in Fig. 1.20.

The theoretical efforts are now concentrating on determining the exact temperatures at which the different resonances melt. In time, the progresses of Lattice QCD put stronger constraints on the values of the screening radius at T_C and above; moreover, they supplied new potential parametrisations for the $Q\overline{Q}$ potential to be used in the Schrödinger equation for the bound state. The studies were carried out with particular attention to charmonium states, since most of the experimental data in this field of interest refer to J/ψ mesurements (see Sec. 1.2.3). The present knowledge about the melting of charmonium states is summarised in Tab. 1.2: it appears that, while the ψ' and χ_c resonances should melt around T_C, the J/ψ should survive up to $T \simeq 2T_C$.

State	J/ψ (1S)	χ_c (1P)	ψ' (1S)
T_D/T_C	2.1	1.2	1.1

Table 1.2: Dissociation temperatures of charmonia in a deconfined medium, according to the present theoretical estimates.

Finally, there now exist direct finite temperature LQCD studies of the in-medium behaviour of charmonia, allowing *ab initio* calculations not based on any potential model (i.e. on the assumption that a two-body treatment around T_C is possible). These seem to support a higher J/ψ dissociation temperature.

While the argument of quarkonia suppression in a deconfined medium lies on solid theoretical bases, nevertheless the validation of predictions against

the experiment is not straightforward, since there exists a set of concurrent or alternative phenomena which may blur the picture. These include:

- cold nuclear matter effects affecting the quarkonia yield in both the initial state (e.g. shadowing of the Parton Distribution Functions in the nucleus) and the final state (nuclear absorption); these are somewhat known effects that can be taken into account in the analysis of data;
- quarkonia suppression in a pure hadronic scenario, e. g. by hadronic comovers;
- quarkonia regeneration phenomena.

A few of these items will be discussed in the next section.

1.2.3 Experimental results on quarkonia suppression

In this section a few experimental issues related with the study of J/ψ suppression will be discussed, and selected results on J/ψ suppression will be summarised. Results on bottomonium states so far are scarce, due to a smaller production cross section.

The preferred channel in which J/ψ was studied is through its dilepton decays: the branching ratio is similar for e^+e^- and $\mu^+\mu^-$: it amounts to about 6%.

The J/ψ suppression pattern

Infomation about suppression mechanisms can be obtained by measuring the J/ψ yield per nucleon collision as a function of the centrality of the collision. In absence of suppression mechanisms, the yield per nucleon collision should be independent of the number of collisions. The number of nucleon collisions for a given centrality can be obtained from the Glauber model[20]. A few experiments have chosen to study (as a function of centrality) the ratio of the J/ψ yield to the Drell-Yan yield, since the latter process is not affected by the medium and its measurement is affected by similar experimental systematics (acceptance, trigger and so on) as those affecting the measurement of J/ψ dileptonic decays: such systematics cancel when computing the ratio.

As pointed out at the end of Sec. 1.2.2, cold nuclear matter effects affect the J/ψ yield, causing what is called a normal suppression. Such phenomena include the absorption of the pre-resonant $c\overline{c}$ pair by nuclear matter in the colliding nuclei: this effect, usually referred to as nuclear absorption, can be parametrised with a phenomenological absorption cross section σ_{abs}, so that:

$$\sigma(AB \to J/\psi) \propto ABe^{-\rho_0 \sigma_{abs} L} \tag{1.9}$$

where A and B are the numbers of nucleons in the two colliding nuclei, ρ_0 is the ordinary nuclear density and L is the length of the path of the $c\overline{c}$ pair through nuclear matter, which can be calculated from the impact parameter b. The value of σ_{abs} is usually obtained experimentally from p-A or d-A collisions, where only normal J/ψ suppression is possible.

Overview of experimental results so far

The main results on quarkonia suppression come from the NA38 (later upgraded to NA50 and NA60, Fig. 1.21) experiment at SPS and from the PHENIX experiment at RHIC.

The NA38 experiment measured J/ψ production in O-U and S-U collisions (200 GeV/nucleon) by means of a dedicated muon spectrometer: a factor 2 suppression of the J/ψ yield (normalised to the underlying continuum) from peripheral to central collisions was observed[21]. It was shown that such suppression was compatible with nuclear absorption[22].

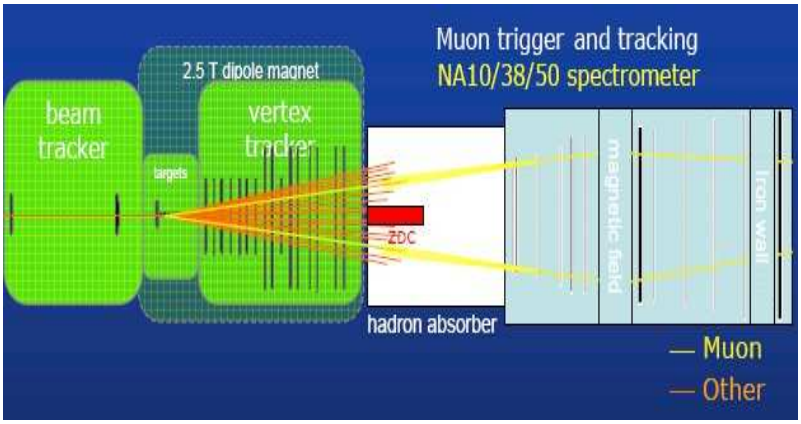

Figure 1.21: Common design of the NA10-NA38-NA50-NA60 experiments. The vertex tracker was only added with the upgrade to NA60.

The NA50 experiment took data in heavier ion collisions, such as Pb-Pb, where the energy density created is bigger: a deviation of a few σ from the normal suppression pattern was indeed observed[23]. The suppression pattern obtained by NA50 is shown in Fig. 1.22, together with the NA38 data and their extrapolation according to the nuclear absorption pattern.

The NA50 experiment was later upgraded to NA60 by adding a vertex tracker (Fig. 1.21), drastically improving the mass resolution and the rejection of background. The results[24] obtained by NA60 in In-In collisions confirm the suppression observed by NA50, with an onset of the suppression

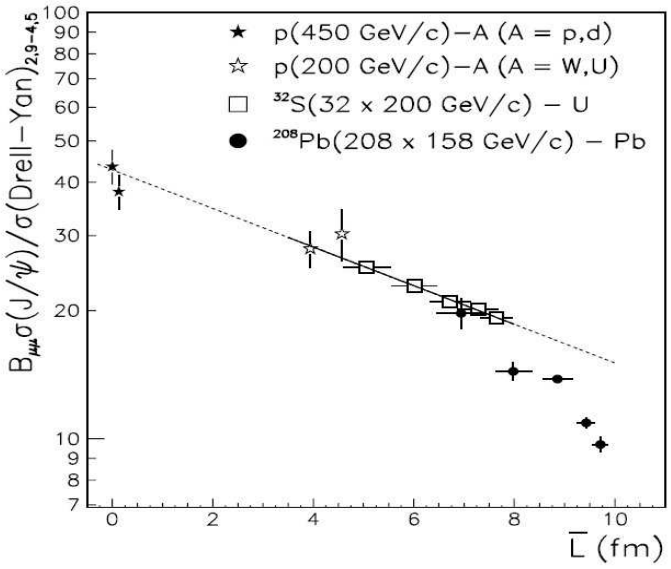

Figure 1.22: Ratio of J/ψ to Drell-Yan cross section as a function of the path length L, as measured by the NA38 and NA50 experiments. The fit of small-L data according to Eq. 1.9 is also shown.

at an energy density around 1.5 Gev/fm^3. Models predicting J/ψ suppression by comovers in an expanding hadronic gas fail to account for the entity of the observed suppression.

The start-up of RHIC opened the way to a new energy domain for heavy ion collisions, with an increase in $\sqrt{s}$ of about one order of magnitude (from 17 to 200 GeV per nucleon pair). The J/ψ suppression pattern at RHIC has been mainly investigated by the PHENIX experiment (Fig. 1.23). J/ψ is detected in both the dimuon (at forward rapidity) and dielectron (at mid-rapidity) channel. The choice of normalising the J/ψ yield to another reference process (such as Drell-Yan) is useful, but not mandatory: in fact, the PHENIX collaboration chose to compare the A-A data directly to p-p ones, by studying the nuclear modification factor:

$$R^{AA}_{J/\psi}(c) = \frac{\sigma^{pp}_{inel} N^{AA}_{J/\psi}(c)}{\sigma^{pp}_{J/\psi} N_{binary}(c)} \tag{1.10}$$

where σ^{pp}_{inel} and $\sigma^{pp}_{J/\psi}$ are the inelastic cross section and the measured cross section for J/ψ production in p-p collisions, respectively, $N^{AA}_{J/\psi}$(c) is the measured number of J/ψ per A-A collision at centrality c and $N_{binary}(c)$ is the number of binary collisions for the same centrality. $R^{AA}_{J/\psi}$ is basically the ra-

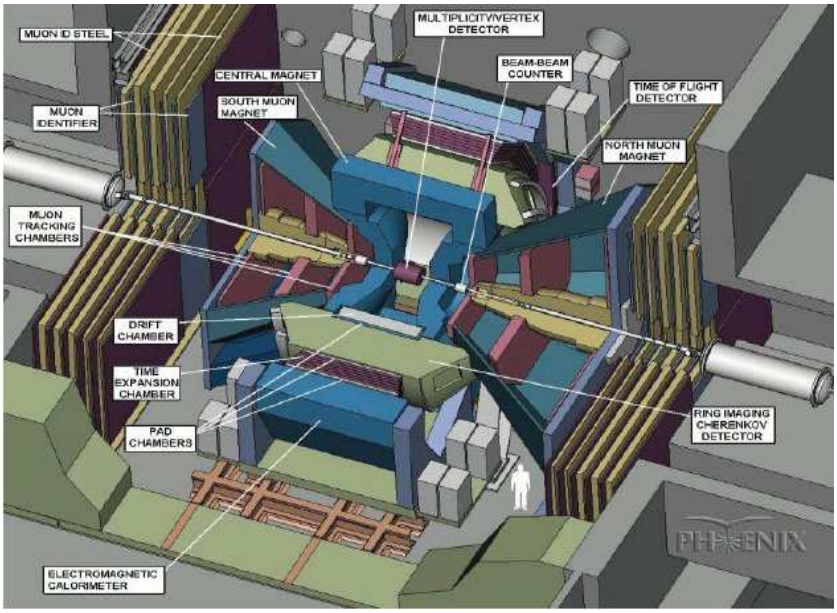

Figure 1.23: The PHENIX experiment at RHIC.

tio between the J/ψ yield per nucleon collision in AA collision and the same quantity in p-p collisions.

The results[25] obtained by PHENIX on J/ψ suppression in Au-Au and Cu-Cu collisions have been puzzling the heavy ion community, since it looks like the amount of suppression observed at RHIC is pretty much the same as the one observed at SPS. The behaviour of $R^{AA}_{J/\psi}$ at SPS and RHIC is compared in Fig. 1.24.

Two different hypotheses have been made to explain this phenomenon.

Sequential suppression - The measured prompt J/ψ yield is composed for 60% of directly produced J/ψ(1S), and for 40% of J/ψ produced in the decays of higher resonances such as ψ'(2S, 10%) and χ_c (1P, 30%). As it was pointed out in Sec. 1.2.2, the dissociation temperature for J/ψ(1S) is expected to be higher than the one for ψ'(2S) and χ_c (1P): if the temperatures reached at SPS and RHIC, though different, are both in the region between the χ_c dissociation temperature and the J/ψ dissociation temperature, then one can expect the observed suppression to be the same, since in both cases the suppression only affects the feed down and not the direct J/ψ.

Regeneration - The production of charm in the thermalised medium is expected to be suppressed by the high mass of the c quark. If, anyway, an excess of charm is produced during the primary collision, it can survive until

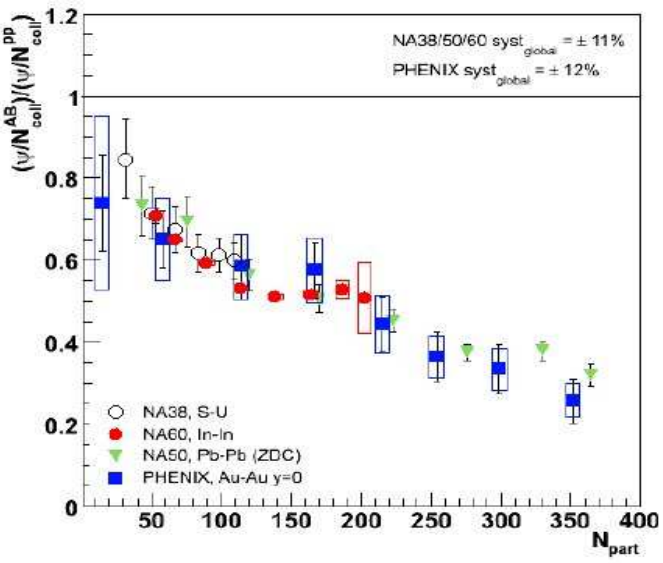

Figure 1.24: J/ψ nuclear modification factor as a function of the number of participant nucleons at RHIC and SPS. The curves are not corrected for nuclear absorption.

the hadronisation stage, where uncorrelated $c\bar{c}$ pairs can recombine to form a J/ψ. The extra J/ψ yield thus created is expected to increase with the energy of the collision (because so does the charm cross section): the suppression at RHIC may thus be partially compensated by the enhancement due to regeneration.

The two scenarios presented above lead to very different predictions for experiments at higher energies (Fig. 1.25):

- if sequential suppression is the correct explanation, then the J/ψ should eventually melt, leading to an increased suppression;
- if regeneration is the correct explanation, then the J/ψ yield is expected to grow as more charm is produced.

The puzzle is thus expected to be solved at the Large Hadron Collider (LHC) at CERN, where Pb-Pb ions will collide at $\sqrt{s}$=5.5 TeV per nucleon pair.

Finally, there exist other experimental topics regarding J/ψ suppression, whose discussion goes beyond the scope of this work, but which are complementary to the topics discussed here: these include the differences between J/ψ suppression at forward and mid-rapidity and the centrality-dependence of $< p_T^2 >$. The study of these and other items at the LHC is expected to shed

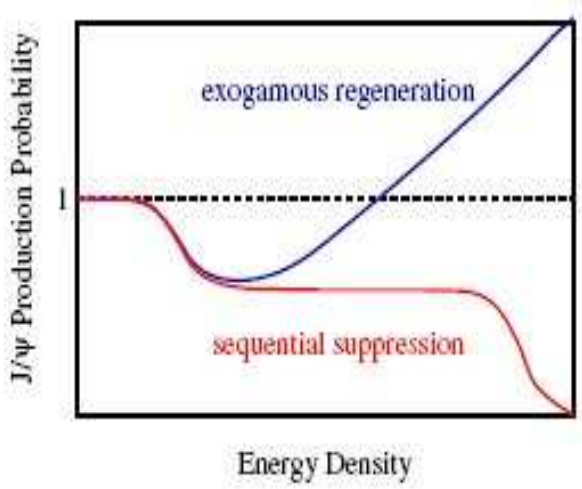

Figure 1.25: J/ψ yield as a function of the energy density according to the regeneration and sequential melting scenarios.

new light on the behaviour of J/ψ and other quarkonia in a Quark-Gluon Plasma.

Chapter 2

ALICE and the muon spectrometer

2.1 A Large Ion Collider Experiment

2.1.1 The Large Hadron Collider

With a radius of 27 km, the Large Hadron Collider[26, 27] at CERN is the largest collider in the world. It is housed in the tunnel of the previous Large Electron Positron collider, at a depth between 50 and 175 m underground. It will serve as both a proton and ion collider.

The nominal luminosity for p-p collisions is of 10^{34} $s^{-1}cm^{-2}$, while for Pb-Pb collisions it is about 10^{27} $s^{-1}cm^{-2}$. The PS and SPS rings will be used as injectors for the machine (fig. 2.1); in particular, the SPS will inject protons in the LHC ring with an energy of 450 GeV. The beams will be accelerated in two separate rings, with intersections corresponding to the experiments.

The LHC present schedule includes:

- regular p-p runs at $\sqrt{s}$=14 TeV (9 months/year$\simeq 10^7$ s/year);
- 1$\div$2 years Pb-Pb runs at $\sqrt{s}$=5.5 TeV per nucleon pair at nominal luminosity (1 month/year$\simeq$ 10^6 s/year);
- 1 year hybrid collisions (p-Pb at $\sqrt{s}$=8.8 TeV p. n. p., d-Pb or α-Pb);
- 1 year Ar-Ar.

The schedule for the second phase of operation has not been fixed yet, since it will depend on the outcome of the above program. The colliding systems that may be added to the regular p-p runs are:

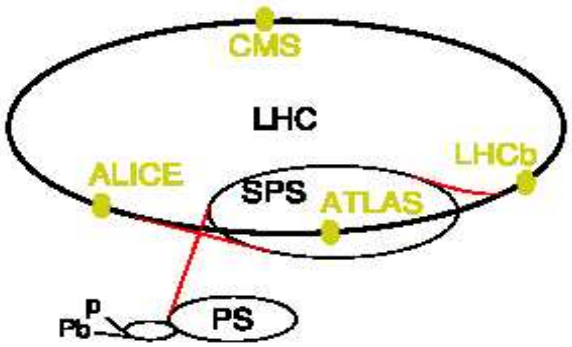

Figure 2.1: The Large Hadron Collider at CERN. The four main LHC experiments and the PS and SPS injector rings are also shown.

- lighter ion collisions such as O-O, N-N, Kr-Kr;
- a dedicated p-p run at $\sqrt{s}$=5.5 TeV;
- d-d and α-α runs;
- hybrid collisions with lighter ions;
- Pb-Pb runs at lower energies.

The main experiments running at the LHC will be:

- A Toroidal LArge Solenoid (ATLAS): a large general purpose experiment whose main goal is the search for the Higgs boson;
- Compact Muon Solenoid (CMS): same as ATLAS;
- LHC-beauty (LHCb): an experiment designed to study CP violation in the sector of b-hadrons;
- A Large Ion Collider Experiment (ALICE): the only LHC experiment dedicated to heavy ion physics;
- Total Cross Section, Elastic Scattering and Diffraction Dissociation (TOTEM): a detector which will measure total and elastic cross sections and diffractive processes; shares the interaction point with CMS;
- LHC-forward (LHCf): an experiment designed to measure the energy and number of forward neutral pions produced in the collisions; shares the interaction point with ATLAS.

While both ATLAS and CMS foresee a heavy ion physics program, secondary to the p-p one, ALICE is the only LHC experiment that was primarily designed to study heavy ion collisions at the LHC.

2.1.2 The ALICE experiment

The ALICE experiment[28] is housed at Interaction Point 2. It currently employs about 1000 physicists from about 30 nations.

Physics program

ALICE is designed to study the physics of strongly interacting matter and the quark-gluon plasma at energy densities never accessed before, in heavy ion collisions, through a set of experimental probes (the most important of which were discussed in Sec. 1.1.3). The ALICE physics program includes data-taking with many different colliding systems: though the focus is undoubtedly on Pb-Pb collisions, nevertheless measurements with each colliding system are of crucial importance, for different reasons:

- data-taking in Pb-Pb collisions will provide access to the higher energy density regime ever studied in a laboratory;
- data-taking in collisions with ions lighter than Pb will allow to span a wide range of energy densities;
- data-taking in p-p collisions will provide a baseline to be compared with A-A data;
- data-taking in p-A collisions will allow to disentangle cold nuclear matter effects from genuine medium effects.

The study of p-A and p-p collisions in ALICE is also interesting as a stand-alone task: given its design, tracking and PID capabilities, ALICE provides access to the study of a few phyisics topics in kinematical regions that are complementary to those explored by the other experiments at the LHC. A discussion of such topics is way beyond the scope of this section, but it is worth mentioning the contribution that ALICE is expected to give to the study of small-x physics and of particle production down to very low p_T.

Experimental apparatus

The main technological challenge for a heavy ion experiment at such high energies is the huge multiplicity of charged particles expected to be produced

in each collision. The design and segmentation of all detectors have been optimised to cope with multiplicities as high as 8000 per unit of pseudorapidity (η in the following).

The ALICE experimental apparatus (Fig. 2.2) consists of:

- a central barrel where hadron, electron and photon tracks will be reconstructed;
- a set of forward detectors whose main task is the determination of centrality and multiplicity;
- the muon spectrometer.

The central and forward detectors[29] will be briefly described in the following paragraphs, while the muon spectrometer will be described more in detail in Sec. 2.2.

Central barrel

Unless otherwise specified, the pseudorapidity coverage of the detectors in the central barrel is $|\eta| < 0.9$.

Inner Tracking System (ITS). It will perform primary and secondary vertex reconstruction, multiplicity measurements, tracking and identification of low momentum particles (p_T down to 20 MeV/c for electrons). It is composed of six cylindrical layers of silicon micro-pattern detectors with two-dimensional read-out (Fig. 2.3), covering the pseudorapidity range $|\eta| <1.7$. The two innermost layers, for which a higher granularity is required, will be made of Silicon Pixel Detectors. Layers 3 and 4 consist of Silicon Drift Detectors, while the outer layers (5 and 6) will be made of Silicon Strip Detectors. Some of the channels will have analog read-out, for the identification of low energy particles via energy loss.

Time Projection Chamber (TPC). The TPC is the main tracking detector in ALICE. Its inner radius (about 90 cm) is defined by the maximum particle density that can be tolerated, its outer radius (about 250 cm) by the path length needed to achieve the desired resolution (7%) on dE/dx for particle identification. The mean momentum of tracked particles is about 500 MeV/c. The electrons drift time over the whole path is about 95 μs: the TPC is a slow detector, but still it can cope with the expected minimum bias collision rate in Pb-Pb (about 8 kHz at nominal luminosity). To prevent pile-up, the luminosity in p-p collisions will be reduced from the nominal value of 10^{34} cm^{-2}s^{-1} to a few 10^{30} cm^{-2}s^{-1} by defocusing the beams at the interaction point (IP).

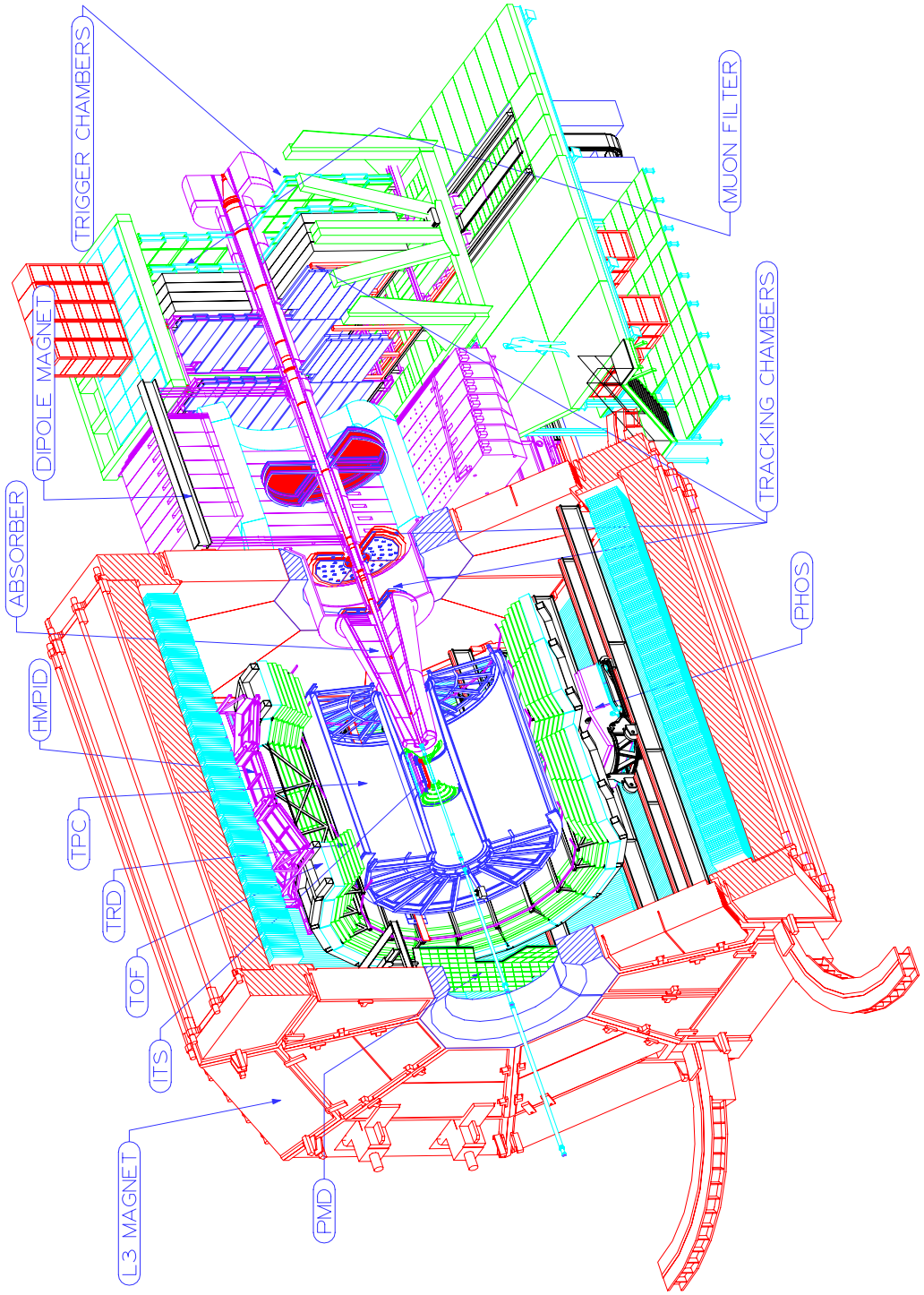

Figure 2.2: The ALICE experiment at the LHC. Not shown: EMCAL, ZDC, FMD, T0, V0.

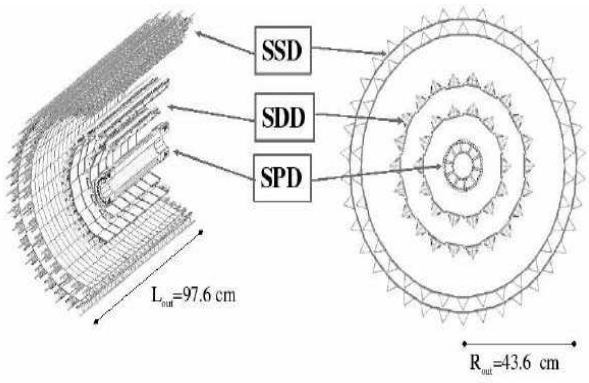

Figure 2.3: The Inner Tracking System of ALICE.

Transition Radiation Detector (TRD). The TRD is composed of 540 detector modules, each consisting of a radiator and a multiwire proportional chamber. It will provide electron identification for p_T >1 GeV/c, and pion-electron separation better than 1% for p_T >3 GeV/c. Given its 600 μm position resolution in the bending plane, it can be coupled to the ITS and TPC to improve the momentum resolution. It is complementary to the muon spectrometer, since it provides access to the study of quarkonia and open heavy flavoured mesons in the electronic channel. It can exploit the vertex information provided by the ITS (which has the same angular acceptance) to separate primary J/ψs from those originating from B-mesons decays, but the high p_T trigger cut on electrons prevents triggering on charmonium with p_T <5 GeV/c.

Time of Flight (TOF). It will perform π/K (π/p) separation for momenta above 0.5 GeV/c and up to 2 (2.5) GeV/c, and e/π separation in the momentum range between 140 and 200 MeV. The time of flight is measured by means of Multigap Resistive Plate Chambers with an intrinsical time resolution of about 50 ps.

High Momentum Particle Identification (HMPID). Identification of particles with momenta above 1.5$\div$2 GeV/c is performed by a Ring Imaging Čerenkov detector, providing π/K (π/p) identification up to 3.4 (5) GeV/c.

Photon Spectrometer It is a high resolution photon calorimeter, made out of $PbWO_4$ crystals. The PHOS covers a pseudorapidity interval $|\eta|$ <0.12 and a 100° azimuthal interval. It will measure both direct photons and decay photons (high p_T π_0 and η). Its position resolution is good enough to distinguish between the two. Since the PHOS is sensitive to charged particles, it is coupled to a Charged Particle Veto device based on the signal from a multiwire proportional chamber. To reject background from neutrons and

other neutral hadrons, a cut on the shower width is applied.
Electromagnetic Calorimeter (EMCAL). The last detector to be added to the ALICE design is a lead-scintillator sampling calorimeter. It will cover the pseudorapidity range $|\eta|$ <0.7, and a 100° interval in azimuthal angle. It will provide good γ/π_0 and electron/hadron discrimination. It will add to the ALICE capabilities in reconstructing the neutral component of jets.
Solenoidal magnet. It is a large solenoidal magnet, the same used for the L3 experiment at LEP; it provides a uniform and relatively weak field ($\simeq$ 0.5 T), so that particles down to p_T $\simeq$100 MeV/c can be tracked in the TPC.

Forward detectors

The location of the ALICE forward detectors is shown in Figs. 2.4 and 2.5.
Zero Degree Calorimeters (ZDC). The main task performed by these calorimeters is the estimation of the collision centrality via the energy deposited by the spectator nucleons. There are four ZDCs, two for neutrons (ZN) and two for protons (ZP). They are located 116 m away from the IP; at such distance, protons and neutrons are spatially separated by the LHC magnetic elements: for this reason, while the neutron calorimeter is placed at zero degrees with respect to the LHC beam axis, the proton calorimeter is displaced (Fig. 2.4). The ZDCs are "spaghetti" calorimeters, composed of a dense absorber (brass for ZP, a tungsten alloy for ZN) in which quartz fibers are interspersed. The choice of quartz fibers instead of the conventional scintillating ones is due to the requirements in terms of radiation-hardness (the estimated daily dose for ZN during Pb-Pb operation is of about 10^4 Gy), while the choice of a dense material was driven by the small space available for the detectors (in particular, ZN must fit in a 8 cm wide space between the two beam pipes).
Forward Multiplicity Detector (FMD). The FMD is a silicon detector segmented into seven modules surrounding the beam pipe, at distances between 42 and 225 cm from the IP. The FMD pseudorapidity[1] windows are 1.7< η <3.4 and -5.1< η <-1.7, complementary to the ITS coverage. The main goal of the FMD is the measurement of charged particle multiplicities ranging fron tens (in p-p) to thousands (in Pb-Pb); the FMD will also provide a multiplicity trigger signal.
Photon Multiplicity Detector (PMD). The PMD is a pre-shower detector measuring the photon multiplicity and angular (η and φ) distributions in the pseudorapidity window -3.5< η <-2.3, providing estimates for the

[1]The convention adopted in this work assigns positive (pseudo) rapidities to the muon arm side.

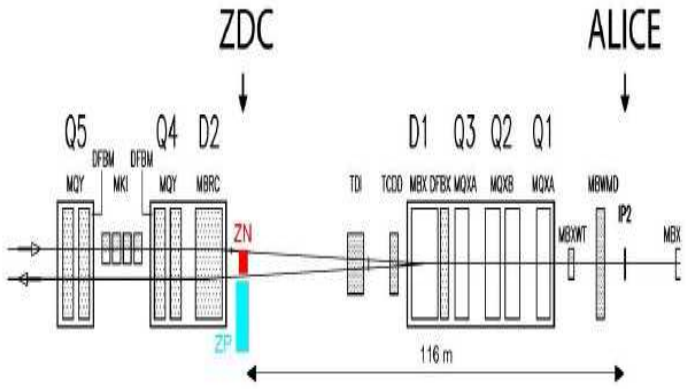

Figure 2.4: Location of the ALICE Zero Degrees Calorimeters ZN and ZP along the LHC beam line.

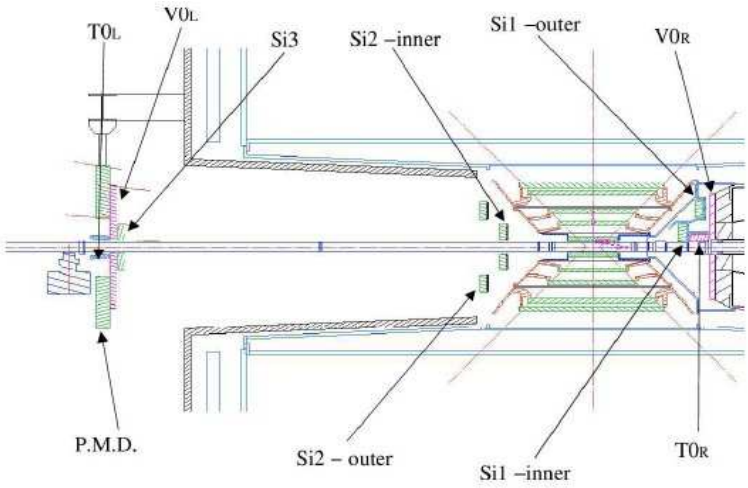

Figure 2.5: Location of the ALICE forward detectors V0, T0, PMD and of the FMD modules Si1, Si2 and Si3 along the LHC beam line. The location of the PMD corresponds to the L3 magnet door.

reaction plane and for the transverse electromagnetic energy. The PMD is composed of two planes of proportional chambers with a lead converter (3 radiation lengths thick) in between. The front plane acts as a vetoing detector for charged particles.

TO. The T0 detector is composed of two arrays of Čerenkov counters: TO_L (-5< η <-4.5, 350 cm from the IP) and $T0_R$ (2.9< η <3.3, 70 cm from the IP). Its main aim is to generate a start signal for the TOF with a 50 ps precision. Moreover, it can measure the vertex position with a resolution of the order of the centimeter, enough to discriminate against beam-gas interactions: this is needed for triggering purposes.

V0. The V0 detector is composed of two scintillator hodoscopes located at 90 cm ($V0_R$, muon spectrometer side) and 340 cm ($V0_L$, PMD side) from the IP. Its main tasks are the measurement of the vertex position, the estimation of centrality, the rejection of beam-gas interactions and the delivery of minimum bias and centrality triggers.

2.2 The ALICE muon spectrometer

2.2.1 Design

The design of the muon spectrometer was driven by the requirement of a mass resolution as good as 100 MeV/c^2 at 10 GeV/c^2, which is needed to separate the Υ, Υ' and Υ" resonances in the high background environment of central Pb-Pb collisions.

The muon spectrometer (Figs. 2.6 and 2.7) covers the θ range between 2° and 9°, corresponding to the pseudorapidity interval 2.5< η <4. It is composed of three absorbers, a dipole magnet, five stations of tracking chambers and two stations of trigger chambers.

The absorbers, magnet and tracking system are briefly described in the following paragraphs; more emphasis will be put on the trigger system, to which Sec. 2.2.2 is devoted, since the trigger detectors are a subject of this thesis.

Front absorber

The front absorber is located inside the L3 magnet, 90 cm away from the IP. It is made predominantly of carbon and concrete, alternated in both the radial and longitudinal direction. It is 4 m long ($10X_0$): its composition was optimised in order to limit multiple-scattering and energy loss of the muons and backscattering in the TPC. In particular, lower Z materials such as carbon are located nearer to the vertex in order not to deteriorate the

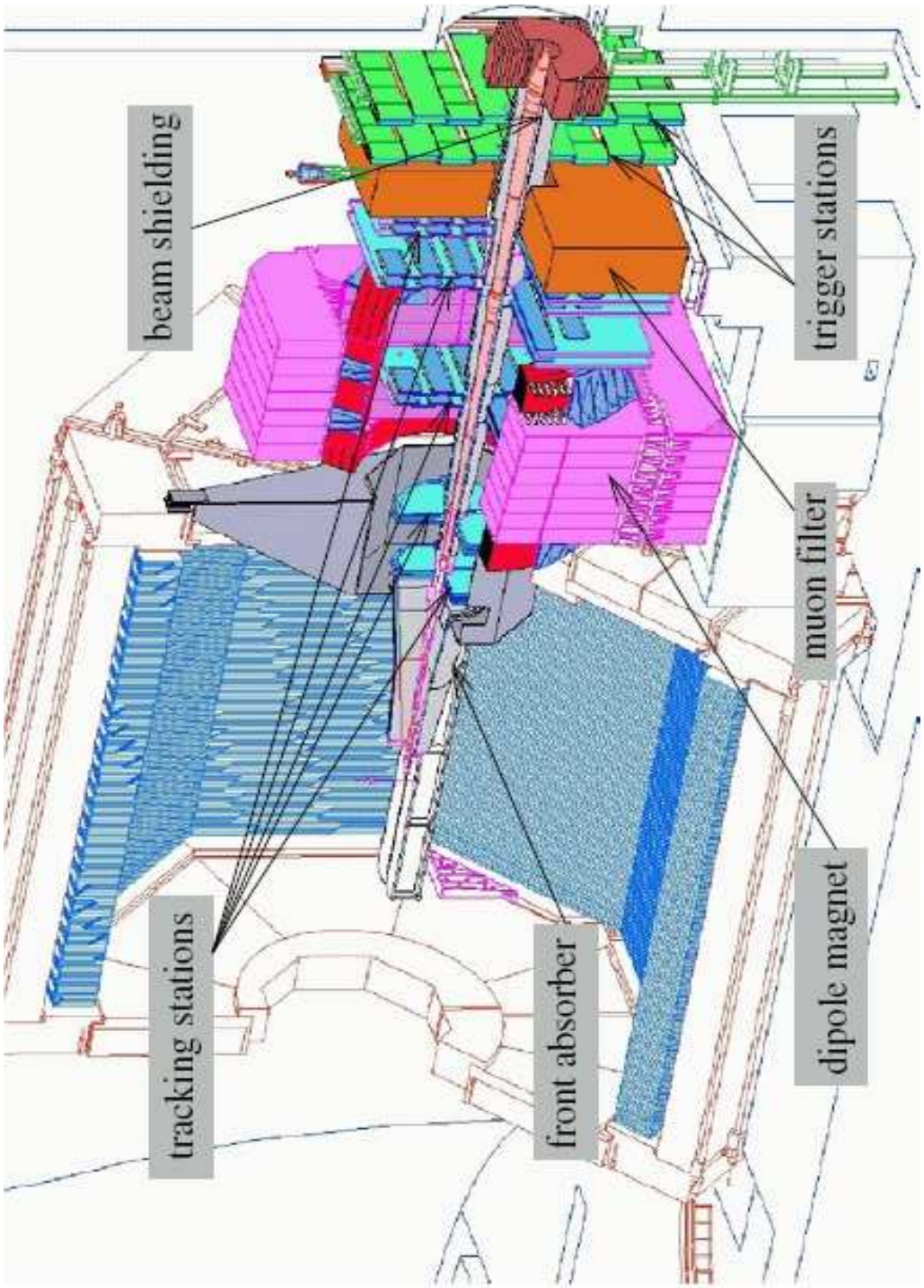

Figure 2.6: Schematic 3D view of the ALICE muon spectrometer.

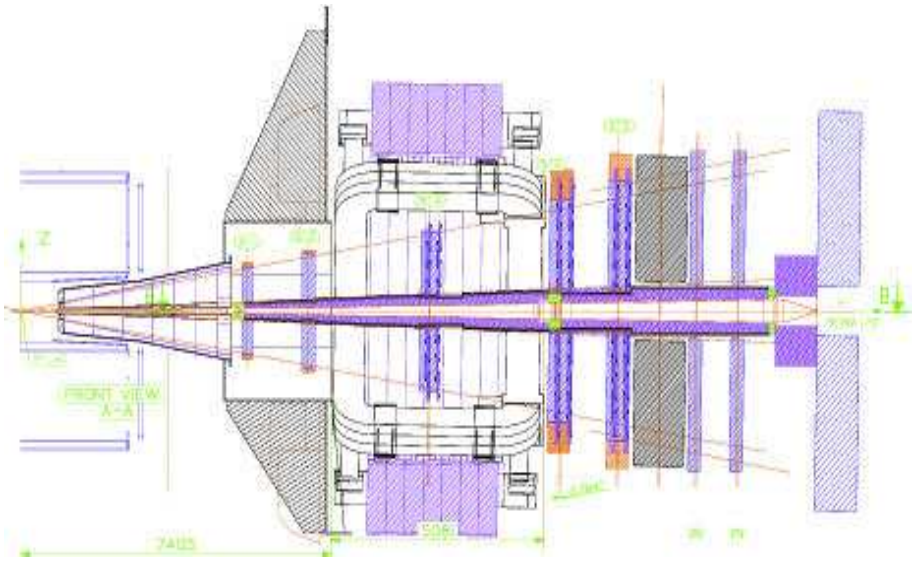

Figure 2.7: Schematic side view of the ALICE muon spectrometer.

mass resolution. The front absorber stops most of the hadrons emitted in the muon spectrometer acceptance, thus reducing the particle flux on the detectors by two orders of magnitude.

Beam shield

The beam pipe is shielded by an assembly of tungsten, lead and stainless steel, which surrounds it. The beam shield prevents particles produced at very small angles and secondaries generated in the beam pipe from reaching the detectors.

Dipole magnet

A dipole magnet with resistive coils is placed about 7 m away from the IP, outside the L3 magnet. It is 5 m long and weighs about 850 tons. The nominal field is 0.7 T, in the x direction (i.e. perpendicular to the beam and parallel to the LHC radius), so that the bending plane is the yz plane and the non-bending plane is the xz plane (z denotes the coordinate along the beam line).

Tracking system

The tracking system covers an area of about 100 m^2. It is composed of five stations of two detection planes each, located (distances are given from the IP) before (5.4 and 6.4 m), inside (9.8 m) and after (12.9 and 14 m) the dipole magnet. To achieve the desired Υ mass resolution, a momentum resolution $\Delta p/p<1\%$ is needed, i.e. a spatial resolution of 100 μm in the bending plane and 1 mm in the non-bending plane. Moreover, the tracking chambers are required to tolerate a high hit density ($5\times10^{-2}/cm^2$ for the most exposed detectors, located in the first station).

The above requirements are met by multiwire proportional chambers with segmented cathode planes (Cathode Pad Chambers, CPC), filled with an Ar/CO_2 (80/20) gas mixture. Each CPC is read on both cathodes, providing two-dimensional spatial information. To keep the occupancy at a 5% level, a very fine segmentation is needed: pads near the beam pipe in the first station are as small as 4.2×6 mm^2. The total number of read-out channels is about 1 million. The chambers in station 1 and 2 have a quadrant geometry (Fig. 2.8(a)), with read-out electronics on the surface, while those in stations 3 through 5 have a slat geometry (Fig. 2.8(b)) and read-out electronics on the side. In order to minimise multiple scattering of the muons, the materials in

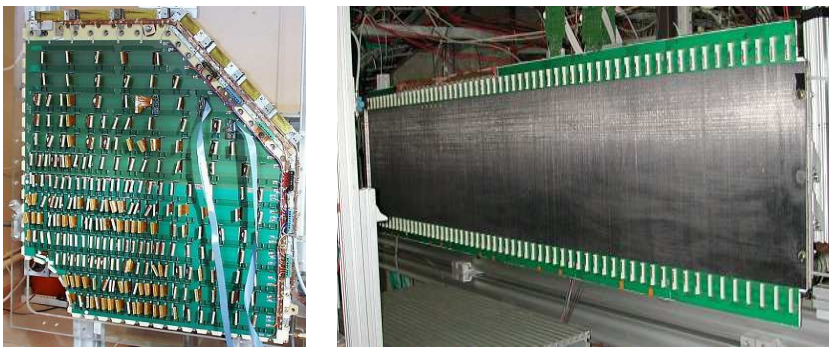

(a) (b)

Figure 2.8: The tracking chambers of the ALICE muon spectrometer: a quadrant (a) and a slat (b).

the tracking system are composite materials such as carbon fibre, so that the total thickness of a chamber is 0.03 X_0. Given the strict spatial resolution requirements, the position of the chambers is monitored optically by a Global Monitoring System within a 20 μm accuracy.

The front-end electronics for all stations is based on a 16 channel chip (Multiplexed Analogic Signal, MANAS). Four of these chips are mounted on a front end MANAS Numerical card (MANU), equipped with a 12-bit ADC, read by the Muon Arm Read-out Chip (MARC) with zero suppression. Data from the MANU are collected and transferred to the DAQ within 240 μs after the trigger signal.

The tracking chambers, with their final front-end electronics, have been tested at CERN, with muons from the SPS and pions from the PS. Both slats[31] and quadrants[32] have been shown to meet the above mentioned spatial resolution requirements.

Muon filter

One more absorber is located in between the tracking and the trigger system, 14.5 m away from the IP: it consists of an iron wall 120 cm (1.2 X_0) thick, whose aim is to reduce the background on the trigger chambers (which are less constrained by multiple scattering) by absorbing pions and low-momentum muons: the combined effect of the front absorber and the muon filter prevents muons with p<4 GeV/c from reaching the trigger chambers.

2.2.2 The ALICE muon trigger system

The goal of the muon trigger is to select unlike-sign muon pairs from the decay of resonances, like sign muon pairs for combinatorial background studies and single muons from open heavy flavours.

The expected collision rate in Pb-Pb at nominal luminosity is about 8 kHz. The trigger rate that can be tolerated by the DAQ system is of the order of 1 kHz. In central Pb-Pb collisions, about eight muons from π and K decays are emitted per event in the muon spectrometer acceptance. As shown in Fig. 2.9, these background muons have a predominantly low-momentum p_T distribution. To minimise the probability of triggering on background muons, a p_T cut must be applied. For this purpose, a large-area trigger system based on position sensitive detectors with a resolution of the order of the cm is needed: this is realised by means of Resistive Plate Chambers (RPC).

Design

The trigger system is based on two trigger stations (Fig. 2.10(a)), located 16.1 m (MT1) and 17.1 m (MT2) away from the IP. Each station is composed of two detection planes of 18 single-gap RPCs each, so that the total number

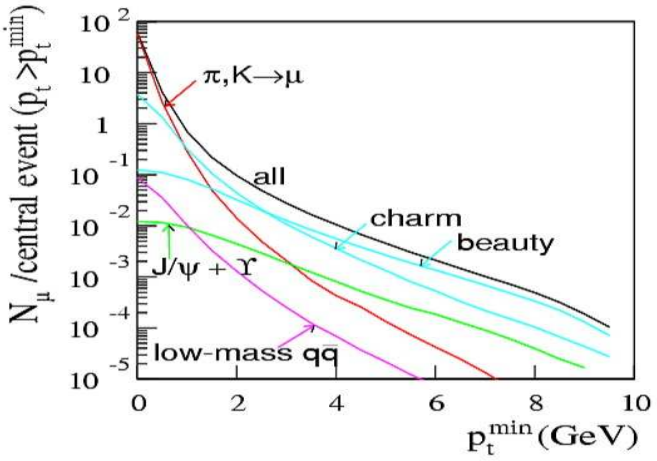

Figure 2.9: Average number of muons with $p_T > p_T^{min}$ emitted in $2.5 < \eta < 4$ in a central Pb-Pb collision at the LHC, as a function of p_T^{min}.

of RPCs is 72. More details about the detectors will be given in Chap. 3. RPCs are read on both sides with copper strips: the horizontal strips (X) measure the coordinate along the y direction (bending plane), while the vertical strips (Y) measure the coordinate along the x direction (non-bending plane). The total number of channels is about 21000. Each half plane is composed of detectors of three kinds: Long, Cut and Short (L,C,S), as shown in Fig. 2.10(b), with different shape and segmentation; L-type detectors come in three different segmentations. The shape of the detectors is driven by the need to allow a central hole for the beam pipe.

In order to ensure a flat occupancy throughout the plane surface, the pitch and length of the strips increase with the distance from the beam pipe, approximately in the same proportion as the hit-rate per surface unit decreases. The pitch of the strips is also conditioned by the momentum resolution required for the p_T cut: X strips have widths ranging from about 1 cm (near to the beam pipe) to about 4 cm (in the most peripheral regions), while Y strips only have widths of 2 and 4 cm, since the resolution requirements in the non-bending plane are less stringent. The strip segmentation of all types of detectors is shown in Fig. 2.11. The strips are arranged in projective geometry, i.e. the strip pitches in the four detection planes scale with the distance of the plane from the IP (Tab. 2.1). Similarly, the area of the detectors is larger in MT2 than in MT1 (Tab. 2.2).

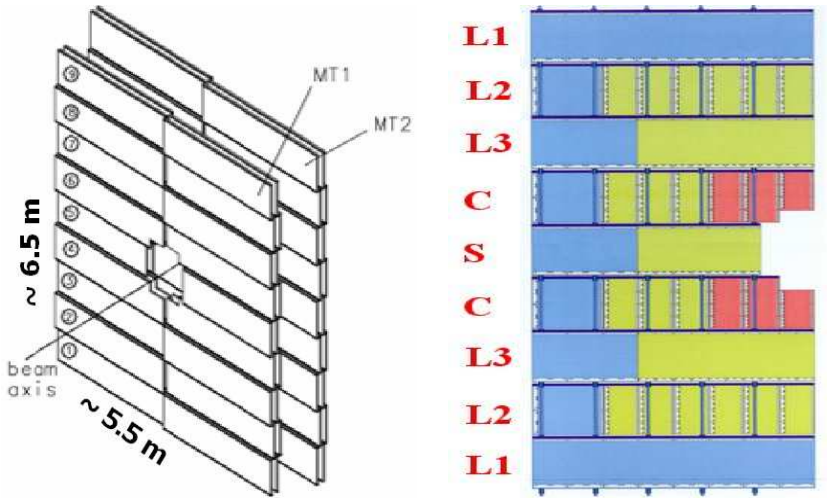

(a) (b)

Figure 2.10: Schematic 3D view of the ALICE muon trigger system (a); detector composition of a half plane of the ALICE muon trigger system (b).

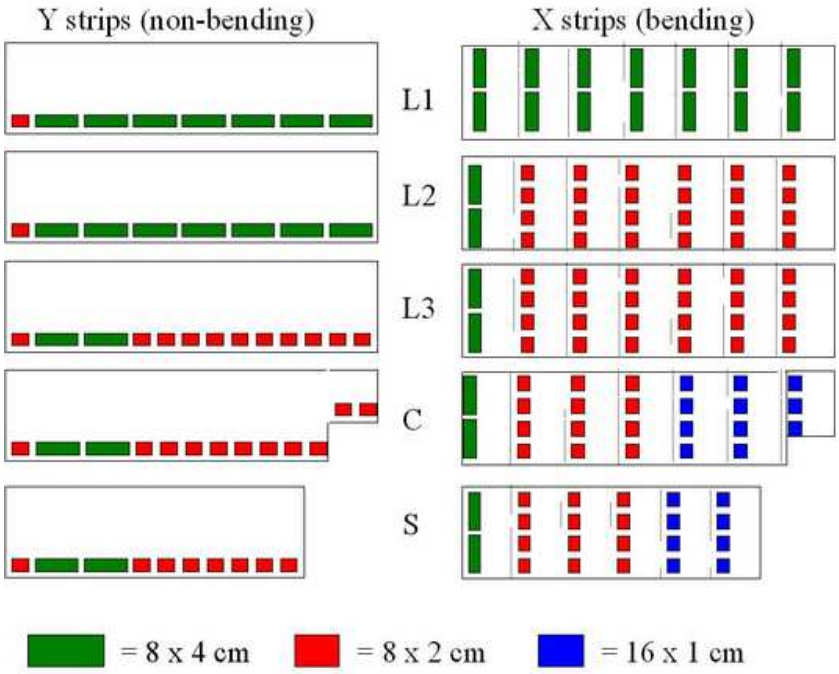

Figure 2.11: Strip segmentation of the detectors in the ALICE muon trigger.

Station	Plane	Strip pitches (mm)		
MT1	1	10.63	21.25	42.50
MT1	2	10.74	21.48	42.95
MT2	1	11.29	22.58	45.15
MT2	2	11.40	22.80	45.60

Table 2.1: Strip pitches for the four detection planes of the ALICE muon spectrometer.

Station	Detector type	Area (mm^2)
MT1	L,C	2740×720
MT1	S	2230×720
MT2	L,C	2920×765
MT2	S	2376×765

Table 2.2: Dimensions of the detectors in the ALICE muon trigger. The reported dimensions do not take into account the corner cut of C-type detectors.

Trigger principle

Two different p_T cuts have been defined[33], which represent a compromise between efficiency and background rejection: a low p_T cut (1 GeV/c) optimised for J/ψ detection and a high p_T cut (2 GeV/c) optimised for Υ detection. The p_T cut is implemented according to the following method[34], illustrated in Fig. 2.12: a muon created at the IP is bent by the dipole field and fires the trigger stations MT1 and MT2 in the positions (x_1, y_1, z_1) and (x_2, y_2, z_2). The deviation induced along the y direction by the dipole magnet is defined as:

$$\delta y_2 = y_2 - y_{2,\infty} \tag{2.1}$$

where $y_{2,\infty}$ is the position in which a muon with infinite momentum crossing MT1 in y_1 would fire MT2. If the deviation due to the magnetic field is less than 10°, δy_2 can be written in terms of the particle p_T with reasonable approximation:

$$\delta y_2 = (z_2 - z_1)\frac{eBL}{z_1}\frac{R_F}{p_T} \tag{2.2}$$

where B is the magnetic field, L is the dipole length and R_F is the radial position in the dipole mid-plane. It is thus clear how, at least at first order, a cut on δy_2 corresponds to a cut on p_T. Moreover, positive and negative muons can be distinguished according to the sign of the deviation. The calculated

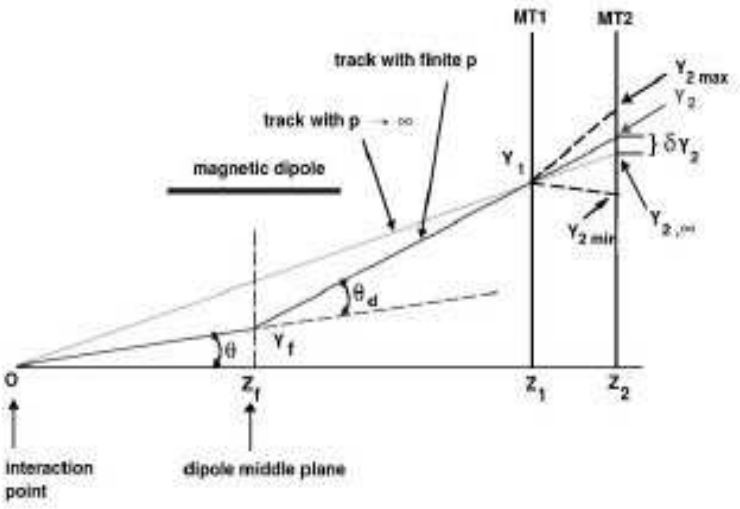

Figure 2.12: The ALICE muon trigger principle: projection in the bending (yz) plane.

values of δy_2 as a function of p_T are stored in look-up tables, to be compared with the measured deviation in strips. The x coordinate information is used to check that the tracks point back to the IP, providing an effective tool for background rejection.

When one of the two planes in MT1 is fired, a road[35] is opened, i.e. a set of strips that should be fired in the other three planes if the track is coming from the IP. If three out of the four planes have counted a hit belonging to that road, the track is processed and the p_T estimated. Depending on the preset trigger mode, the trigger signal is issued if there are two unlike sign tracks, or two like sign tracks, or a single track, with momentum above the p_T cut. The choice of a 3/4 condition accounts for possible detector inefficiencies or dead channels.

Electronics

The RPCs are equipped with the ADULT[36] front-end electronics, which employs a dual threshold technique[2] to improve the timing performances of the detectors, thus matching the time resolution of $1 \div 2$ ns needed for the identification of the bunch crossing (each 25 ns in p-p).

The local trigger electronics (234 VME boards hosted in 16 crates) receives digital signals, in the form of bit patterns, from the front-end chips

[2]The ADULT technique will be described in Chap. 3.

(about 2000 cards). The local electronics performs two main tasks:

- generates the local level-0 muon trigger, performing the p_T cut on single tracks;
- stores the input bit patterns in a pipelined memory which will be read out at the occurrence of either a muon trigger or a trigger by another ALICE detector.

The response time so far is 250 ns. The local trigger information is then sent to the regional trigger boards (one for each of the above mentioned crates), hence to the global trigger electronics which issues either the single muon or the (un)like-sign muon pair signal. The total latency of the muon trigger is about 700 ns (including cable delays), small enough to enter the general ALICE L0 trigger[37].

Performance

Simulations[38] have been carried out to evaluate the performances of the trigger system, with particular emphasis on the efficiency for heavy quarkonia and on the total expected trigger rates. The trigger efficiency (defined as the ratio of triggered to triggerable particles) is about 70% (90%) for J/ψ (Υ), as obtained with the low (high) p_T cut. It is important to note here that the trigger efficiency (and acceptance) is non-vanishing at zero p_T. The unlike-sign dimuon trigger rates expected in Pb-Pb, Ar-Ar and p-p are reported in Tab. 2.3, for nominal luminosity values[3]: for all colliding systems, the values are safely below 1 kHz.

Colliding system	$\sqrt{s}_{NN}$ (TeV)	$\mathcal{L}$ ($cm^{-2}s^{-1}$)	f_{low}(Hz)	f_{high}(Hz)
Pb-Pb	5.5	5×10^{26}	330	65
Ar-Ar	6.3	5×10^{28}	630	73
p-p	14	3×10^{30}	5÷15	2÷8

Table 2.3: Monte Carlo unlike-sign dimuon trigger rates in the ALICE muon spectrometer, for given luminosity values, for low and high p_T cut.

2.2.3 Physics with the ALICE muon spectrometer

It has already been discussed how heavy quarkonia can be studied via their electronic decays in the ALICE central barrel, with the Transition Radiation

[3]The trigger rates are expected to scale directly with the luminosity.

Detector. Quarkonia measurements in the muon channel will be performed in the forward muon spectrometer[30, 39]. Nevertheless, more physics items will be addressed by the spectrometer, in A-A collisions but also in p-p and hybrid collisions. These items include open beauty and electroweak bosons. The detection of open charm and low mass vector mesons in the ALICE muon spectrometer is not trivial and has only recently begun to be investigated.

The performances described below have been published by the ALICE collaboration in Ref. [39], except where otherwise specified.

Quarkonia

The physics associated with quarkonia in nucleus-nucleus collisions has already been discussed in Sec. 1.2.2. In particular, it has been pointed out how quarkonia measurements at the LHC energies are expected to discriminate between the different scenarios that have been conjectured to explain the SPS and RHIC results on charmonium. Moreover, the much higher energy at the LHC offers the possibility of measuring with significant statistics the bottomonium yields, thus providing an additional probe for QGP studies.

Together with the above mentioned new possibilities, new problems arise in the study of quarkonia production at the LHC. First of all, in the dense medium produced in a heavy ion reaction, energy loss of heavy quarks might modify the particle spectra: this implies that the study of quarkonia production should be carried out in parallel with the study of open heavy flavours. Moreover, the choice of normalisation processes is not straightforward and the combinatorial background will be huge. To get a picture as clear as possible, a very detailed study shall be carried out, including the measurement of quarkonia:

- as a function of centrality, to identify the suppression pattern;
- for different colliding systems (to disentangle normal and anomalous suppression);
- for all quarkonium states (to probe sequential melting);
- as a function of p_T and rapidity (to discriminate between QGP models);
- together with open charm and beauty (see discussion above);
- versus the reaction plane (to test alternative absorption mechanisms);

As it has already been pointed out, the choice of the normalisation of the signals is crucial when studying medium effects. The normalisation with

respect to Drell-Yan processes used by the NA50 and NA60 experiments is not conceivable at LHC energies, since Drell-Yan dimuon production will be overwhelmed by muon decays of open charm and beauty. Alternative strategies, proposed or used by other experiments are:

- the Z boson;
- the open charm (beauty) signal;
- the minimum bias method (i.e. the bare measurement of the quarkonium yield per A-A collision as a function of centrality);
- the p-p cross section, i.e. the measurement of the nuclear modification factor R^{AA} defined in Eq. 1.10;
- the bare quarkonium yield without normalisation.

A detailed review of the advantages and drawbacks of the above methods can be found in Ref. [39]. In Chap. 6 an analysis of the systematics concerning the normalisation to p-p data (R^{AA} method) will be presented.

The performances of the ALICE muon spectrometer in Pb-Pb collisions have been analysed by means of detailed simulations. The Monte Carlo dimuon spectrum in the J/ψ and Υ mass regions as measured by the muon spectrometer is shown in Fig. 2.13. The expected J/ψ yields in one year of heavy ion LHC operation at nominal luminosity range from 130000 in the most central class (impact parameter b<3 fm) to 22000 in the most periperhal class class (b>12 fm). The same quantities for the Υ amount to 1300 and 200, respectively. Since the muon spectrometer is not equipped with a vertex tracker, it can not distinguish between prompt (i.e. produced at IP) and secondary (from B meson decay) J/ψ. The yields reported include both contributions. A reasonable statistics is also achievable for the measurement of Υ' production. With the achieved mass resolution (about $1\div2\%$, see Sec. 2.2.1), the ALICE muon spectrometer should be sensitive enough to discriminate between different suppression scenarios (Fig. 2.14).

Moreover, studies have been carried out to investigate the possibility of measuring the J/ψ azimuthal anisotropy, which will provide additional information on J/ψ suppression mechanisms such as direct absorption on participating nucleons, comover absorption or QGP formation.

The study of quarkonia in p-p collisions has a twofold interest: on one hand, p-p measurements represent a baseline for A-A data; on the other hand, they have an intrinsic interest, since they are expected to shed light on the quarkonia production mechanism through the study of differential cross sections and polarisation. In particular, these measurements provide access

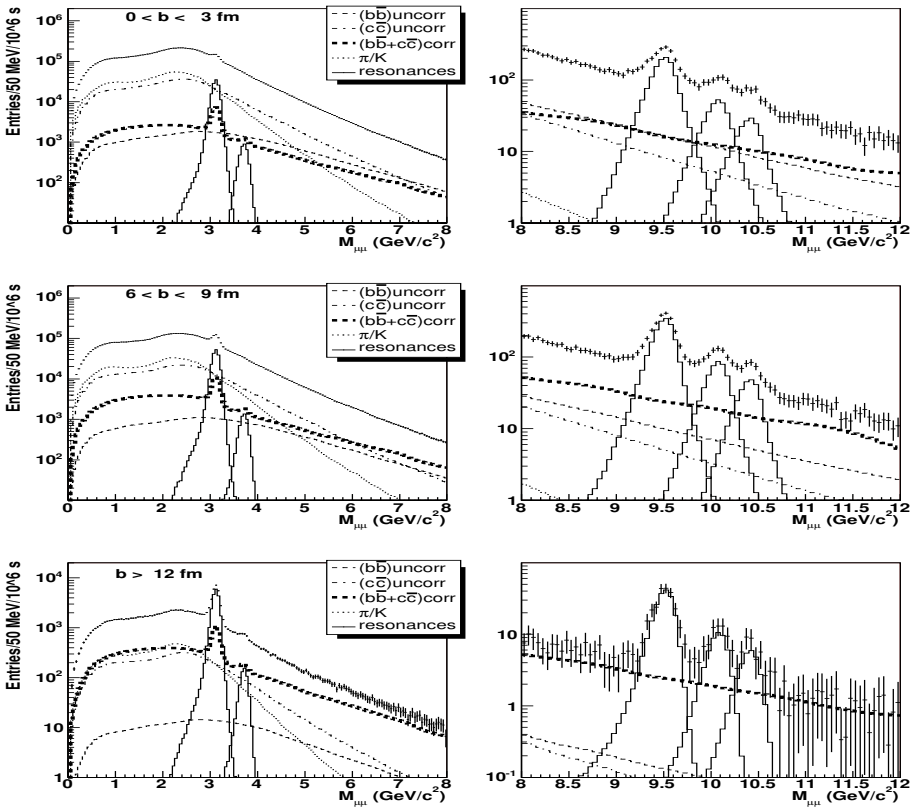

Figure 2.13: Monte Carlo unlike-sign dimuon mass spectra in the J/ψ (left) and Υ (right) region, for three centrality classes, as measured by the ALICE muon spectrometer in a Pb-Pb run of 10^6 s, for a luminosity of 5×10^{26} cm^{-2}s^{-1}.

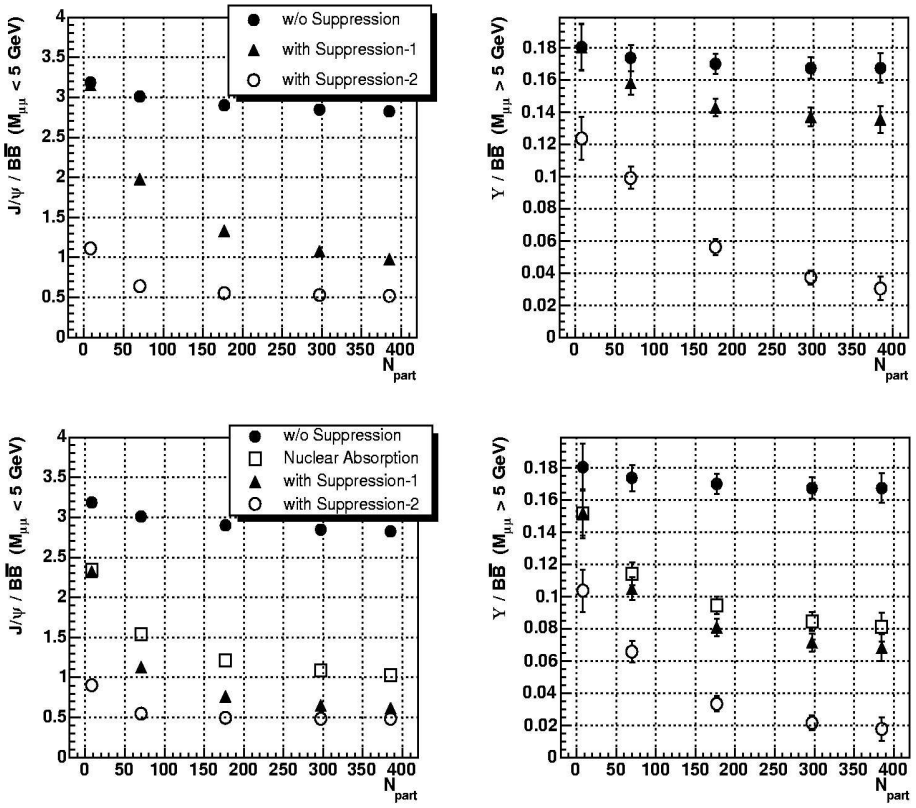

Figure 2.14: Ratio of J/ψ (left) and Υ (right) to open beauty yield as function of the number of participants, as measured by the ALICE muon spectrometer in a Pb-Pb run of 10^6 s, for a luminosity of 5×10^{26} cm^{-2}s^{-1}. The suppression scenario 1 (2) reported in the labels corresponds to a dissociation temperature of 460 (230) MeV for the J/ψ and 1100 (550) MeV for the Υ. In the bottom panels, nuclear absorption is added to the QGP effects.

to the Parton Distribution Functions at very small x[40]. Finally, the study of quarkonia in p-A collisions in the muon spectromer provides a useful tool to disentangle cold nuclear matter effects and the possibility to explore the partonic structure of nucleons and nuclei at small x.

Open heavy flavours

The measurement of open charm and beauty production allows one to investigate the mechanisms of heavy quark production, propagation and, at low momenta, hadronisation in the medium. It has already been mentioned how open charm and beauty may be used as reference processes for quarkonia studies. The intrinsic interest of open heavy flavours lies mainly in the possibility to test both perturbative and non perturbative sectors of QCD. While open beauty muons will dominate the high p_T (and high mass in the case of dimuons from $b\bar{b}$) region, charm muons will lie in the low p_T (mass) region, sitting on top of a huge background from lighter hadron decays (Fig. 2.15). For this reason, the physics performance studies have been concentrated on open beauty detection. Open charm detection is also possible but requires the development of dedicated strategies for background rejection.

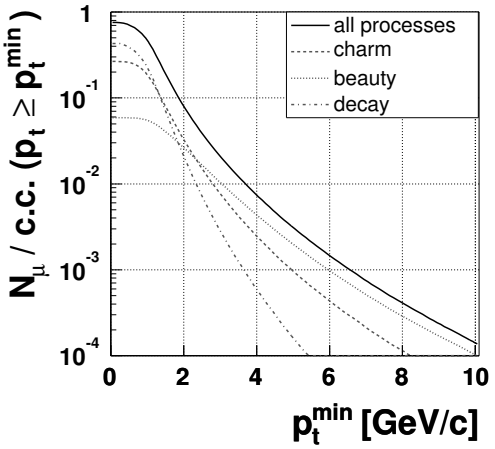

Figure 2.15: Number of muons with $p_T > p_T^{min}$ per central Pb-Pb collision (5% most central) detected in the muon spectrometer, with the low p_T trigger cut (1 GeV/c).

While single muon differential and inclusive measurements will provide large statistics in a wide p_T range, the possibility to detect both muons

from $b\overline{b}$ offers additional information to test QCD predictions, through the dimuon correlations in azimuthal angle, p_T and rapidity, which are sensitive to relevant features of the $b\overline{b}$ production mechanism.

As for the case of quarkonia, measurements in p-p and p-A will be important both as a reference process and *per se*, since they provide access to small Bjorken x regions.

Weak bosons

The high amount of centre-of-mass energy available at the LHC will allow W bosons to be produced with fairly large yields. The branching ratio for the process W$\rightarrow \mu\nu_\mu$ is about 10.6%. In AA collisions, being weakly-interacting probes, W bosons will not interact with the surrounding medium, hence they could provide a reference for observing medium-induced effects on other probes, like energy loss of high p_T b quarks. For the same reason, the combined measurement in A-A, p-A and p-p collisions will allow to test the validity of the Glauber model at LHC energies. Moreover, p-p collisions provide access to the quark distribution functions in the x range from 10^{-4} to 10^{-3}, for large $Q^2 \simeq m_W^2$, while in p-A collisions the production cross section may be sensitive to the nuclear modification of quark distribution functions.

It has been estimated[41] that about 10^5 (10^4) muons from W boson decay will be produced in the muon spectrometer acceptance in one year in p-p (Pb-Pb) collisions.

Chapter 3

Resistive Plate Chambers for the ALICE muon trigger

3.1 Resistive Plate Chambers

A Resistive Plate Chamber (RPC) is a planar geometry gaseous detector, whose structure is shown in Fig. 3.1.

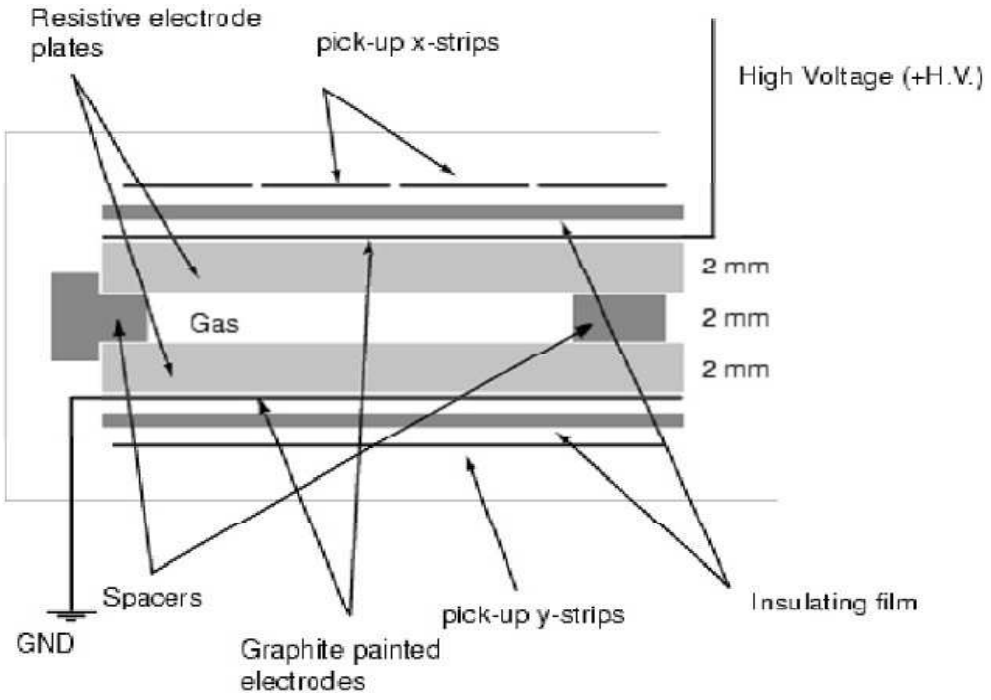

Figure 3.1: Cross section of a Resistive Plate Chamber.

3.1.1 Design and working principle

The main difference between the RPC and a traditional gaseous counter is the resistive material out of which the electrodes are made. These are connected to the High Voltage and to ground by a layer of conductive material applied on their outer surface, and kept at a constant distance between them by plastic spacers inside the gas gap. The detector is filled with gas at room pressure, which flushes through the gap by means of an inlet and an outlet pipe. The voltages required for operation are of the order of $4 \div 5$ kV/mm.

Since the electrode is resistive, the signal can be picked up inductively by means of conductive strips, electrically insulated from the electrodes. The strips have a width of the order of the cm, and, together with their ground plate, behave as transmission lines with a characteristic impedance around 50 Ω. To avoid reflection of the signal, The strip and the ground planes are connected at one end with a 50 Ω resistor.

When they first were conceived[42], RPCs were designed for streamer mode operation: when an ionising particle crosses the gas gap, the liberated electrons eventually give rise to a discharge on the anode. Unlike what happens in an ionisation chamber or in a cylindrical counter, such discharge is a handleable signal, since it is promply quenched by[43]:

- absorption of UV photons by organic gases in the gas mixture, preventing secondary discharges formation via photo-ionisation;
- electron capture by electronegative gases in the mixture, limiting the discharge size;
- an abrupt decrease of the local electric field in the discharge region, due to the resistive electrode: since the discharge duration is of the order of 10 ns and the relaxation time of the electrodes is larger than 10 ms, the electrode behaves as an insulator throughout the whole discharge, preventing the signal from propagating beyond a small region ($\simeq 0.1$ cm^{-2}).

The first two processes are common to many gaseous detector typologies; nevertheless, due to the planar geometry, in a RPC mixtures with strong quenching properties can be employed without loss in efficiency, since the electric field does not decrease with the distance from the anode as in a cylindrical geometry and hence multiplication occurs in the whole gas volume. The third process is instead typical of RPCs. Moreover, the localisation of the discharge provides two dimensional spatial information, provided that the detector is read on both sides with orthogonal strips.

The first prototype of spark counter with a localised discharge was realised in 1971[44]. The electrodes were made of glass ($\rho \simeq 10^{10}$ Ωcm). Due to the small gas volume (gas gap 100 μm), the use of pressurised gas (12 atm) was required. The mixture consisted of argon and a few organic gases. The read out strips (one plane only) were in direct contact with the electrode: the spatial information was obtained from the difference between the arrival times of the signal on the two ends of the strip plane. The detector had very good spatial (200 μm) and time (30 ps) resolution, but it required a great effort in terms of mechanical precision, with consequences in terms of costs and coverable area.

The version of the detector that Santonico and Cardarelli describe in Ref. [42] is extremely simplified: the electrodes are made of bakelite (paper sheets treated with phenol resins) with $\rho \simeq 10^{10} \div 10^{11}$ Ωcm, the gas gap is 2 mm and the gas is at room pressure. The first prototype was 85×13 cm^2 in area and was filled with argon and butane. It had 97% efficiency for cosmic rays. The performances in terms of time and spatial resolution were of course less brilliant than those of the above described spark counter, but the use of robust and relatively cheap materials widens consistently the range of the possible applications of the detector.

While the structure of RPCs has remained essentially unaltered up to nowadays, a lot of effort has been put in the optimisation of the gas mixture. The first RPCs were meant to be operated in streamer mode, i.e. obtaining a signal from the discharge to which the process of multiplication eventually gives rise. Later on, the possibility to operate the detectors with mixtures and voltages such that the multiplication signals does not degenerate in discharge (avalanche mode) began to be investigated. Such developments will be described in Sec. 3.1.3.

In spite of their low cost and robustness, Resistive Plate Chambers provide a time resolution of the order of the ns, a spatial resolution of the order of the cm and a fast response (a few ns). According to experimentals tests[45], they have low sensitivity to neutrons ($\simeq 10^{-3}$ at 1 MeV) and photons ($\simeq 10^{-2}$ at 1 MeV). Also, RPCs are weakly sensitive to magnetic fields. All these reasons make RPCs a suitable detector for use in large area trigger systems, or in cosmic ray physics. Parallel to triggering RPCs, the evolution of the spark counter described at the beginning of this section led to a class of detectors with resistive electrodes which provide excellent time resolution at the cost of a more complex technical design: an example is provided by the Multigap Resistive Plate Chambers employed in the ALICE Time Of Flight and mentioned in Chap. 2. These are commonly referred to as timing RPCs and will not be discussed in this work.

3.1.2 Working parameters

Efficiency

The efficiency of a RPC reaches its maximum value when the applied voltage is high enough for the charge multiplication process to develop and give rise to a signal higher than the preset threshold (in streamer mode the start of a discharge is also required).

The efficiency-HV curve of a properly working RPC should present a steep rise (in a few hundreds of Volts) up to what is called the knee, i.e. a change in the slope, after which the efficiency remains constant. This last part of the curve is commonly referred to as plateau. The efficiency curve moves rigidly towards higher voltage values when increasing the discrimination threshold.

The voltage is not the only parameter affecting the detector efficiency. The effect of temperature and pressure can be understood by recalling that the multiplication process starts when the energy $eE\lambda$ acquired in a mean free path λ by primary electrons accelerated in the electric field E is enough to ionise an atom:

$$eE\lambda = e\frac{V}{d}\lambda > I \tag{3.1}$$

where V is the applied voltage, d is the length of the gas gap and I is the energy required to ionise atoms in the gas. The mean free path λ can be written (with some approximation) as

$$\lambda = \frac{1}{\sigma N} = \frac{k}{\sigma \mathcal{V}}\frac{T}{p} \tag{3.2}$$

where σ is the electron-atom cross section, N is the atom density of the gas, k is the Boltzmann constant and $\mathcal{V}$ is the gas volume. The second equality holds if one uses the equation of state of ideal gases to express the atom density N. The condition in Eq. 3.1 is thus found to depend on the quantity VT/p. To take into account the temperature and pressure dependence of efficiency, an effective voltage can be defined:

$$V_{eff} = V\frac{T}{T_0}\frac{p_0}{p} \tag{3.3}$$

where p_0 and T_0 are reference values at which the applied and effective voltages coincide, and temperatures are expressed in K. At room conditions and voltages around 8 kV, a 5° temperature variation results in an effective voltage variation of about 150 V. The same effect corresponds to a 20 mbar pressure variation. For these reasons, HV power supply systems for RPC are often operated together with a temperature and pressure monitor, so that

the applied voltage can be varied online, in order to keep the effective voltage constant.

The maximum efficiency reached by the detector is usually slightly lower than 100%, due to the spacers, which limit the active volume. The main cause of local inefficiencies in a RPC is the non-perfect parallelism between electrodes, resulting in regions where the gas gap is wider and the electric field is lower.

More case-specific issues concerning the efficiency of Resistive Plate Chambers will be discussed in Chap. 4.

Time resolution

In a conventional cylindrical counter, the electric field scales with the inverse of the distance from the anode wire: only in a limited region near to the anode the electric field is high enough for the multiplication process to start. Consequently, the main source of time uncertainty is represented by the fluctuations in the drift time of electrons to the multiplication region. In a detector with parallel plates the electric field is uniform and critical everywhere: there is no drift region and the spread of the signal arrival time is smaller. The first RPC prototypes[42] had a time resolution slightly worse than 1 ns at voltages around 11 kV. The time resolution of RPCs is better in avalanche mode, for reasons that will be explained in Sec. 3.1.3.

Spatial resolution and cluster size

The spatial resolution of a RPC is of the order of $w/\sqrt{12}$, where w is the strip width. Such value can be modified by cluster size effects, i.e. by the number of adjacent strips on which, in one same event, a signal above the discrimination threshold is induced. The cluster size depends on the size of the avalanche (streamer), which in turn can be affected by the quenching properties of the gas mixture. The typical cluster size of RPCs in streamer mode is about 1.5 with strips 1 cm wide. It has to be pointed out that a properly working RPC will count a physiological number of events with cluster size 2, those when the particle impact coordinate is in between two adjacent strips: in this cases, the spatial resolution is better than $w/\sqrt{12}$ since the particle coordinate is better constrained. An excess of events with cluster size 2, though, usually reflects a large discharge transverse size and is an indicator of poor quenching properties of the gas mixture.

Finally, an important role is played by the surface resistivity of the electrodes and of the conductive layer on them, since this influences the propagation of the electric signal. The conductive layer is usually made out of

graphite, whose surface resistivity is about 100 kΩ/square.

The streamer mode operation is best suited for applications in which an optimal spatial resolution is required. While the pulse amplitude spectrum of the streamer mode presents a narrow peak around a mean value, the pulse amplitude spectrum of the avalanche mode decreases exponentially, so that a relatively low threshold must be adopted in order not to lose the low amplitude signals. For this reason, in case of large avalanches hitting one strip, the signal induced on the neighbouring strips will most probably be above the threshold as well.

Noise rate

The low sensitivity of RPCs to background neutrons and γ has already been mentioned in Sec. 3.1.1. Thus, the main background source of RPCs is the noise due to intrinsic detector effects, such as imperfections in the electrodes surface: if this is not smooth enough, the electric field will be locally higher due to spike effect, leading to extraction of electrons from the cathode, which cross the whole gas gap generating an unwanted discharge. The prevention of such discharges is important not only for the purpose of reducing the background, but also in terms of the rate capability and ageing of the detector, as it will be made clearer further in this section. For this reason, the inner surface of the electrodes is often coated with a linseed oil layer, to ensure a smooth surface.

Other sources of unwanted counts may be the transmission through the conductive strips of external electromagnetic signals (this can be partially avoided by enclosing the RPC in an external metallic structure at ground voltage, which acts as a Faraday cage), or cross-talk phenomena.

The lower amplitude of the avalanche signal and the consequent need to set lower thresholds results in a higher noise rate in avalanche mode with respect to the streamer mode.

Current

The current circulating between the electrodes is an important parameter to be monitored during the detector operation. In case of perfect insulation of the electrodes, there is no ohmic current and the only charge motion is that of the free charges liberated in the gas by ionising particles or electrons extracted from the cathode. In this case, the current is simply an index of the hit rate of the detector. The current drawn by the detector when it is not irradiated is commonly referred to as dark current (but of course most dark current measurements also include the contribution from cosmic ray-induced

signals). An ohmic (leakage) current may however circulate in case of bad insulation of the electrodes from one another or from the external structure. Leakage current can be measured at low voltages, when the contribution from liberated charges in the gas is not important yet.

Rate capability

A streamer signal deposits on the electrodes an average charge of about 500 pC. This causes a diminution of the electric field in the region where the signal was generated, making the detector temporarily inefficient in that region. If the relaxation time of the electrodes is larger than the time interval between two consecutive hits in the same region, this will affect the detector efficiency.

With some approximation, the RPC can be assumed to behave locally like an RC circuit. After the discharge, the capacitor associated with the detector restores the original voltage V_O according to the well known exponential law:

$$V = V_0(1 - e^{-\frac{t}{\tau}}) \tag{3.4}$$

The relaxation time τ=RC can be estimated by considering the circuit in Fig. 3.2(a) or its equivalent in Fig. 3.2(b), whose parameters are:

$$R_p = \frac{\rho d}{S}; \quad C_p = \epsilon_r \epsilon_0 \frac{S}{d}; \quad C_g = \epsilon_0 \frac{S}{g} \tag{3.5}$$

where ρ, S, d and ϵ_r are the electrodes resisitivity, surface, thickness and

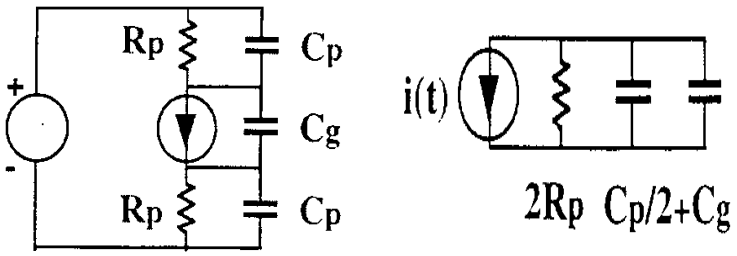

(a) (b)

Figure 3.2: Circuit modeling a RPC during the recharge of the electrodes(a); its equivalent (b).

relative dielectric constant, respectively, g is the gas gap and ϵ_0 is the absolute dielectric constant of vacuum. Putting d=g, the relaxation time is:

$$\tau = RC = 2R_p(\frac{C_p}{2} + C_g) = \epsilon_r \epsilon_0 \rho(1 + \frac{2}{\epsilon_r}) \tag{3.6}$$

With ρ of the order of 10^{11} Ωcm and typical values of ϵ_r ($\simeq$5), one finds a relaxation time of about 10 ms. According to this simple model, the rate capability of RPCs should only depend on the dielectric constant and resistivity of the electrodes.

Tests[46] carried out at the CERN PS with a π beam showed a linear decrease of the efficiency as a function of the incident rate. The efficiency got lower than 90% for hit rates higher than 60 Hz/cm^2. Together with the efficiency loss, a worse time resolution was observed. Subsequent tests[47] carried out with the same detector under γ irradiation from a nuclear reactor showed a degradation of the performance already for hit rates of 15 Hz/cm^2. The explanation[48] that was given to this discrepancy involved the lateral flow of charges, due to the finite surface resistivity of the electrode. This would explain why the performance degradation sets in earlier if the whole surface of the detector is exposed to irradiation (as is the case of exposure to a reactor) than it would if the irradiation were limited to a spot (as is the case of the beam test). An alternative explanation is the alteration of the electrodes resistivity between the two tests (see next paragraph). Within the same context[48], a simple experiment was carried out: the RPC electrodes were connected to a battery, and, once the battery was disconnected, the voltage across the electrodes was measured as a function of time. It was found that the relaxation time τ was not univocal, the curve not following a simple exponential; local fits yielded values of τ at least 10 times larger than the one obtained with Eq. 3.6.

A few authors[48, 49] state that the rate capability of RPCs cannot be increased *ad libitum* by using electrodes with lower and lower resistivity, since for resistivities below $\simeq 10^9$ Ωcm the detectors is likely to become noisy and draw too much current. In Sec. 3.2 it will be shown how the rate capability limits reported above can be strongly ameliorated with a suitable choice of both the gas mixture and the resistivity of the electrodes.

Ageing

The performances of a RPC can suffer from long-term operation. Due to the exposure of the detector at high hit rates, chemical reactions may occur in the gas, leading to the formation of substances not included in the original mixture. These may react with the electrodes, causing alteration of its surface

or resistivity. Such reaction might as well alter the quenching and/or ionising properties of the mixture. Moreover, continuous discharges in the detector as well as chemical reactions may cause the detachment of linseed oil from the electrode.

For example, evidence for the occurrence of chemical reactions was found during the test at the nuclear reactor mentioned above: chromatographic analysis performed on the exhaust gas after a few hours of operation at high detector counting rate (130 kHz) revealed the presence of substances other than the original mixture components.

The chemical reactions in the gas are connected with the presence in the gas of energetic electrons which, on a probabilistic basis, can break the molecular bonds of gases in the mixture, linseed oil and electrode plates. For this reason, the age of a detector is assumed to be proportional to the current per surface unit which was drawn by the detector during its operation period. If the charge deposited on the electrodes at every hit is assumed to be known, ageing can be quantified with the time-integrated rate (hits/cm^2).

Another ageing effect, complementary to those described above, is connected to flushing the detector with a dry (i.e. water-vapour free) mixture: this results in the diffusion of H_2O molecules from the bakelite plate to the mixture. The consequent decrease of the bakelite water content causes an increase of the resistivity and, possibly, mechanical alterations of the electrodes. As it will be shown further in this chapter, such effect can be partially avoided by flushing the detector with a wet mixture containing water vapour.

The most common symptom of ageing in a RPC is the increase of the current and/or hit rate after a certain period of operation: this is most probably due to the deterioration of the surface and can eventually lead to the loss of efficiency.

3.1.3 Gas mixtures: avalanche vs streamer

The mixtures in the first RPCs only included Ar as a multiplier (given its high Townsend coefficient) and organic gases as quenchers. Later, electronegative gases such as freon began to be employed[43], with the aim of limiting the discharge size. When the research and development focused on the rate capability of the detector, strongly quenched mixtures began to be investigated, with the aim of reducing the charge deposited on the electrodes at each hit. A test[49] carried out on a detector filled with pure freon showed that the charge was reduced by three orders of magnitude.

In the context of studies concerning the rate capability, an analysis[48] on the pulse shape of a detector operated with Ar, freon and iso-butane (C_4H_{10}) revealed an interesting feature: the streamer signal (whose amplitude is of

the order of 100 mV), is always preceded by a smaller signal, of the order of a few mV. Such signal can be identified with the arrival at the anode of the avalanche formed by primary and secondary electrons originated during the ionisation and multiplication process. Afterwards, UV photons emitted from ion-electron recombination, together with electrons extracted from the cathode by photons or ions, further ionise the gas and more avalanches form, until a spark eventually occurs and the streamer signal is generated. As it can be observed by comparing Figs. 3.3(a) and 3.3(b), the timing of the avalanche signal is much more precise. This can be explained by the straightforward (somewhat deterministic) nature of the multiplication process; the formation of a spark is instead a stochastic event, with a larger time-jitter. It was also observed that when increasing the high voltage the streamer signal occurs earlier and eventually superimposes to the avalanche one, while when decreasing the voltage below some critical value the streamer signal is not observed.

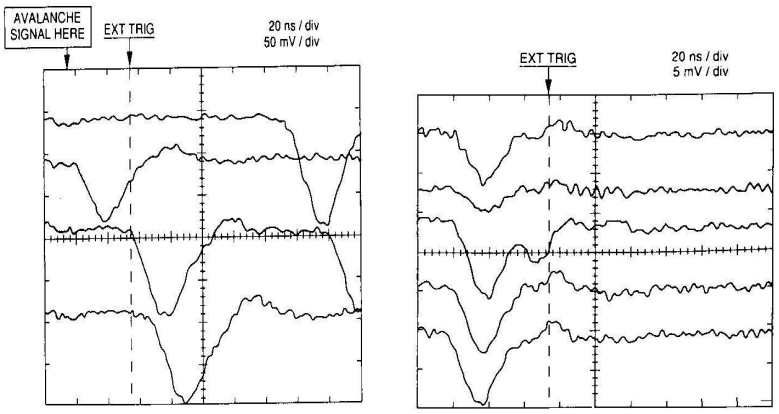

Figure 3.3: A few typical streamer (a) and avalanche (b) pulses from Ref. [48], observed with an oscilloscope connected to the anode of a RPC with a 50 Ω termination. Note the different voltage scale in the two plots.

The transition between the avalanche and streamer regimes has been shown to be discontinuous[50]: the avalanche signal is always present and is approximately proportional to the charge liberated during the primary ionisation, while the streamer signal sets in above a critical voltage, following the avalanche with a delay varying from event to event. Different studies have confirmed the possibility to work in avalanche mode, obtaining a better time

resolution and a smaller charge deposited on the electrodes (of the order of the pC). The price to pay, together with the effects of the avalanche pulse spectrum on spatial resolution and noise rate already discussed in Sec. 3.1.2, is the amplification by external electronics required to obtain signals that can be discriminated with conventional electronics.

From an operative point of view, the difference between the streamer and avalanche modes lies in the gas mixture: avalanche mixtures employ a larger amount of quenchers, preventing the signal to degenerate into a streamer. For the same reason, argon is often substituted with $C_2H_2F_4$, an organic gas that, though easily ionised, exhibits quenching properties. Freon is no longer used due to environmental and security issues. Even in avalanche mode, a certain fraction (of the order of 20%, increasing with HV) of signals degenerate into a streamer. The addition of SF_6 (a strongly electronegative gas) can reduce this effect, so that almost streamer-free mixtures can be obtained.

Finally, the main advantages of streamer and avalanche operation are compared in Tab. 3.1.

Operation mode	Advantages
Streamer	Spatial resolution
	No amplification needed
	Lower noise rate
Avalanche	Time resolution
	Rate capability
	Slower ageing

Table 3.1: Main advantages of streamer and avalanche RPC operation.

From the facts presented in this and the previous section, it emerges how the selection of the operating mode and of other characteristics of Resistive Plate Chambers must be performed on the bases of the specific requirements that must be fulfilled. In the next section, the specific options chosen by the ALICE collaboration for the RPCs of the muon spectrometer will be presented.

3.2 Characteristics of the ALICE muon RPCs

3.2.1 Requirements

The characteristics of the RPCs of the ALICE muon spectrometer reflect the requirements for operation in both the heavy ions and proton-proton runs. These are:

- a high efficiency up to irradiation rates of the order of 100 Hz/cm^2, plus a good safety margin;
- a spatial resolution of the order of the centimeter (i.e. a cluster size as close as possible to 1), to provide a highly selective trigger;
- a time resolution much smaller than the interval between bunch crossings (25 ns), to make sure that all muons produced in a given collision are correctly assigned to the same bunch crossing;
- a detector lifetime compatible with the LHC A-A and p-p program.

After an intense R&D stage, the ALICE collaboration chose to use standard RPCs with low resistivity (a few 10^9 Ωcm) bakelite electrodes 2 mm thick, and a 2 mm gas gap. The gas mixture used will be different for A-A and p-p collisions. In A-A collisions, where the spatial resolution requirements are more stringent, a wet low-gain streamer mixture will be used, made out of:

$$50.5\%\ \mathrm{Ar} \quad 41.3\%\ \mathrm{C_2H_2F_4} \quad 7.2\%\ \mathrm{i\text{-}C_4H_{10}} \quad 1\%\ \mathrm{SF_6}$$

while in p-p collisions, where the main concern is the detector lifetime in the expected high irradiation conditions, a wet, highly-saturated avalanche mixture has been chose, made out of:

$$89.7\%\ \mathrm{C_2H_2F_4} \quad 10\%\ \mathrm{i\text{-}C_4H_{10}} \quad 0.3\%\ \mathrm{SF_6}$$

The reasons for these choices will be discussed in the next section, together with the performances obtained.

3.2.2 Performance

Efficiency and rate capability

In literature, the best rate capability reported with medium resistivity RPCs ($\rho \simeq 10^{10} \div 10^{11}$ Ω cm) operated in streamer mode is about $50 \div 100$ Hz/cm^2 (see e.g. Ref. [46]). These values, though compatible with the ALICE

running conditions, include a small safety margin. The possibility to increase such limits was then investigated[51].

The gas mixture mentioned above was optimised in order to reduce the amount of charge deposited on the electrodes. In the early R&D stage, a streamer mixture similar to the one reported above was selected, with 4% SF_6. The amount of SF_6 has later been reduced due to ageing issues. Such mixture was tested at the CERN SPS with a π beam, with RPCs of different resistivities. As shown in Fig. 3.4, an efficiency as high as 95% for a local rate of about 1 kHz/cm^2 can be achieved with electrodes with ρ=3.5×10^9 Ωcm. It

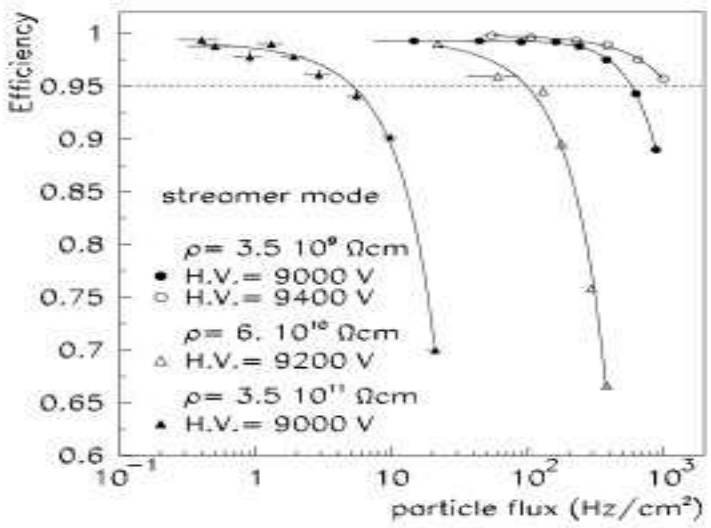

Figure 3.4: Efficiency of a RPC in streamer mode as a function of the local flux, for different values of voltage and resistivity.

was also found that, unlike previous results obtained with higher resistivity electrodes, the efficiency did not decrease within one same burst. Moreover, the current and noise values were found to be compatible with those observed with higher resistivity electrodes. The choice of low resistivity electrodes was then adopted by the ALICE collaboration.

Time resolution

As it was explained in Sec. 3.1.3, the time resolution of RPCs operated in avalanche mode (about 1 ns) is better than the one obtained in streamer mode. To obtain a small time jitter in streamer mode, one has to raise the high voltage well above the knee of the efficiency curve, with possible negative effects on the ageing of the detector.

To improve the time resolution of RPCs in streamer mode, a dual threshold discrimination method was developed (ADULT, A DUaL Threshold[36]). The ADULT technique aims at exploiting both the timing properties of the avalanche precursor and the large amplitude of the streamer signal (Fig. 3.5). This is realised by means of the coincidence between two discriminators: the first one has a low threshold (10 mV), compatible with the avalanche signal, while the second has a high threshold (80 mV), for the streamer. The time reference is provided by the first discriminator, but the signal is validated only if the second discriminator yields a signal within a preset delay from the first.

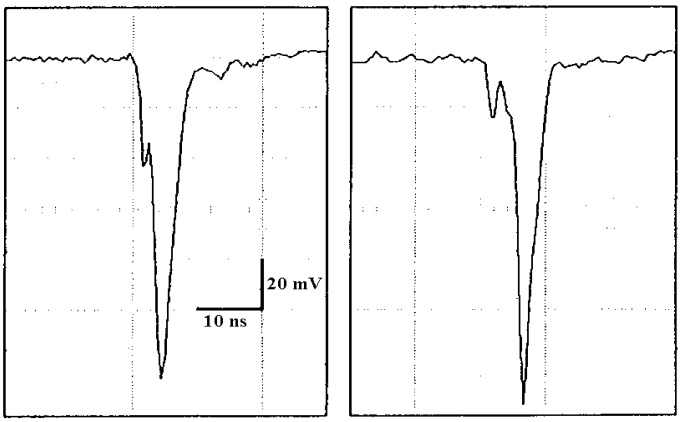

Figure 3.5: RPC streamer signals and avalanche precursors, observed at HV=9200 V with an oscilloscope through a BNC cable with a 50 Ω impedance, during a cosmic ray test. The gas mixture is made out of $Ar/C_2H_2F_4/C_4H_{10}/SF_6$ in the ratios 49/40/7/4.

Such a technique reduces drastically the time jitter, as shown in Fig. 3.6, so that a resolution of about 1 ns can be achieved at reasonable voltage values (Fig. 3.7).

The ADULT method has been successfully implemented[52] on the front-end electronics chip of the RPCs for the ALICE muon trigger (Figs. 3.8(a) and 3.8(b)).

Spatial resolution

The spatial resolution of detectors flushed with the first streamer mixture considered (the one with 4% SF_6) has been investigated[53] by means of a beam test with π from the CERN PS. In that particular set-up, the cluster size turned out to be about 1.1 for strips 2 cm wide. During the beam test, the

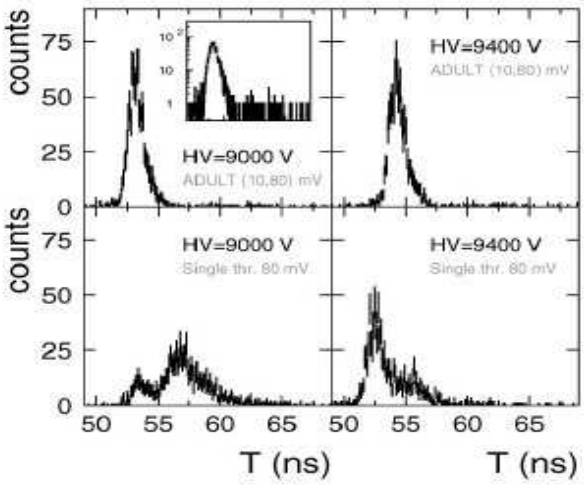

Figure 3.6: Signal time distributions obtained with cosmic rays with the ADULT method (top) and with a single threshold discriminator (bottom), for two different voltages. The ADULT plot at HV=9000 V is also shown in logarithmic scale.

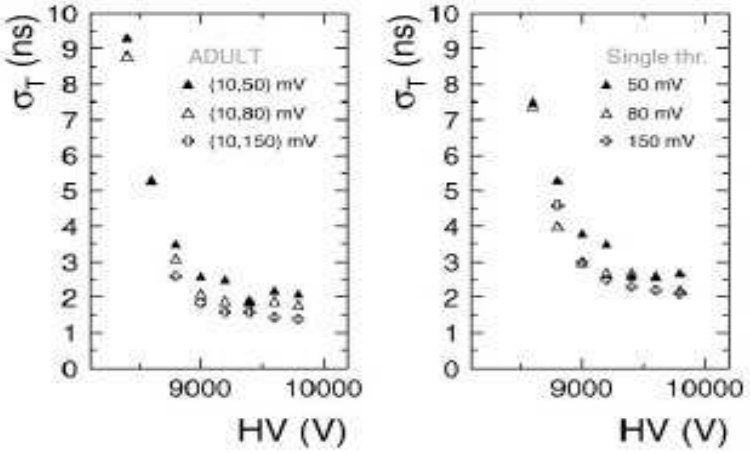

Figure 3.7: RMS of the time distribution obtained during cosmic ray test as a function of the HV, with the ADULT method (left) and with a single threshold (right), for different threshold settings.

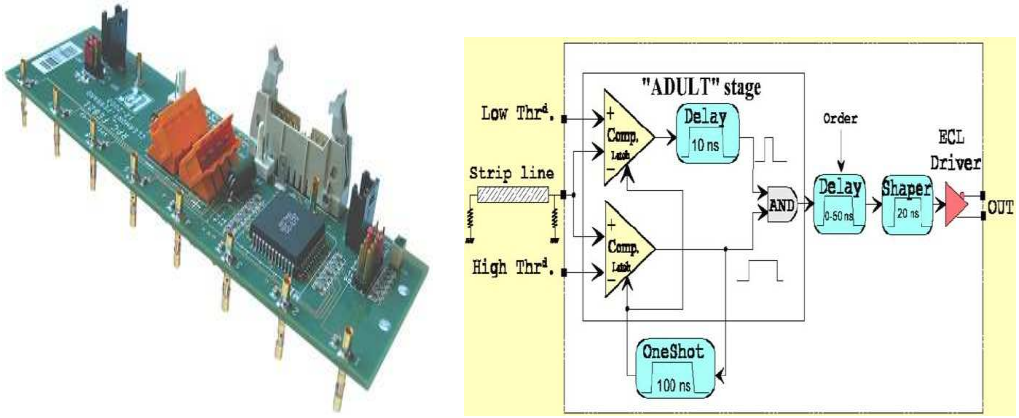

Figure 3.8: The ADULT front-end chip for the RPCs of the ALICE muon trigger (a); block diagram of a single channel of the ADULT chip (b).

spatial resolution of the RPC was evaluated by means of a tracking system composed by three tracking chambers equipped with 5 mm strips, providing a reference to evaluate the RPC spatial resolution, which was found to be (RMS value) 2.3 (5.3) mm with strips 1 (2) cm wide. When, later on, the SF_6 amount was reduced to 1%, a slight increase of the cluster size (about 1.3 with strips 2 cm wide) was observed during beam tests with the X5 muon beam at the CERN SPS[54]. In this case, the cluster size was also measured under high photon-induced counting rate ($\simeq$80 Hz/cm^2) from the CERN Gamma Irradiation Facility (GIF[55]), with very similar results.

A detailed study of the spatial resolution of RPCs operated with the mixture chosen for p-p operation has not been performed yet: the spatial resolution requirements in p-p collisions, though, are much less stringent than in A-A, the expected muon trigger rate being about two orders of magnitude lower.

3.2.3 Ageing

A-A collisions

Ageing tests[56, 57] with the streamer mixture have been carried out at the Gamma Irradiation Facility, to evaluate the effects of long-term operation on the detectors. The availability at GIF of high irradiation rates allows one to simulate in a few months of data-taking an exposure compatible with the one associated with years of operation at the LHC.

The first studies were carried out with prototypes with different characteristics, in order to understand what parameters had more influence on ageing. The main choices adopted by the collaboration were the following:

- the reduction of SF_6 content from 4% to 1%: chemical analysis of exhaust gas revealed the formation of HF, and an analysis of the electrodes revealed corrosion by fluorine. Indeed, some correlation was noticed between the SF_6 content and the degradation of the performances of the detector;

- the adoption of a double linseed oil coating on the electrode surface, to prevent surface damage;

- the addition to the mixture of about 1% water vapour (wet mixture), to prevent resistivity increase.

The overall result was that the prototypes showed constant performance up to 100 Mhits/cm^2, i.e. a current per surface unit of about 50 mC/cm^2. Afterwards, an important increase of the dark current was observed. If one assumes a realistic estimate of about $1 \div 5$ Hz/cm^2 for the hit rate on the detectors in Pb-Pb, and about 30 Hz/cm^2 in Ar-Ar collisions, the detector lifetime can be considered compatible with 10 years of heavy ion operation[1] at the LHC with these colliding systems, including a safety factor of 2.

An extensive ageing test on a full-size pre-production RPC (labelled RPC1) operated with the final streamer gas mixture was carried out at GIF. The setup for the test is shown in Fig. 3.9. The efficiency, measured by means of a cosmic ray telescope, has been monitored as a function of the integrated hits. Periodical data-taking at source-off has also been performed, to measure the dark current, the dark rate and the efficiency without irradiation. The results are shown in Fig. 3.10: it appears that, while the dark rate remains small and constant (below 0.4 Hz/cm^2), the dark current increases from the initial small values up to about 15 μA. The dark current increase, unjustified by the dark rate is a puzzling effect, observed in the tests with prototypes as well, which has not been explained yet. However, the performances of the detector remain satisfactory up to about 100 Mhits/cm^2. No efficiency loss is observed with source-off, while a decrease is observed with source-on. The efficiency was measured on a limited surface by means of a cosmic ray trigger set-up. In chapter 5, the results of a high granularity efficiency test performed with a dedicated test station on the same detector after the long-term exposure will be presented.

[1] One month per year, see Sec. 2.1.1.

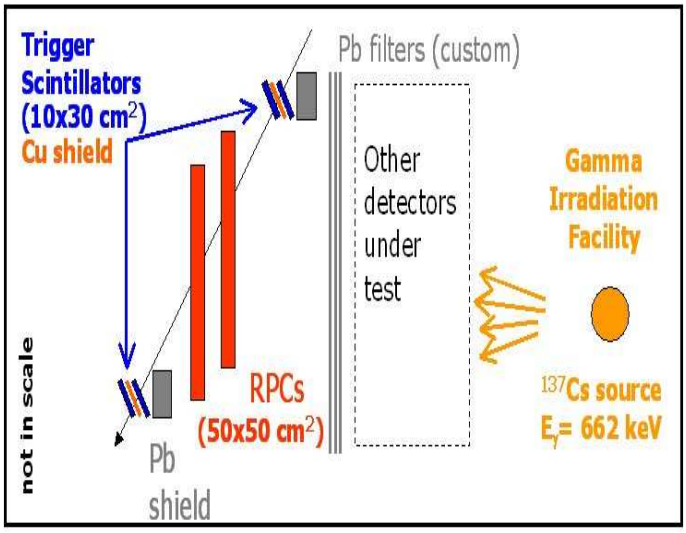

Figure 3.9: The setup for the ageing tests at the Gamma Irradiation Facility.

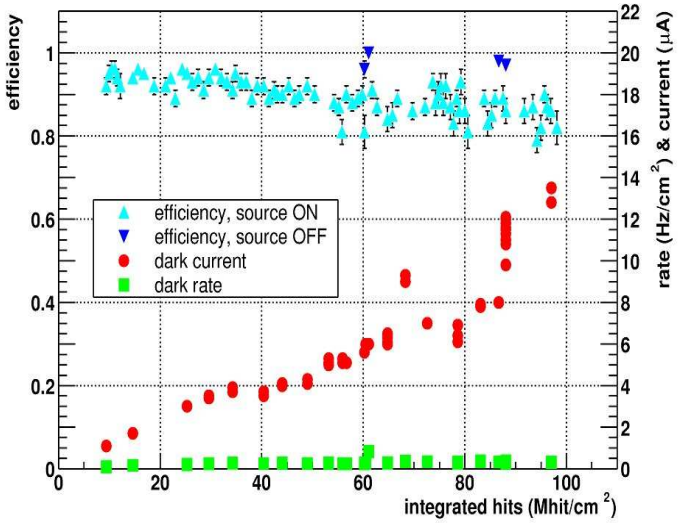

Figure 3.10: Evolution of efficiency, dark current and dark rate as a function of the integrated hits, for the full size RPC labelled as RPC1 in the text, operated at voltages between 8050 and 8200 V.

p-p collisions

The ALICE data taking scenario in proton-proton collisions is rather different than in A-A collisions. There are two main reasons that lead to the choice of a different gas mixture and operation mode for p-p collisions:

- the expected muon trigger rate is much lower: the momentum resolution requirements can be relaxed, and thus a larger clustersize (i.e. a slightly worse spatial resolution) can be accepted;
- the hit rate on the chambers will be higher, due to the high beam intensity: the main source of hits is the interaction of the beam with residual gas in the beam pipe[58]. In particular, a few detectors are expected to be irradiated up to a few tens of Hz/cm^2 [59]. Moreover, the data-taking time per year in p-p collisions will be 10 times higher than in A-A. The number of integrated hits will then be much higher: to limit ageing effects, the charge deposited on the electrodes must be reduced.

The two above facts, i.e. the possibility to accept a larger clustersize and the need to reduce the charge, led the collaboration to consider avalanche operation in p-p collisions. Avalanche operation is possible with the ADULT chip described earlier in this chapter, provided that the high threshold is set equal to the low one. Since a threshold lower than 10 mV can not be set on the ADULT chip, the avalanche mixture must be highly saturated, in order to provide signals large enough to be read with the same front-end electronics as in A-A collisions.

After an intense R&D program[54, 60], a mixture has been selected, very close to the final one reported at the beginning of this section, with a 2% SF_6 content. Preliminary tests with cosmic rays have shown that for a voltage range of about 600 V above the working point, less than 20% of the signals degenerate into a streamer discharge (Fig. 3.11); beam tests at the CERN SPS X5 have shown that such a mixture satisfies the ALICE requirements for p-p running, even under high irradiation rate.

Ageing tests[54] have been performed at GIF-on a 50x50 cm^2 prototype. The setup of the test is essentially the same as for the streamer test, shown in Fig. 3.9. After about 225 Mhits/cm^2, the detector showed some instability, which was believed to be related to the high working voltage required for operation. To overcome this problem, the SF_6 content was reduced to 0.3%. The performances of the mixture have been checked again without significant effect other than the desired shift of the efficiency curve towards lower values.

Two 50x50 cm^2 prototypes, which in the following will be labelled RAV3 and RAV4, have been tested for ageing at a voltage of 10050 V and 10100

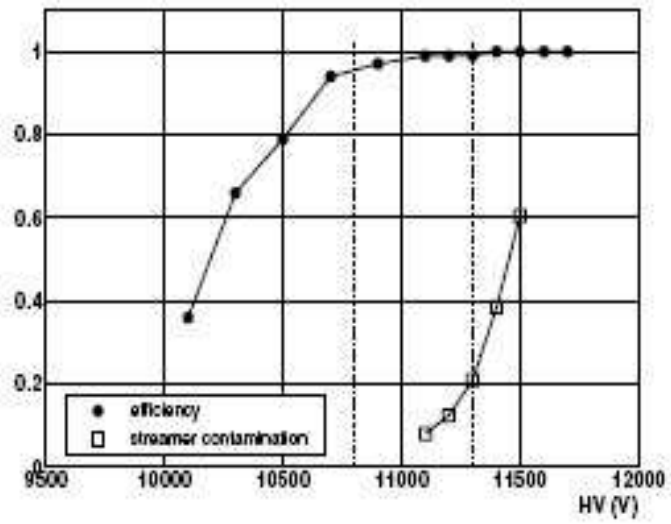

Figure 3.11: Efficiency and streamer contamination as a function of HV for a protoype operated with a $C_2H_2F_4/C_4H_{10}/SF_6$ gas mixture in the ratios 88/10/2. The two vertical lines correspond to 90% efficiency and 20% streamer contamination, respectively.

V respectively. The detectors have integrated 570 Mhits/cm^2 (RAV3, Fig. 3.12) and 540 Mhits/cm^2 (RAV4, Fig. 3.13). In both cases, instability occurred at some point, but it was found to be due to bad insulation (RAV4) and to a problem with the water vapour control system (RAV3): after the malfunctions were fixed, the detectors recovered their normal behaviour.

The efficiency of both prototypes is fairly constant at a high value ($\simeq 98\%$) when measured at GIF-off, while a slight decrease occurs under irradiation: the efficiency, however, never decreases below 95%. The dark rate of RAV4 shows a slight increase as a function of the integrated hits; this is not observed for RAV3. The rate does not exceed 2 Hz/cm^2. The behaviour of the dark current reflects the behaviour of the dark rate, the maximum value reached being 3 μA.

If one assumes a mean rate on the RPCs of 10 Hz/cm^2 in p-p collisions[59], the detector lifetime is compatible with at least five years of operation in the ALICE p-p program. Moreover, chemical analyses on the exhaust gas performed during the ageing test revealed no trace of HF and a percentage of impurities much smaller than that of other mixtures previously tested.

The two prototypes RAV3 and RAV4 have also been tested with the test station developed for the tests of the RPCs of the final production, to evaluate more accurately the effects of ageing. The results will be presented

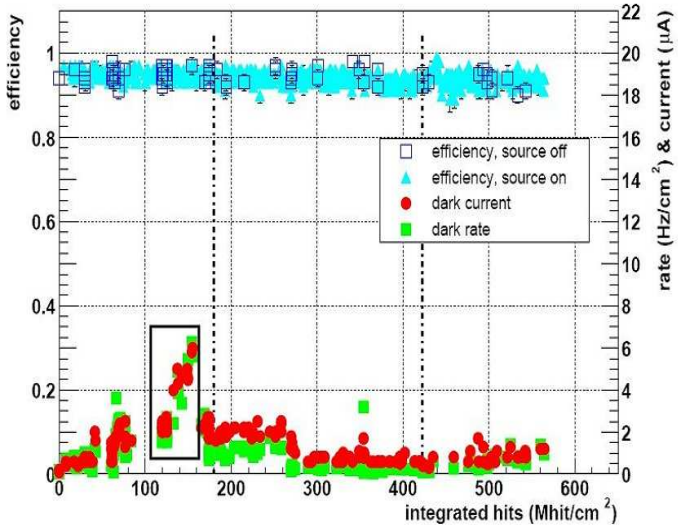

Figure 3.12: Evolution of efficiency, dark current and dark rate as a function of the integrated hits, for the 50x50 cm^2 prototype labelled as RAV 3 in the text, operated at 10050 V, 970 mbar and 20°; the region in the black frame corresponds to a period of high current and rate, due to a problem with the water vapour control system.

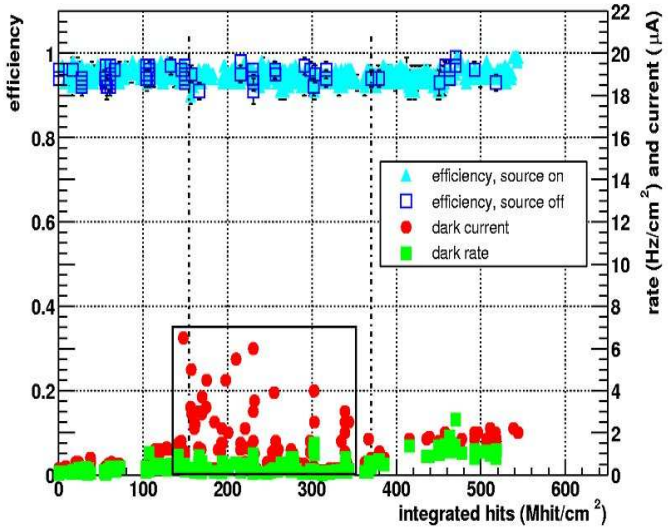

Figure 3.13: Evolution of efficiency, dark current and dark rate as a function of the integrated hits, for the 50x50 cm^2 prototype labelled as RAV 4 in the text, operated at 10100 V, 970 mbar and 20°; the region in the black frame corresponds to a period of unstable current, due to bad insulation.

in Chap. 5.

Chapter 4

Characterisation of the final detectors

4.1 Production and quality assurance

4.1.1 Gas volumes

In order to start the final production[62] of the ALICE RPCs, about 250 bakelite sheets (2 mm thick) were produced by Frati Laminati (Gambolò, Italy) and their resistivity measured in Torino in controlled climatic conditions (T$\simeq$ 20°, relative humidity$\simeq$ 40%) with the Hewlett-Packard high resistivity meter HP4339B: 50 V are applied through brass electrodes kept in contact with the plate by means of conductive rubber, with a 10 Kg lead weight on top to assure constant pressure. For calibration purposes, in some cases measurements were repeated with conductive gel, which ensures intimate contact between the meter's electrodes and the bakelite: the measurements performed with rubber where found to be a factor 2 higher than those performed with gel. At the same time, the sheets were visually inspected to detect deep bumps and scratches on the surface. The sheets were then labelled and sent to Riva (Cinisello Balsamo, Italy) to be cut to the desired shape by milling. Sheets with lower resistivity have been assigned to S and C detector types, since such detectors will be positioned near to the beam pipe, where a higher rate capability is required (see Secs. 3.1.2 and 3.2.2 for a discussion of the relationship between resistivity and rate capability).

The gas gaps were built by General Tecnica (Colli, Italy). Here, bakelite sheets are cleaned and once again visually inspected. Then, graphite painting (surface resistivity 100 KΩ/square) is applied on the external sides, leaving an 11 mm wide graphite-free contour along the edges, to prevent unwanted discharges. The glueing of sheets with internal spacers (arranged in

a 10×10 cm^2 matrix) and external frames is performed by means of dedicated machines; finally, insulating PET sheets 190 μm thick are glued on the external surface, together with U-shaped PET ribbons along the volume edges.

After production, the volumes are filled with a linseed oil/n-pentane 40/60 mixture and slowly drained out. Then, filtered air circulation at 28° is forced inside the gaps, to ensure linseed oil polymerization. The procedure is performed twice, in order to obtain a double linseed oil layer.

4.1.2 External mechanics

The complementary mechanics have been manufactured in the INFN Torino laboratories.

The readout strip and ground planes are etched on a 0.19 mm thick mylar foil, coated with a copper layer 20 μm thick; a milling machine rotating at 6000 rpm grooves the mylar foil to a depth of 0.1 mm with a longitudinal speed of 4000 mm/min. Then, engraved strips and ground foils are glued on opposite sides of a 3 mm thick foam plate.

The external stiffener planes are made out of 10 mm thick nomex sheets. In order to connect the readout strips to the front-end electronics, stiffener and strip planes are coupled and drilled; then, cylindrical connectors for the front-end electronics are inserted. Finally, L-shaped aluminium profiles are fixed along the long edge, to support the screws for the final assembly and to allow space for the gas pipes.

4.1.3 Final assembly

After manufacturing at General Tecnica, the gas gaps were transported to the OPERA[63] RPC test stand at the INFN-LNGS laboratories, to check gap tightness and spacer glueing. For the first test, the chamber is filled with argon with an overpressure of 6 mbar: then, the overpressure is monitored for at least 300 s. A volume is accepted if the difference between the initial and the final measure is less than 0.1 mbar: 2% of the volumes were rejected. To check the correct glueing of the spacers, a system of weights impinging on the spacers positions is used. If one spacer is not glued, in its position the overpressure inflates the gap to a value greater than 2 mm: the weight brings it back to the original value, thus increasing the pressure inside the gas volume. Unglued spacers can then be detected by monitoring the pressure. A volume is accepted if it has up to two non-adjacent unglued spacers; 6% of the volumes presented one unglued spacer, and 1% two non-adjacent unglued spacers.

The gas volumes are then transported to Torino, where they are assembled with the external mechanics. The first production session is now over, but more detectors are to be produced in order to fullfill the requirements in terms of spare chambers (see Sec. 4.3.5).

4.2 Testing the final detectors

The tests on the detectors of the final production have been carried out at the INFN laboratories in Torino. The aims of such tests are:

- to make sure that the final detectors meet high quality standards, thus validating on a large scale the choices made by the collaboration in the R&D stage;
- to characterise all the produced detectors so that their characteristics are known and available to the collaboration;
- to choose the best detectors among those produced in order to fulfill the ALICE requirements shown in Tab. 4.1;
- to have a first estimation of the voltage at which each detector should be operated in order to have it fully efficient.

Type	Required in ALICE	Required spares
C	16	8
L	48	12
S	8	8
Total	72	28

Table 4.1: Number of detectors of types C, L and S required for the ALICE trigger system.

The efficiency measurements have been performed with cosmic rays. It has to be pointed out that the aim of the tests does not include the absolute measurement of the detectors' efficiency, for two main reasons:

- the environment in which the detectors have been tested is different from the one in which they will be operated, and the measurement of efficiency is affected by systematics which will be discussed later on in this chapter;

- the efficiency of a RPC is subject to changes in time due to ageing: the measurement of efficiency shall be performed periodically during operation, with methods based on the ALICE data[64].

For the above reasons, the tests focused on aspects such as the intrinsic noise of the detectors, the current drawn during operation and, above all, the uniformity of performances of the detectors: to prevent the trigger system from biasing the measurement, it is important to have the whole trigger station equally efficient. Since the voltage of each of the 72 detector is regulated separately, it is possible to operate each detector at the proper voltage in terms of noise, efficiency and current. The tests performed in Torino have given an idea of what the best voltage choice is for each detector. The ideal working voltage shall anyway be determined during the commissioning and data-taking phases. What needs to be avoided is to have detectors with non-uniform behaviour throughout their surface, since this would lead to differences in efficiency that can not be controlled externally. This is why the measurement of efficiency is performed on a local scale, by dividing each detector in virtual cells and measuring the efficiency separately for each cell.

Here is the complete list of all tests carried out:

- 1) the detection of possible gas leaks;
- 2) the electrodes resistivity under working conditions, measured with the argon method ;
- 3) the current-HV curve (ramp-up) and the detection of possible leakage ohmic currents;
- 4) the efficiency-HV curve in cells $\simeq$ 20x20 cm^2;
- 5) the mean noise rate and the noise map of the detector, with the autotrigger method;
- 6) the efficiency map at working HV, with a granularity of $\simeq$ 2x2 cm^2;
- 7) the dark current absorbed at working HV.

The tests numbered 1), 2) and 3) will be described in Sec. 4.2.1; the tests numbered 4) and 5) will be described in Secs. 4.2.2 and 4.2.3; the tests numbered 6) and 7) will be described in Sec. 4.2.4.

4.2.1 Preliminary tests

Gas leaks

Before being tested, the detectors are checked for gas leaks: the gas gap is filled with argon, the gas inlet is closed and the gas outlet connected to a U-shaped pipe partially filled with water. Gas leaks can be detected by monitoring the level of the water in the pipe during a time interval of about one hour. If the level of the water has moved by a few mm, the gas gap is either rejected or sent back to the production bench.

Resistivity measurement

After being checked for gas leaks, the detectors are flushed with pure argon in order to measure the electrodes resistivity. When the voltage applied to the argon-filled gas gap reaches a value of about 2000 V, the gas begins to conduct free charges: UV rays emitted in the recombination of Ar^+ ions with free electrons in the gas, not absorbed by any quencher gas, feed further ionisation, until the gas becomes a conductive plasma that short-circuits the electrodes. The resistance of the electrodes can then be measured from the slope of the current-voltage curve (Fig. 4.1).

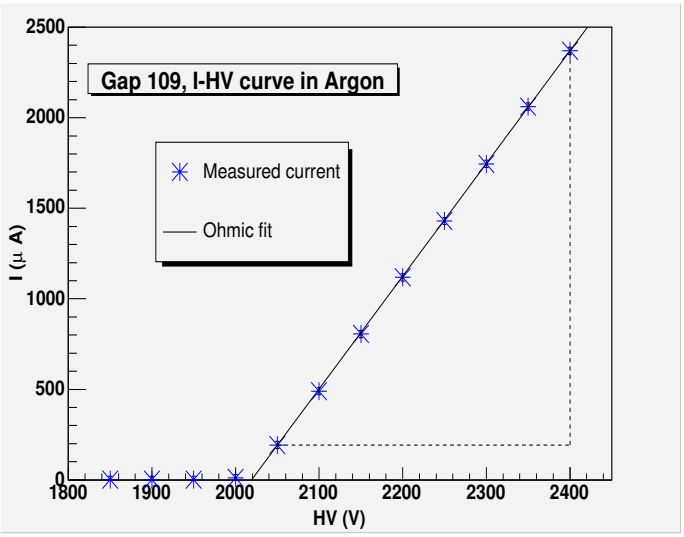

Figure 4.1: Current voltage-curve of a RPC flushed with pure argon. The trend is ohmic above HV $\simeq$ 2000 V.

The two electrodes (2 mm thick) can be considered as a series of resistors of length $l = 2$ mm, surface S and resistivities ρ_1 and ρ_2. The mean resistivity

$\overline{\rho} = \frac{1}{2}(\rho_1 + \rho_2)$ of the two electrodes can then be calculated from the measured resistance:

$$\overline{\rho} = \frac{RS}{2l} \tag{4.1}$$

The resistivity of the bakelite electrodes has an exponential dependence on the temperature[65]. Such dependence is accounted for by the following expression[1]:

$$\rho(T) = \rho(T_0) 4.4^{\frac{T_0 - T}{12^\circ}} \tag{4.2}$$

where $\rho(T_0)$ is the resistivity measured at some reference value T_0.
Resistivity measurements carried out at different temperatures can be compared after rescaling to the same temperature according to Eq. 4.2.

Ramp-up

Once the gas gap has been flushed for the first time with the streamer mixture described in Sec. 3.2, the detector is connected to the HV. The ramp up procedure is the following: starting from 3000 V, the applied voltage is increased by steps of 1000 V. When the absorbed current becomes larger than 1 μA, the detector is left at that voltage for a while until the current decreases: some time is needed for the detector to burn impurities such as dust on the surface of the bakelite sheets, which result in a temporarily higher current value. The procedure is considered successful if the current is lower than 1 μA at HV = 7000 V. If this doesn't happen, it may be due to a not perfect insulation of either the electrodes or the mechanical structure, leading to an ohmic leakage current: the detector is either rejected or sent back to the production bench.

4.2.2 Efficiency measurements

Effective voltage

Since temperature and pressure affect the performances of resistive plate chambers, a correction is needed: the applied value V is varied every 15000 events ($\simeq$ 10 minutes) according to T and p, in order to keep constant the effective voltage V_{eff}, defined as in Eq. 3.3:

$$V_{eff} = V \frac{T}{T_0} \frac{p_0}{p}$$

with $T_0 = 20^\circ$C, $p_0 = 1$ bar.
All voltages mentioned in the following should be taken as effective voltages.

[1] The coefficients in the formula have been provided by the producer of the bakelite sheets (Frati Laminati).

Set-up

The detector efficiency is measured with cosmic rays (muons) by means of a dedicated test station (Fig. 4.2), composed of:

- three planes of nine scintillators each, covering an area of 90x150 cm^2;
- two tracking RPCs (172x87 cm^2 each) ;
- four test slots where the RPCs to be tested are placed.

Given the surface of the tracking RPCs and the limited number of available front-end boards and read-out channels, two half-RPCs at a time can be tested: the detectors have thus been tested two by two, while the two remaining slots have been used for the preliminary tests described in Sec. 4.2.1. A moving support structure with wheels has been developed, so that it is possible to select the half-detector to be tested just by moving the trigger system (i.e. the scintillators and the tracking RPCs), without moving the detector itself.

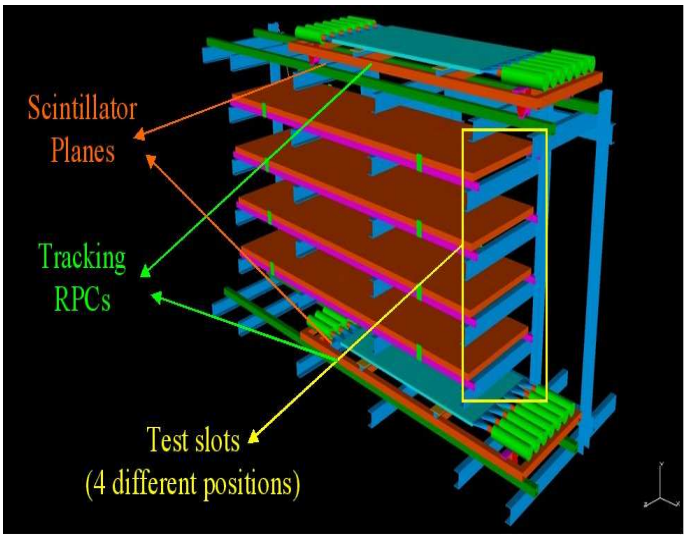

Figure 4.2: The Torino test station for the final RPCs of the ALICE Dimuon Arm

Readout and DAQ

The front-end electronics used for the test is the same in ALICE: the detectors have been equipped with the ADULT front-end boards described in Sec.

3.2.2. The two half-detectors on the testing planes are read out by means of a set of Coincidence Registers, while the signal from the tracking RPCs is read out by means of a set of FERA ADCs with zero suppression. The scintillator planes are read out by means of discriminators. The trigger is issued if at least one strip per each plane of the two tracking RPCs and at least one scintillator per plane have been fired. The logical scheme of the electronic chain for the tests is reported in Fig. 4.3. The data acquisition

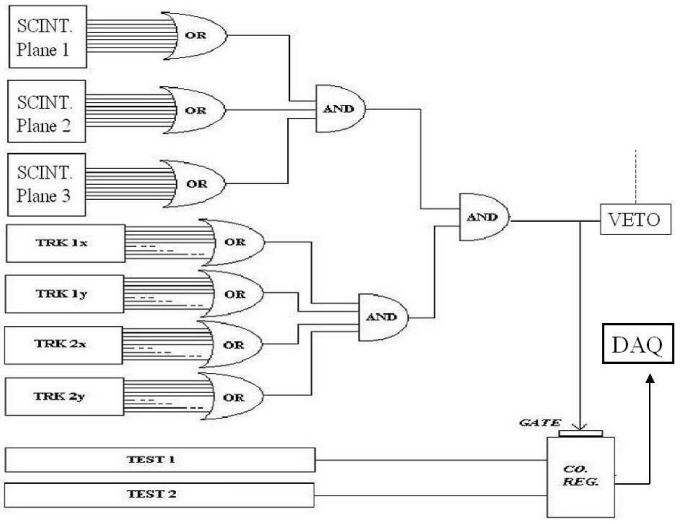

Figure 4.3: Logical scheme of the electronic chain for the measurement of efficiency with the Torino test station.

and monitoring are performed on a terminal on the site, by means of the DATE[61] software.

Algorithm

The two tracking RPCs are read on both sides with orthogonal 2 cm wide strips: with the spatial information provided by these tracking RPCs, the cosmics rays can be tracked to obtain information on the impact point on the test slot planes and to perform a local measurement of the efficiency (Fig. 4.4). Only events with only one cluster per plane in the tracking RPCs are selected (to avoid ambiguities); the cluster size is required not to be larger than 2 strips (to improve resolution and cut off cosmic ray showers).

If (x_1,y_1) and (x_2,y_2) are the impact coordinates on the two tracking RPCs (located at heights z_1 and z_2), the expected impact coordinates on the two RPCs under test (located at heights $z_{test,1}$ and $z_{test,2}$) will be (i =1,2):

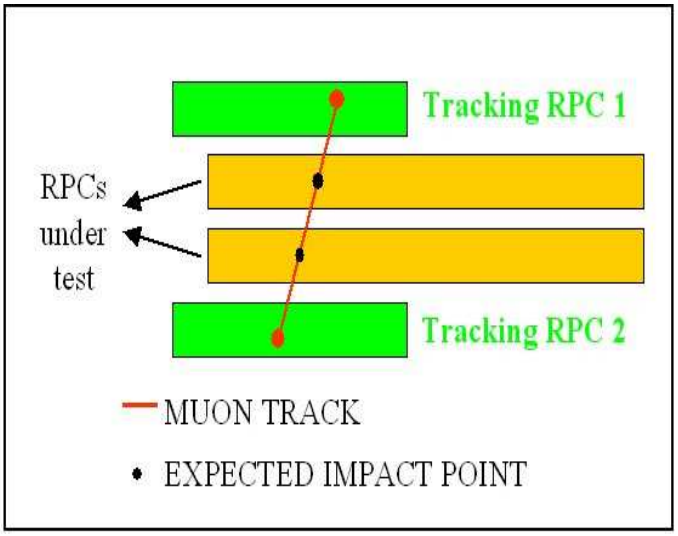

Figure 4.4: Local measurement of the RPC efficiency by means of two tracking detectors.

$$x_{test,i} = x_1 + \frac{z_{test,i} - z_1}{z_2 - z_1}(x_2 - x_1); \quad y_{test,i} = y_1 + \frac{z_{test,i} - z_1}{z_2 - z_1}(y_2 - y_1) \quad (4.3)$$

The resolution on the position reconstruction has been evaluated by means of Monte Carlo simulations. In principle, such resolution is different from test slot to test slot, depending on the z-coordinate of the slot itself. The simulated resolution for the four different slots is shown in Fig. 4.5. As it can be observed, the RMS of the distribution is about 4 mm in all slots, leading to a FWHM (in the gaussian approximation) of about 1 cm. This is a slightly optmistic estimate, since the simulation only takes into account the effect of the discretisation of the measured impact coordinates x_i and y_i, but not the multiple scattering of the muons.

Once the impact point on the testing plane has been reconstructed, the event is assigned to a cell on a grid defined on the testing plane. The efficiency of each cell will be calculated by dividing the number of detected cosmic rays in that cell by the number of events assigned to the cell. Given the above mentioned resolution, the detector area can be safely divided in cells as small as 2x2 cm^2.

The alignment of the testing planes with the reference frame defined by the tracking RPCs is performed offline, by means of the distribution of the difference between the expected impact coordinates on the testing planes

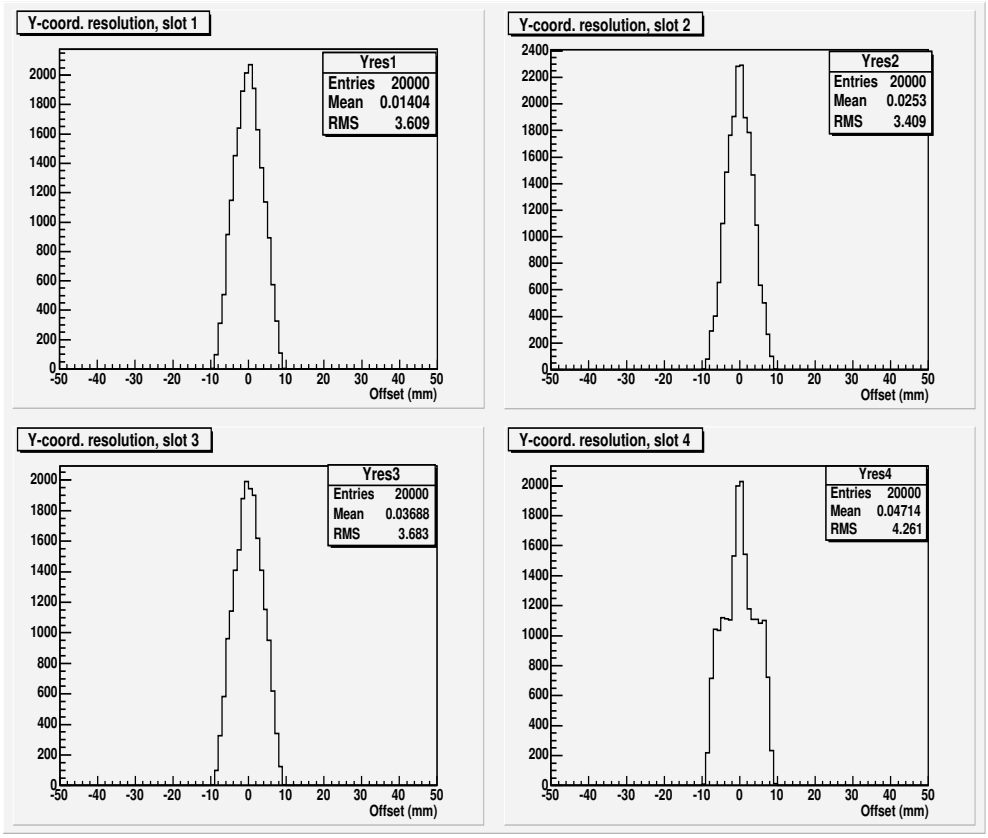

Figure 4.5: Monte Carlo distribution of the difference between real and reconstructed impact coordinates for different test slots. The narrow peak visible on the distribution of slot 4 is due to events with clustersize 2 (i.e. better resolution, as explained in Sec. 3.1.2) on the lower tracking RPC, located right below slot 4.

and the coordinates measured with the RPCs under test: the peak value is the offset between the zero of the reference frame and the edge of the tested RPC. Once this value is known, it can be included in the reconstruction of the position, so that the distribution is peaked around zero (Fig. 4.6). For the alignment procedure, events with one cluster only per plane in the RPC under test are selected.

The distribution of the offset between the expected impact coordinates and those measured by the RPCs under test can also be used to evaluate the error on the position reconstruction with the RPCs under test: the FWHM of the distribution is less than 2 cm with 2 cm wide strips (Fig. 4.6):

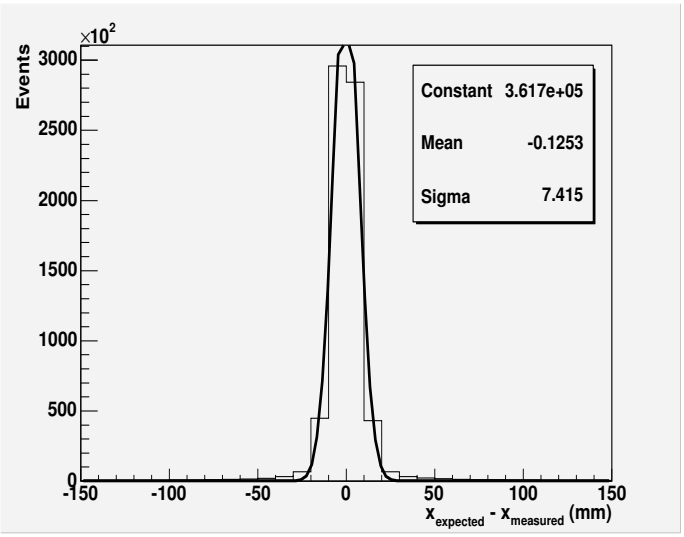

Figure 4.6: Distribution of the difference between expected and measured coordinates for a RPC operated at 8200 V, with 2 cm wide strips.

The event is considered detected if, on both planes, the offset is less than a tolerance value t. An arbitrary though effective expression has been chosen, that takes into account both the strip pitch of the tracking chambers (2 cm) and the strip pitch w of the RPC under test, in the region where the incident cosmic ray has crossed it:

$$t = \sqrt{(1.5w)^2 + (1.5 * 2cm)^2} \tag{4.4}$$

so that:

- for strips 1 cm wide, t = 3.4 cm;
- for strips 2 cm wide, t = 4.2 cm;

- for strips 4 cm wide, t = 6.7 cm;

If more than one cluster is present on the RPC under test, the nearest to the expected impact point is chosen for the evaluation of the offset.

It has been observed that the efficiency does not depend strongly on the tolerance value, provided that such value is larger than the detector resolution: the only effect of such cut is to remove false coincidences between triggered cosmic rays and noise counts of the RPCs under test.

It has been found that such a method implies some systematics on the measurement of efficiency, due to possible false triggers of the tracking RPCs, or to scattering of the muons off the structures of the test station. Such effects will be discussed more in detail in Sec. 4.2.3. As it will be shown, the systematic error on the measurement of efficiency can be estimated to be about 3÷4%: as it has already been pointed out, the efficiency measurements presented here are not meant to evaluate the absolute RPC efficiency, but the uniformity of the efficiency throughout the surface of the detector.

Statistical error

The statistical error on the measurement of efficiency can be calculated by means of the second momentum $\sqrt{np(1-p)}$ of a binomial distribution, where the probability p is estimated with the efficiency ϵ itself, and n is the number of events:

$$\sigma_\epsilon = \frac{\sigma_{n_{detected}}}{n} = \sqrt{\frac{\epsilon(1-\epsilon)}{n}} \tag{4.5}$$

Such formula accounts for the statistical fluctuations of the number of detected particles for a given efficiency. It can be applied safely only if n is larger than a cutoff value depending on ϵ. In App. A it will be shown how the limits of appliability of Eq. 4.5 are essentially respected by the efficiency measurements described here.

Efficiency curves

The efficiency as a function of the high voltage is measured in 21 different cells for each half-chamber: the surface of the cells is about 20x20 cm^2. This is done by using the information on the expected impact point obtained via the tracking procedure described above. The efficiency curve can be different from cell to cell (Fig. 4.7). Each curve is fitted to a suitable function, i.e. the integral of an asymmetric gaussian distribution:

$$\epsilon(HV) = \epsilon_{max} \frac{\int_{HVmin}^{HV} e^{-(t-\mu)^2/2\sigma^2(t)}\ dt}{\int_{HVmin}^{HVmax} e^{-(t-\mu)^2/2\sigma^2(t)}\ dt} \tag{4.6}$$

where

$$\sigma(t) = \sigma_1 + \sigma_2 \frac{t - \mu}{\sigma_1} \tag{4.7}$$

Once the fit parameters are extracted, four more parameters are evaluated, which will be used to characterise the curve:

- ϵ_{max}, i.e. the maximum efficiency reached by the detector;
- HV_{50}, i.e. the voltage value at which the detector has 50% efficiency;
- HV_{90}, i.e. the voltage value at which the detector has 90% efficiency;
- the slope of the curve in the linear region.

The spread of such parameters can be used to evaluate the uniformity of the detector performance (Fig. 4.8). As it will be shown in Sec. 4.2.3, the ϵ_{max} and HV_{90} parameters are quite sensitive to the systematic errors of the efficiency measurement; the uniformity of the detectors is better evaluated by means of the slope and HV_{50} parameters.

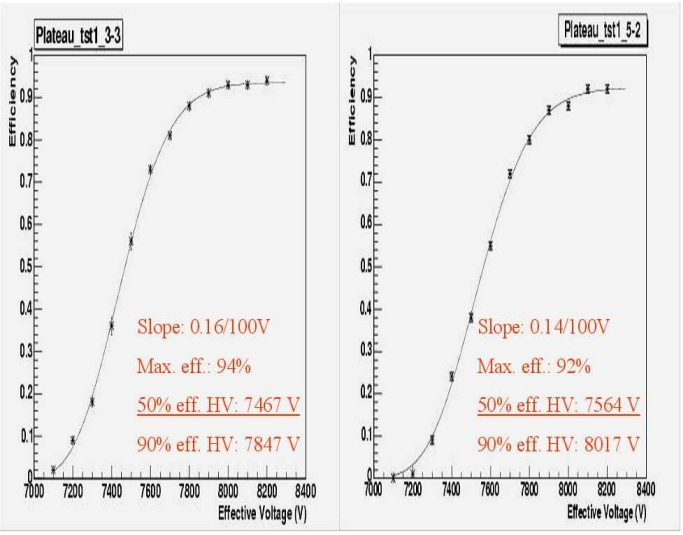

Figure 4.7: Efficiency curves for two 20x20 cm^2 cells of a same RPC.

Efficiency maps

To evaluate even better the uniformity of the detectors, and to detect any imperfection, though small, efficiency maps are measured at two voltage values, 8200 V and 8100 V: such values are right above the working voltage for most detectors.

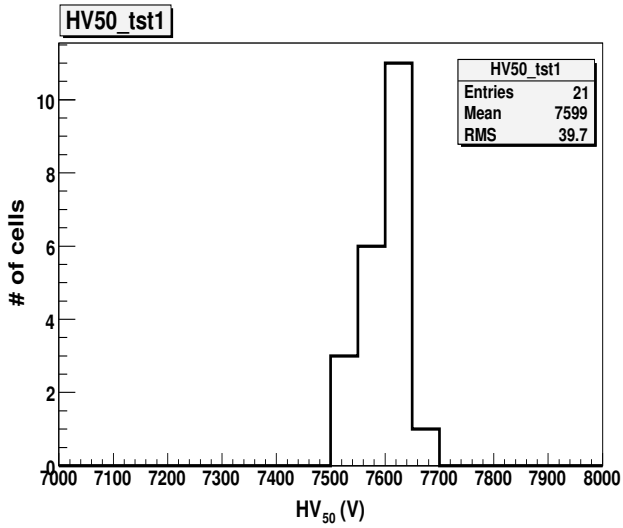

Figure 4.8: Distribution of the voltage at which the detector reaches 50% efficency for cosmic rays, over 21 20x20 cm^2 cells of a half-chamber.

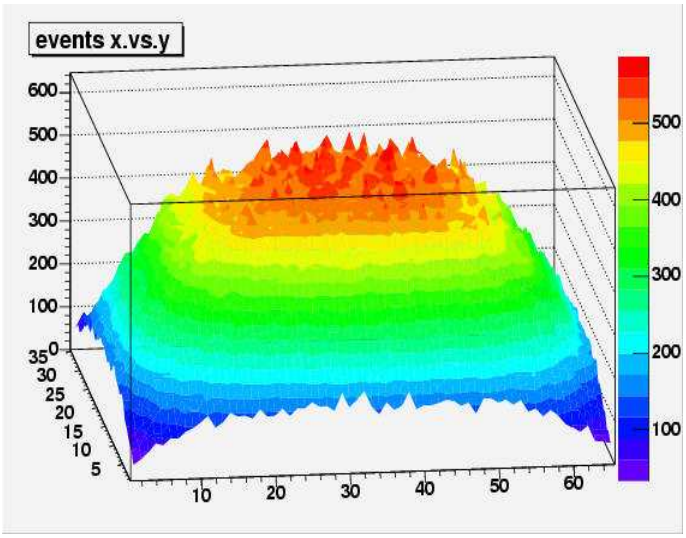

Figure 4.9: Distribution of triggered events for efficiency measurement over the surface of a half chamber. Units are given in cells. The area of the cells is 2x2 cm^2.

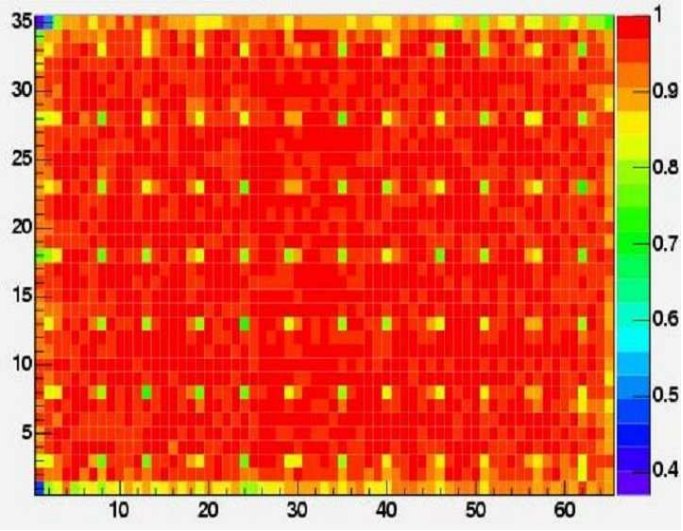

Figure 4.10: Efficiency map of a half chamber operated at 8200 V. Units are given in cells. The area of the cells is 2x2 cm^2.

The cells for efficiency maps are about 2x2 cm^2 large. With a 1000000 events run ($\simeq$ 10 h acquisition time), the statistics is of about 500 events in central cells, 100 in peripheral cells, 50 in the very side cells (Fig. 4.9). The resulting statistical error at working voltage ranges from 1% to 4% according to the position of the cell.

As it was mentioned above, the resolution is of the order of the centimeter, so that, in the efficiency map (Fig. 4.10), even the spacers that keep the distance between the electrodes constant (whose diameter is 1 cm) can be resolved.

The efficiency has also been measured separately for the two orthogonal X and Y strip planes. In such a way, it has been possible to separate efficiency problems due to the readout planes (e.g. short-circuited strips, unstable electric contact or bad insulation) from problems arising from the gas gap: if the problem is seen on both readout planes, it is most probably due to the gas gap, while if it is limited to one of the planes (Figs. 4.11(a) and 4.11(b)), the problem is most likely due to the strips. In this last case, the detector can be opened to check the readout planes and detect any imperfections. About 5% of the readout planes presented this kind of problems.

One of the most common causes of localised efficiency loss is the presence of bumps on the surface, causing a locally wider gap between the electrodes (i.e. a lower electric field): such an efficiency loss can be recovered by operating the detector at a higher voltage, so that the electric field is high enough

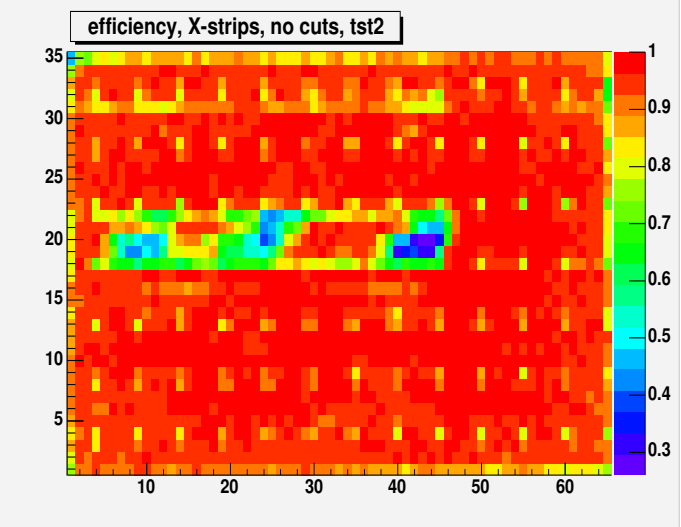

(a)

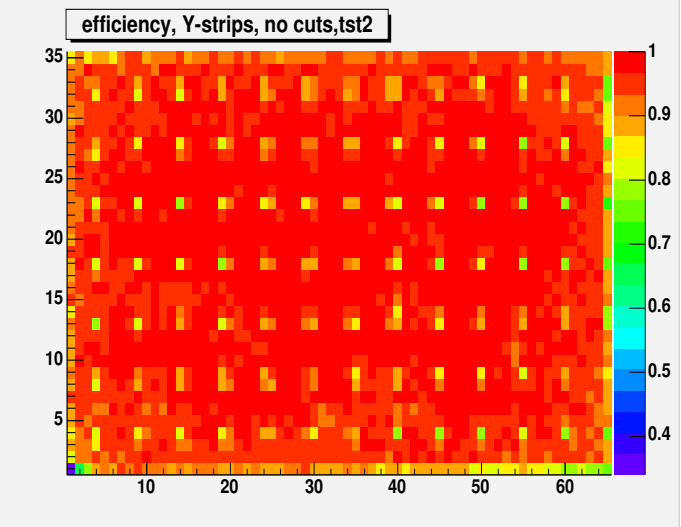

(b)

Figure 4.11: Efficiency map of a half chamber operated at 8200 V, measured with the signal from the X-plane only (a) and with the signal from the Y-plane only (b).

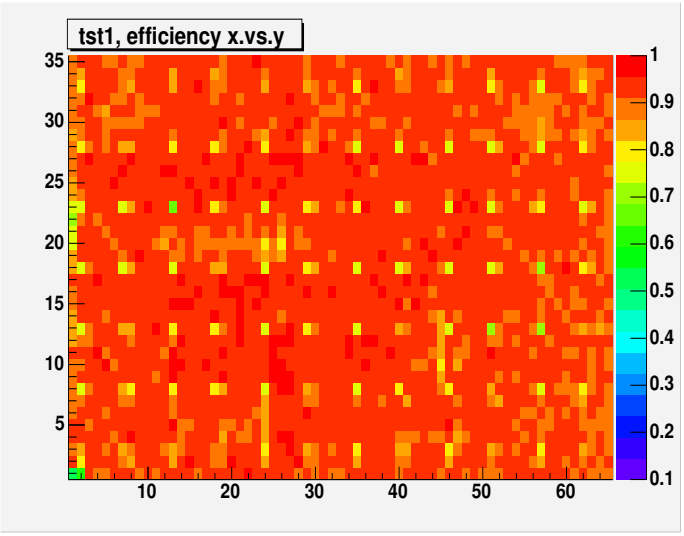

(a)

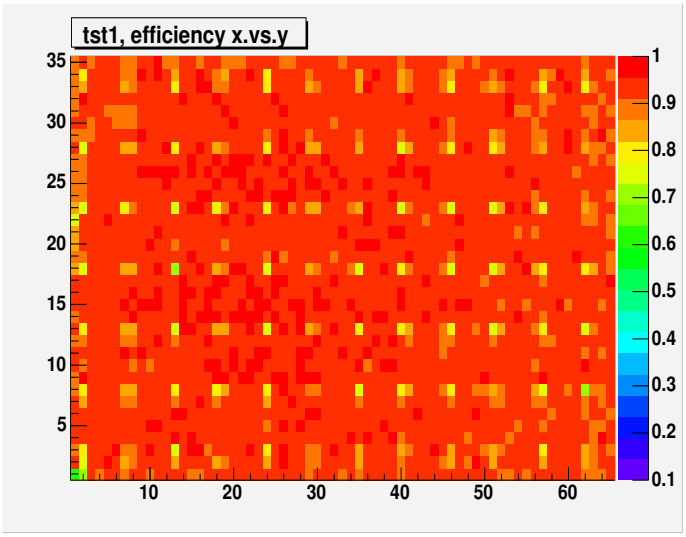

(b)

Figure 4.12: Efficiency map of a half chamber operated at 8100 V (a) and at 8200 V (b).

for the moltiplicaton process to start all over the surface. This can be observed by comparing the efficiency maps at 8200 and 8100 V (Figs. 4.12(a) and 4.12(b)): in many cases, detectors showing non-uniform efficiency at 8100 V recover their full efficiency at 8200 V.

Another possible cause of local efficiency loss is the roughness of the surface (which may also be due to linseed oil dripping from the surface), causing spikes on the surface: these are a source of repeated unwanted discharges in the gap, leading to a localised voltage loss. Such a problem is usually observed together with an increase in the current absorbed by the detector. In this case, raising the high voltage will not help.

A very few detectors have shown major efficiency disuniformities, thus it was possible to apply a strict selection on the uniformity of the efficiency; the selection criteria will be discussed more in detail in Sec. 4.3.5.

4.2.3 Systematic error on the measurement of efficiency

After a few detectors had been tested, it was found that the maximum efficiency reached by the detectors (as measured from the fit to the efficiency curve and seen on the efficiency maps) was systematically lower by about $3 \div 5\%$ than the efficiency measured in the beam tests (see Chapter 3 and Ref. [51]). The hypothesis was made that this may be due to the geometry of the set-up and to the algorithm described in Sec. 4.2.2, namely on the requirement that the impact position on the tested detectors be the same, within some tolerance value, as the expected impact position measured by the tracking system. In a few cases, the reconstruction of the cosmic track may be wrong, because of:

- multiple scattering of the muons off the structures or the test station;
- false coincidences due to more than one muon crossing the set-up simultaneously;
- false coincidences due to noise counts of the tracking chambers.

All these phenomena lead to the reconstruction of false tracks, so that in some fraction of events the tested detectors will be erroneously considered inefficient.

To evaluate such a systematic error, a few runs were re-analysed by calculating the efficiency of one of the two tested detectors only for those events in which the other detector is efficient: this is equivalent to reconstructing the track with three points instead of two, thus cutting drastically all the false tracks. Such a method could not be applied to all the tested detectors, since

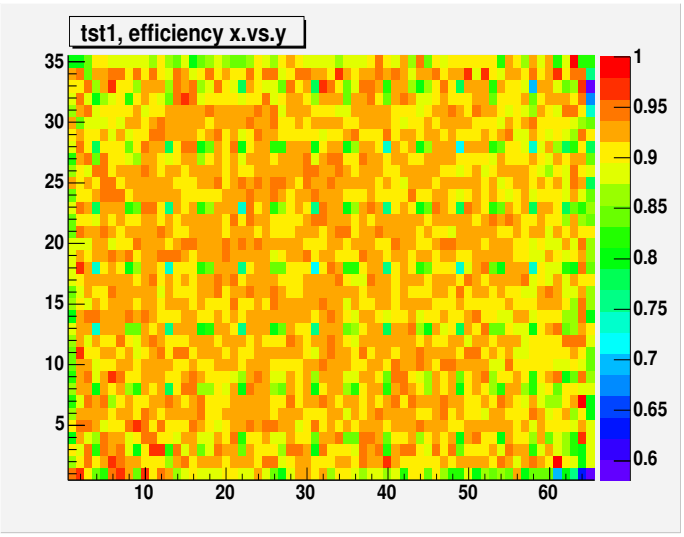

(a)

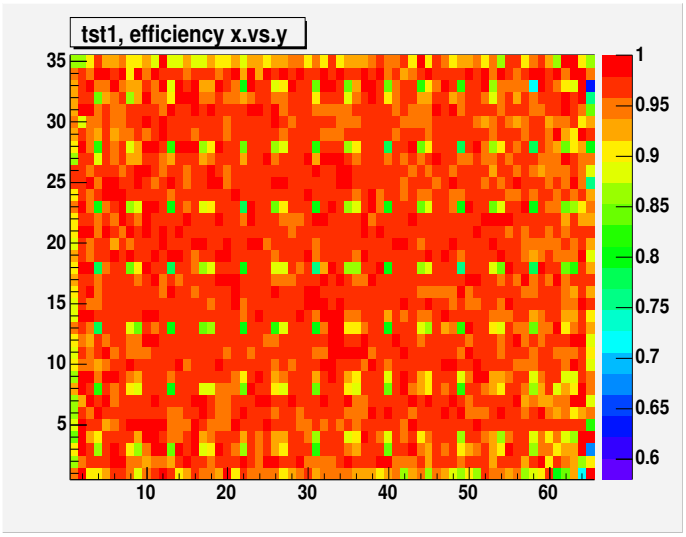

(b)

Figure 4.13: Efficiency map of a half detector operated at 8200 V, measured with the standard method (a) and with the corrected algorithm reported in the text (b).

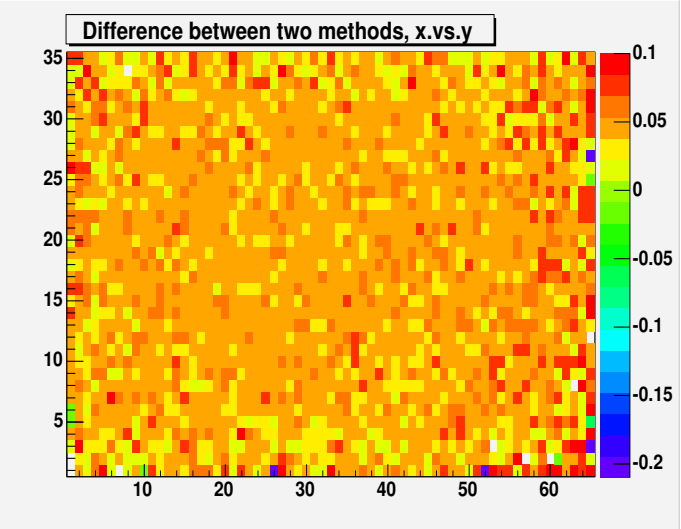

Figure 4.14: Difference cell-by-cell between the two efficiency maps shown in Figs. 4.13(b) and 4.13(a).

for practical reasons not all detectors have been tested together with another one, and since a few testing configurations paired detectors of different sizes, leading to a limited acceptance. The analysis has been performed for a few detectors, and the results found are well represented by the examples presented here. The efficiency maps for the same detector, measured with the usual method described in Sec. 4.2.2 and with the three points requirement, are shown in Figs. 4.13(a) and 4.13(b). The systematic error is clearly visible. In Fig. 4.14, the difference between the two methods is plotted: the systematic error can be evaluated to be about 4%. It is remarkable that such error is evenly spread throughout the surface of the detectors: the fraction of false tracks reconstructed in a cell is roughly the same for all cells. Of course there are fluctuations, but no specific region of the detector is affected by the error. This means that the efficiency maps obtained with the standard method, though affected by an overall systematic error, can still be used to evaluate the uniformity of the detectors, which is the primary goal of such maps.

To evaluate numerically the systematic error, the difference can be plotted on a 1-dimensional histogram. The mean value of the distribution is an estimate of the systematic error. To prevent such mean value from being influenced by very peripheral cells with very few events, each cell has been weighted with the square root of the number of events in the cell. One example of such histogram is reported in Fig. 4.15, while in Tab. 4.2 the results

are shown for all the detectors for which the analysis has been performed.

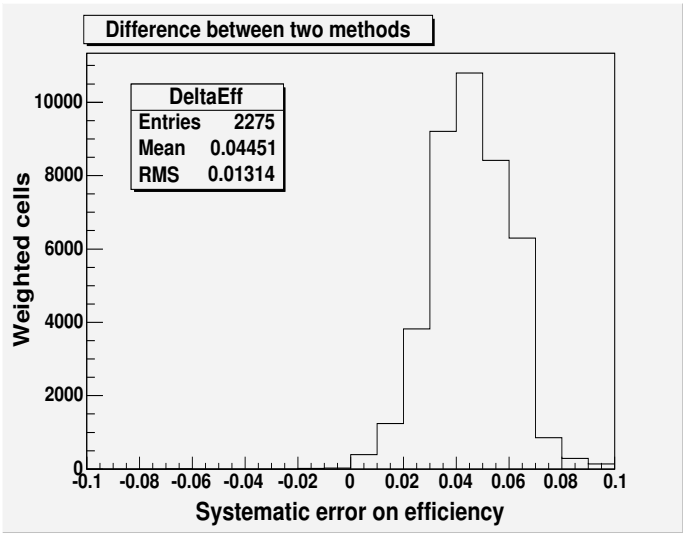

Figure 4.15: Distribution of the difference cell-by-cell between the two efficiency maps shown in Figs. 4.13(b) and 4.13(a). Each cell has been weighted with the square root of the number of events in that cell.

In order to evaluate the effect of the systematic error, the efficiency curves need to be compared as well. In Fig. 4.16 two efficency curves of one same cell of one same detector are shown, calculated with both the standard and the corrected method. It appears that the systematic error does not affect the shape of the curve radically, the main effect being the underestimation by about 3% of the maximum efficiency reached. The effect of the systematics on the four curve parameters mentioned in Sec. 4.2.2 has been analysed, to decide which of the parameters where less affected by the error, thus more suitable to characterise the detectors. The results are well summarised by the examples reported in Figs. 4.17(a) through 4.21(b).

As it was mentioned above, the maximum efficiency (Figs. 4.17(a) and 4.17(b)) is underestimated by a few percent, thus such a parameter has not been used in the characterisation of the detector.

The HV_{50}, HV_{90} and slope parameters give information on the efficiency curve in the cell to which they refer. To be considered uniform throughout its whole surface, a detector should exhibit a small spread of these parameters over the cells in which it has been virtually divided for the analysis. The systematic error affects deeply the determination of the HV at 90% efficiency (Figs. 4.18(a) and 4.18(b)), bringing to the overestimation of the voltage value (by about 100 V) and of the spread of such value over the cells. This

Gas gap	Type	Station/Plane	Half	Mean (%)	RMS (%)
5	S	1/1	Left	4.1	1.4
5	S	1/1	Right	4.4	1.9
89	S	2/1	Left	3.5	1.3
89	S	2/1	Right	3.6	1.5
90	S	1/1	Left	4.3	1.4
90	S	1/1	Right	3.8	1.5
93	S	2/1	Left	3.6	1.3
93	S	2/1	Right	3.7	1.5
100	S	2/1	Left	3.5	1.3
100	S	2/1	Right	3.7	1.6
46	L3	2/1	Left	3.7	1.3
46	L3	2/1	Right	4.4	1.3
52	L3	2/1	Left	3.6	1.3
52	L3	2/1	Right	4.3	1.3

Table 4.2: Mean value and RMS of the difference cell-by cell between raw and corrected efficiency maps, for a few detectors.

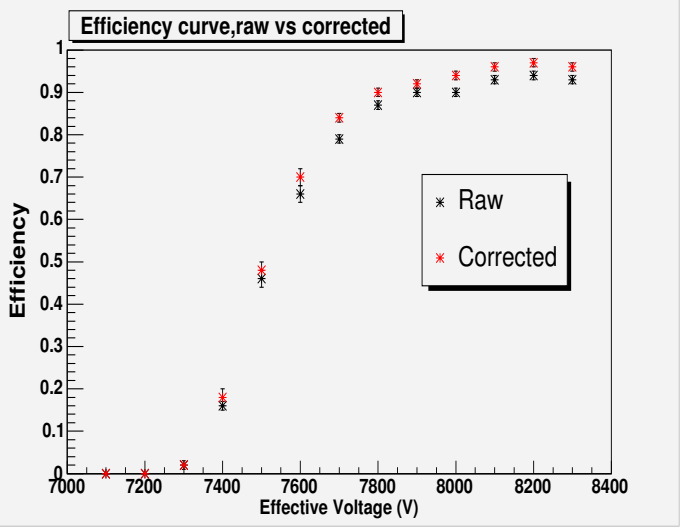

Figure 4.16: Comparison between the efficiency curve of a detector in a 20×20 cm^2 cell calculated with the standard method (raw) and the one corrected for systematics.

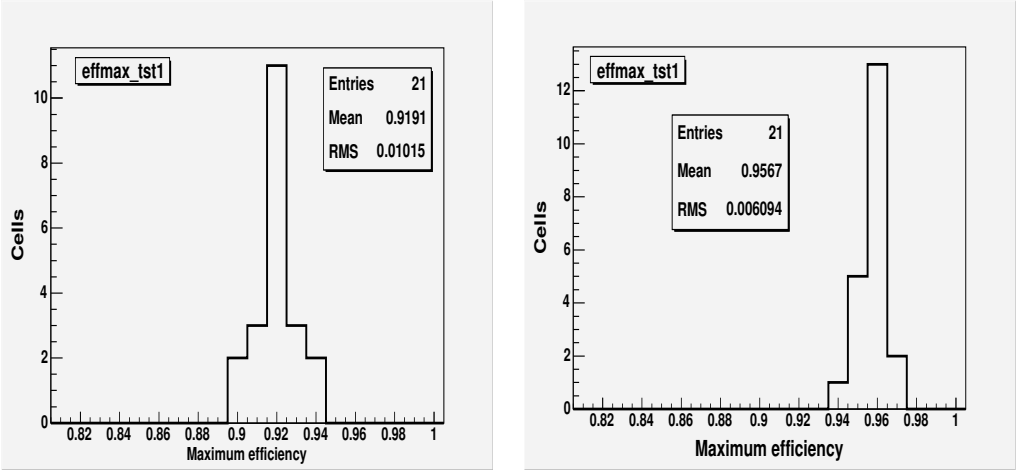

(a) (b)

Figure 4.17: Distributions of the maximum efficiencies over 21 20×20 cm^2 cells of an half detector, measured with the standard method (a) and with the corrected method (b).

does not happen for the voltage at 50% efficiency (Figs. 4.19(a) and 4.19(b)), whose value and relative spread over the cells remain almost unaffected. The reason for this is in the fact that at 50% efficiency the slope of the curve is high, thus a systematic error of about 3-4% on the Y-axis doesn't lead to a significant error on the X-axis (Fig. 4.20(a)). At 90% efficiency the curve is almost flat, thus a small error on the Y-axis may influence significantly the determination of quantities on the X-axis (Fig. 4.20(b)).

The slope parameter is not deeply affected by the systematic error, the shape of the curve being only slightly modified. No significant difference can be appreciated between the standard and the corrected distributions over the cells of the slope (Figs. 4.21(a) and 4.21(b)).

In conclusion, the analysis of the systematic error on the measurement of efficiency and of its consequences on the characterisation of the detectors can be summarised with the following statements:

- the efficiency of the detectors, measured with cosmic rays with the set-up presented here, is underestimated by about 3-4%; this is not a major problem since the aim of the test is to select the best detectors and to evaluate how uniform throughout their surface their performances are: the absolute efficiency of the detectors shall be measured periodically

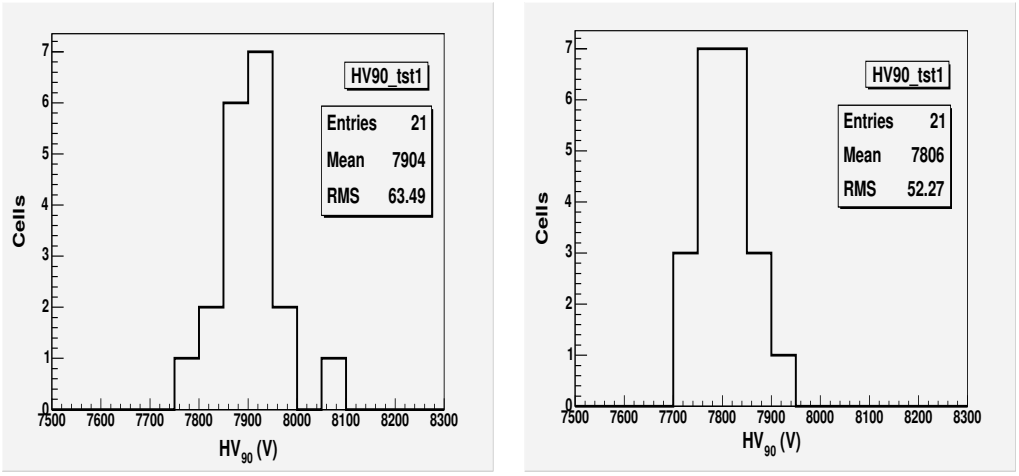

(a) (b)

Figure 4.18: Distributions of the voltage values at 90% efficiency over 21 20×20 cm^2 cells of an half detector, measured with the standard method (a) and with the corrected method (b).

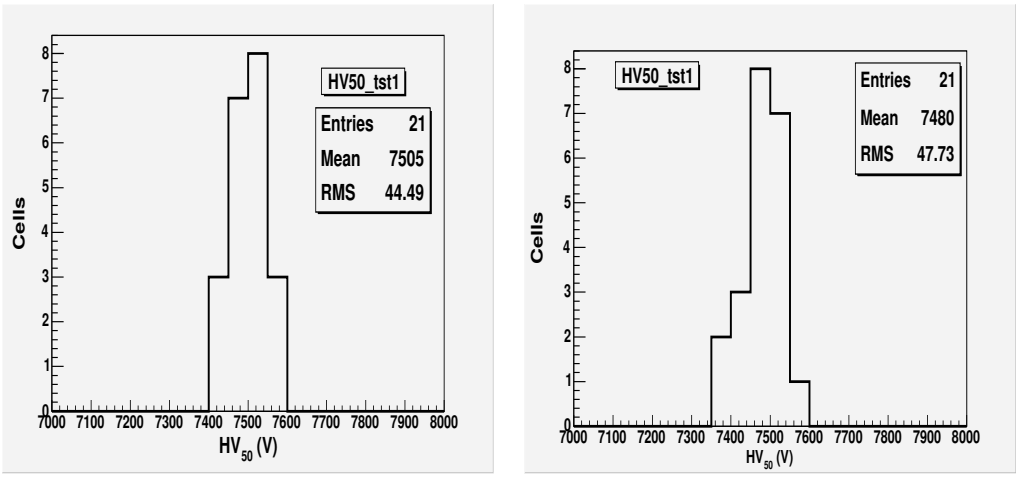

(a) (b)

Figure 4.19: Distributions of the voltage values at 50% efficiency over 21 20×20 cm^2 cells of an half detector, measured with the standard method (a) and with the corrected method (b).

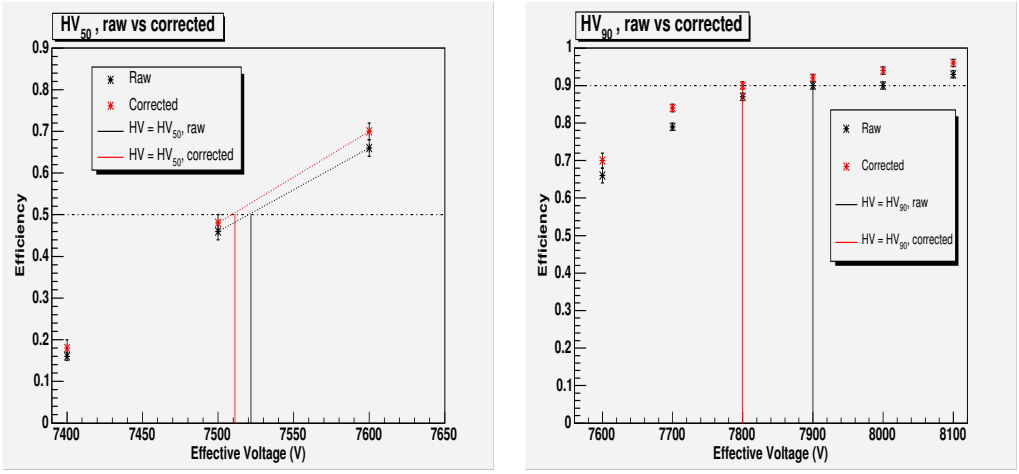

(a) (b)

Figure 4.20: Effect of the systematic error on the determination of the voltage at 50% efficiency (a) and of the voltage at 90% efficiency (b).

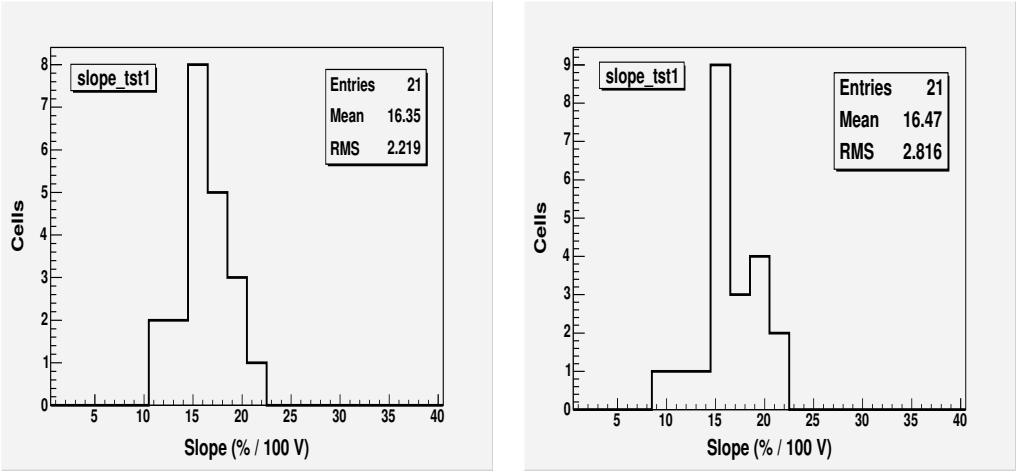

(a) (b)

Figure 4.21: Distributions of the slope of the efficiency curves over 21 20×20 cm^2 cells of an half detector, measured with the standard method (a) and with the corrected method (b).

during data-taking in ALICE;

- the systematic error is evenly spread over the surface of the tested detectors, thus it is still possible to evaluate the uniformity of the detectors and to detect imperfections by looking at the efficiency maps described in Sec. 4.2.2;

- the effect of the systematic error on the efficiency-voltage curve is small, and doesn't affect parameters such as the voltage at 50% efficiency and the slope of the curve, which can still be used to characterise the detectors.

4.2.4 Noise and current measurements

Noise

The noise of the detectors is quantified by the dark counting rate, i.e. the counting rate of the detectors with no beam or irradiation, when the hits are only due to cosmic rays and intrinsic noise.

The counting rate is measured locally with the autotrigger method: the trigger is given by the detector itself, selecting events with at least one hit on both strip planes. The logical scheme of the electronic chain for the autotrigger measurements is shown in Fig. 4.22. The detector surface can be

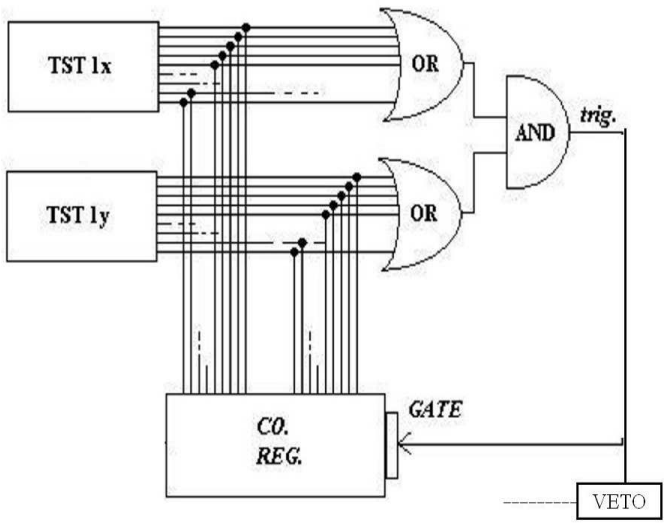

Figure 4.22: Logical scheme of the electronic chain for the autotrigger measurement.

divided in cells defined by the crossing of strips in the two directions. The number of hits N_{ij} in the cell is obtained by counting the number of times that the strips i (in the x direction) and j (in the y direction) have been fired in the same event. The rate R_{ij} (Hz/cm^2) of the cell (i,j) is calculated from N_{ij}:

$$R_{ij} = \frac{N_{ij} N_{non-vetoed}}{\Delta t N_{vetoed} A_{ij}} \tag{4.8}$$

where A_{ij} is the area of the strip crossing, Δt is the acquisition time and the ratio of non-vetoed to vetoed counts over the whole detector accounts for the dead time of the data acquisition system.

Such a method provides the noise map of the detectors (Fig. 4.23(a)), which makes the detection of noisy spots such as those of Fig. 4.23(b) possible. The measurement of the noise map is performed as a function of high voltage, to disentangle genuine detector noise effects from noisy channels in the readout electronics.

The mean noise rate of the whole tested area is simply calculated as

$$R = \frac{N_{non-vetoed}}{A \Delta t} \tag{4.9}$$

where A is the surface of the whole tested area, i.e. approximately a half detector (see Sec. 4.2.2): the mean rate of the whole detector is obtained from the surface-weighted average of the mean noise rates of the left and right halves of the detector. The autotrigger runs have always been performed after the detector had been working for at least one high statistics run, to prevent the results from being influenced by the early stage of operation, when dust or impurities can cause a higher noise.

Dark current

The dark current absorbed by the detector is an important parameter because ageing effects are roughly proportional to the current drawn during long-term operation (see Sec. 3.1.2). The main source of dark current is of course the dark rate, but other effects such as ohmic parasitic currents may be present.

The current has been measured, for each detector, during the high statistics run for measuring the efficiency map. The evolution with time of the current has been monitored during the run, in order to make sure that the measured value be stable.

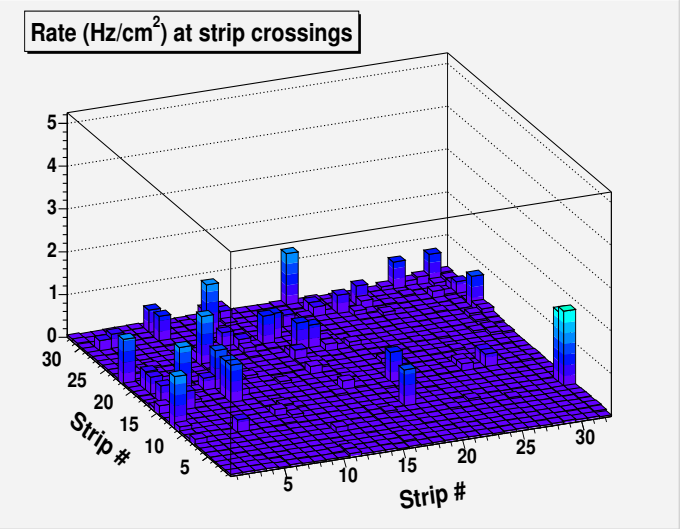

(a)

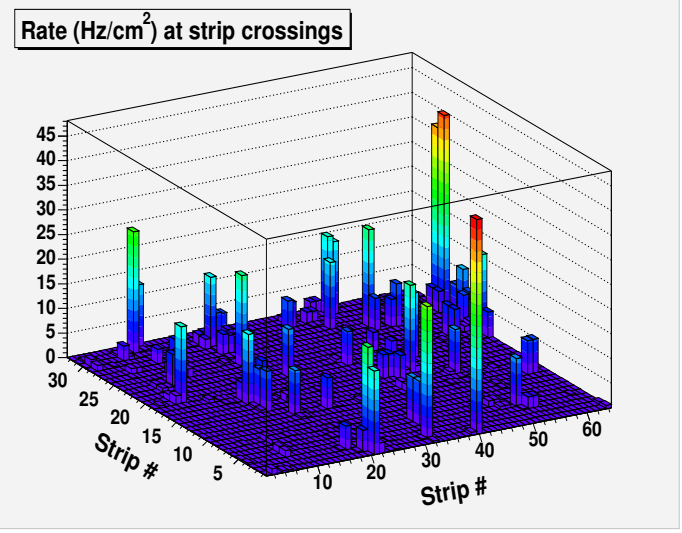

(b)

Figure 4.23: Two examples of noise maps of RPCs operated at 8200 V.

4.3 Results

The results presented here refer to 116 detectors. Though this is a huge set of elements, it has still been possible to analyse and evaluate the results of the test detector by detector, so that each RPC has been characterised and given a quality judgement. The choice of the 72 final detectors (and of the spares) was made on the bases of such judgements. Parallel to such a detector-by-detector procedure, statistical analysis of the results has been carried out for those characteristics that can be represented by numerical values (noise rate, dark current, HV_{50} and so on).

A few detectors (about ten) were discarded during the preliminary tests, mainly due to problems such as gas leaks, broken connectors or short-circuits making it impossible to apply the high voltage to the detectors.

4.3.1 Resistivity

In order to take into account the temperature dependence of the resistivity, the values obtained with the argon method have been rescaled to a reference temperature of 20° C, according to Eq. 4.2. This was possible because the temperature and pressure during the tests were continuosly monitored.

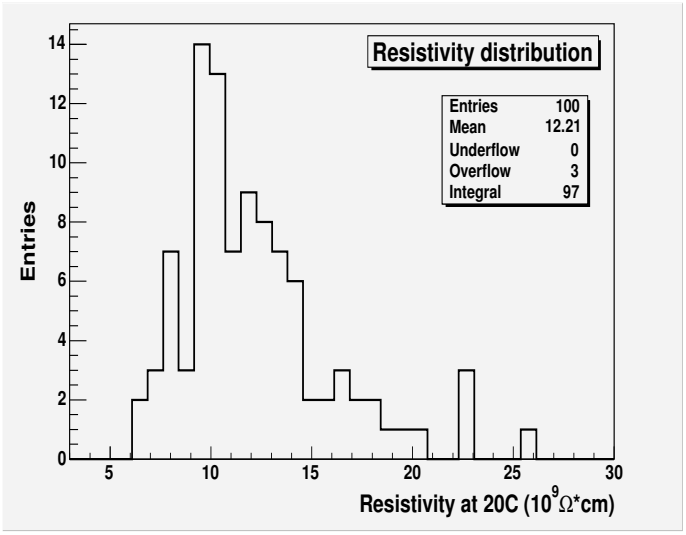

Figure 4.24: Distribution of the resistivity (measured with the argon method and rescaled to 20° C) over 100 tested detectors.

The distribution over 100 detectors of the resistivity measured with the argon method is reported in Fig. 4.24: the peak value of the resistivity is

about 10^{10} Ω cm, the mean value is slightly higher because of the tails of the distribution.

In Fig. 4.25, the distributions are plotted separately for detectors of type C, L and S: it can be noticed that, while the C and S chambers have similar distributions, the distribution of L chambers is shifted towards higher resistivity values. This reflects the choice made in the production stage (see Sec. 4.1.1) to assign lower resistivity electrodes to detector types (C and S) nearest to the beam pipe, i.e. subject to a larger hit rate.

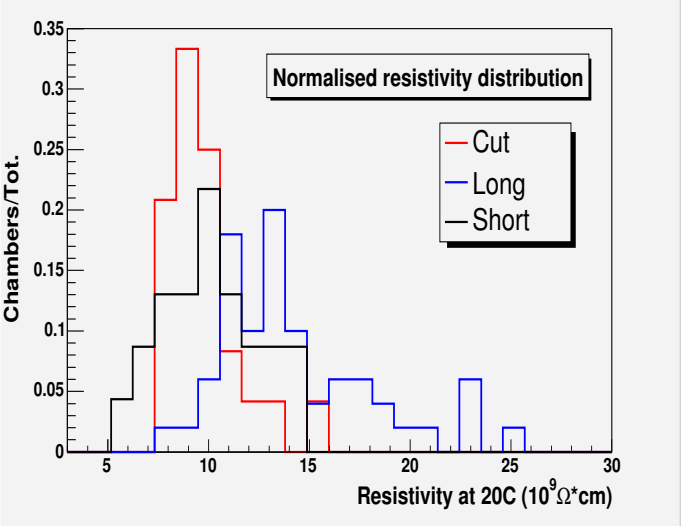

Figure 4.25: Distribution of the resistivity at 20° C measured with the argon method for detectors of type C, L and S. The distributions are normalized to 1.

Figs. 4.24 and 4.25 show higher resistivity values than those that emerged in the R & D stage (see Chapter 3 and Ref. [51]): to understand this, the resistivity value measured for each chamber with the argon method has been plotted versus the mean resistivity of the electrodes with which the same chamber was built, measured as described in Sec. 4.1.1. The plot is shown in Fig. 4.26: it appears that there is an almost linear trend, the resistivity in argon being higher than the mean resistivity of the electrodes by about a factor 3. This may be partially due to alterations of the resistivity during storage and transportation, but such a big discrepancy suggests a systematic error intrinsical to the argon method (e.g. due to the presence on the electrodes of materials such as linseed oil and graphite), or a bias due to the temperature at which the resistivity of the electrodes was measured (no correction has been applied to the measurements performed with the

resistivity meter).

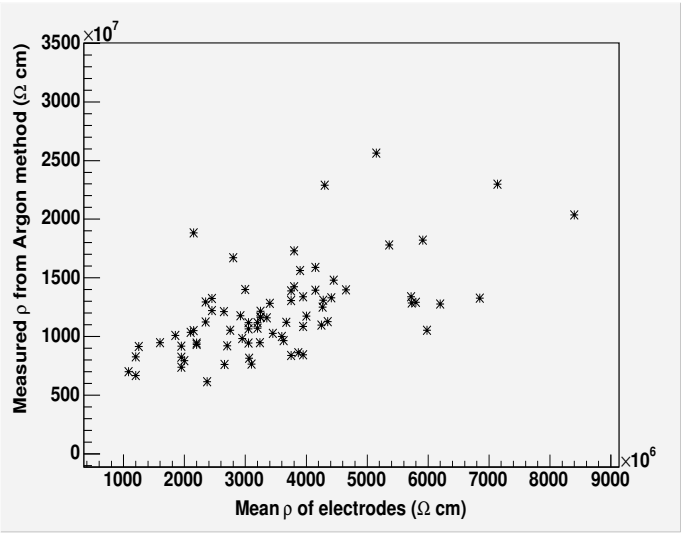

Figure 4.26: Resistivity measured with the argon method and rescaled to 20° C versus mean resistivity of the electrodes measured with the Hewlett-Packard high resistivity meter HP4339B.

4.3.2 Efficiency and uniformity

The efficiency maps and curves have been measured for 106 detectors. The measurements have been carried out with the 72 final readout strip planes and mechanics, so that a few mechanics were tested with more than one gas gap. As it was mentioned in Sec. 4.2.2, in a few cases the efficiency maps showed malfunctions due to imperfections of the readout planes: in such cases, the mechanics were opened and the problem solved.

The efficiency maps of the detectors measured at 8200 and 8100 V were visually inspected, to evaluate the uniformity of the detectors and to mark imperfections and disuniformities. Four classes of behaviours were isolated:

- detectors with uniform, high efficiency throughout the whole surface, such as the one shown in Fig. 4.27 (57% of all produced detectors);

- detectors with a few small (max $\simeq$ 6×6 cm^2) zones with efficiency slightly below 90%, such as the one shown in Fig. 4.28 (17% of all produced detectors);

- detectors with many small zones slightly below 90%, or with a few larger zones slightly below 90%, such as the one shown in Fig. 4.29 (12% of all produced detectors);

- detectors with zones well below 90%, or with large zones slightly below 90%, such as the one shown in Fig. 4.30 (6% of all produced detectors).

The efficiency was not measured for 8% of the detectors, since these have been discarded during the preliminary tests due to construction failures. The above classification does not take into account the very periferal cells of the detector, since, due to the acceptance of the set-up, in those zones the measurement is more deeply affected by both statistical error(small number of events) and systematic error (tracks passing near the edge reconstructed within the active area). Moreover, the cut-off value of 90% for the evaluation of uniformity only refers to the efficiency measured during the test, i.e. affected by the systematic error described in Sec. 4.2.3, the actual efficiency of the detectors being higher by about 4÷5%.

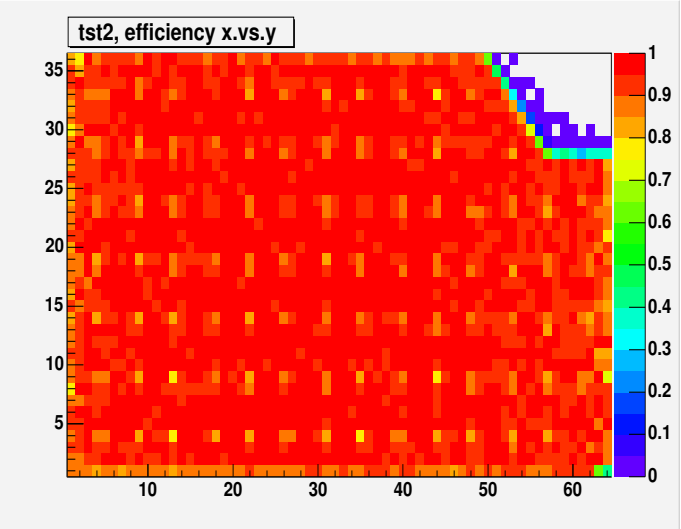

Figure 4.27: Efficiency map of a C-type detector operated at 8200 V, showing high uniform efficiency throughout all the surface. The shape of the top right corner of the map reflects the shape of the detector.

To evaluate numerically the uniformity of the detectors, the HV_{50} and slope parameters have been analysed, since (see Sec. 4.2.3) these are less affected by the systematic errors on the measurement of efficiency. Fig. 4.31(a) shows the distribution of the HV_{50} parameter over all tested detectors.

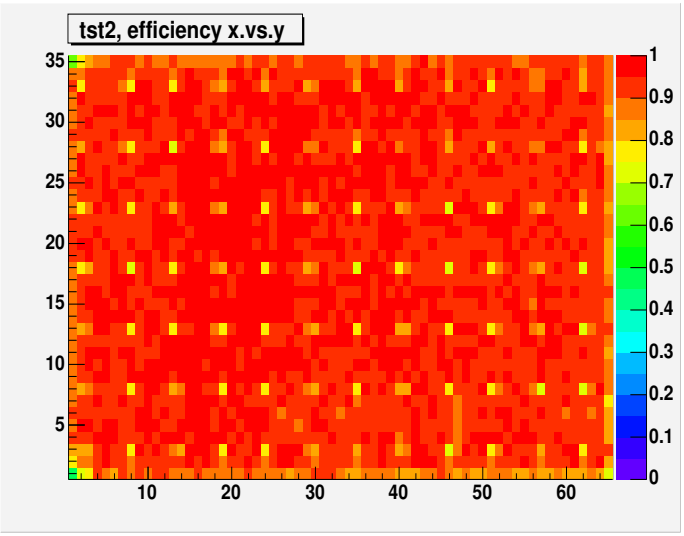

Figure 4.28: Efficiency map of a detector operated at 8200 V, showing small zones slightly below 90%, e.g. the cells with coordinates (28, 5), (26, 6) and (47, 3÷7).

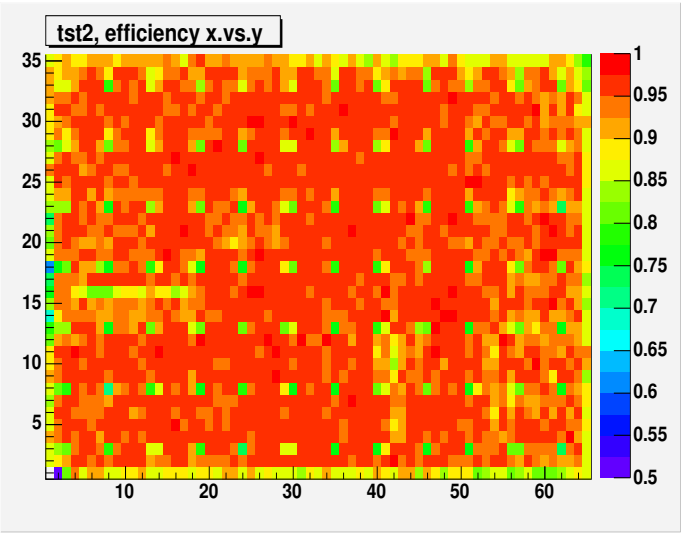

Figure 4.29: Efficiency map of a detector operated at 8200 V, showing a few low efficiency zones.

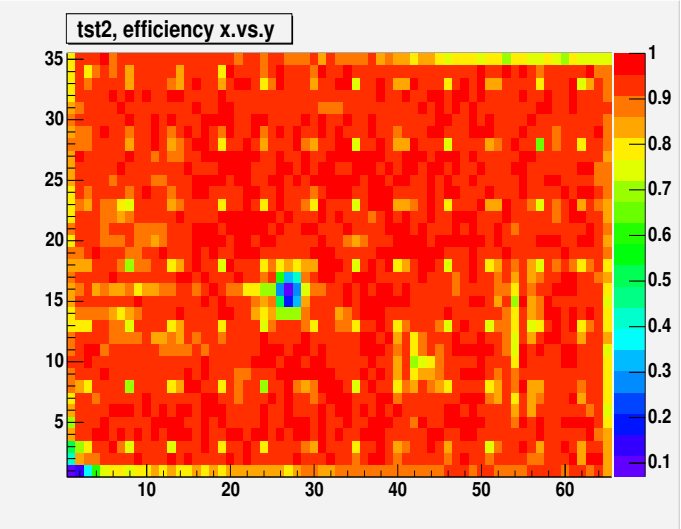

Figure 4.30: Efficiency map of a detector operated at 8200 V, showing several low efficiency zones and one totally inefficient zone.

The value is obtained for each detector by averaging over all the 20×20 cm^2 cells in which it was divided for the analysis. To evaluate the uniformity of each detector, the voltage range in which all 20×20 cm^2 cells of the detector reach 50% efficiency can be used. The distribution of such value over all tested detectors is shown in Fig. 4.31(b).

The distributions show that the detectors reach 50% efficiency around 7500÷7600 V, with a spread among them of the order of 1%. The analysis of Fig. 4.31(b) is more interesting, since it leads to the conclusion that the average spread of the voltage at which different zones of one same detector reach 50% efficiency is about 300 V, i.e. only 4% of the average HV_{50} value. Such results are important since they ensure that the response of each detector to the high voltage is quite uniform throughout its surface.

By looking at the shape of both distributions, a common structure can be spotted: a peak around some typical value plus a tail at higher values, populated by detectors with imperfections.

Concerning the slope of the efficiency curves, it was found that the curves in those 20×20 cm^2 cells containing imperfections have a smaller slope (since different regions of the same cell reach their maximum efficiency at different voltages), while the slope is steeper for regions with uniform efficiency. An example of such a behaviour is shown in Figs. 4.32(a) through 4.33(b).

The distribution of the mean slope over all tested detectors is plotted in Fig. 4.3.2. It is peaked around 0.17 V^{-1}, i.e. most detectors go from 30%

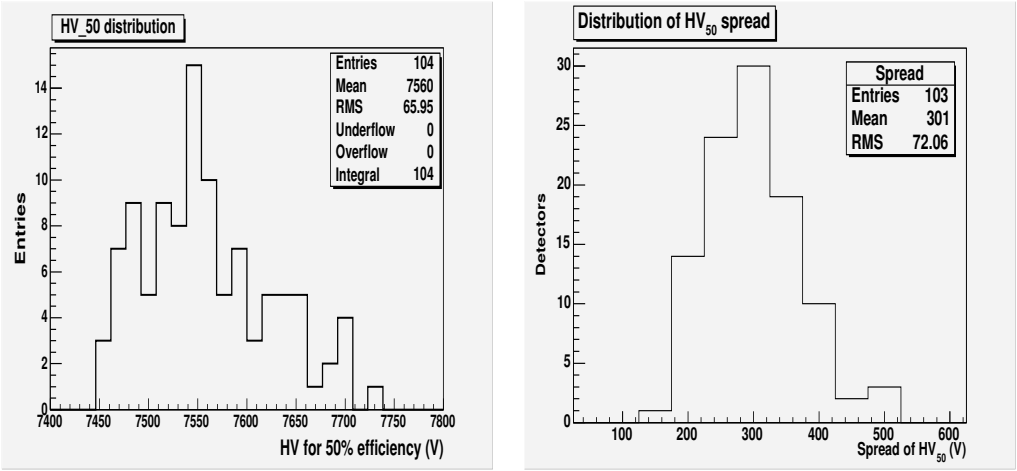

(a) (b)

Figure 4.31: (a) Distribution of the mean HV at 50% efficiency over all tested detectors (b) Distribution over all tested detectors of the voltage range in which all 20×20 cm^2 cells of the detector reach 50% efficiency.

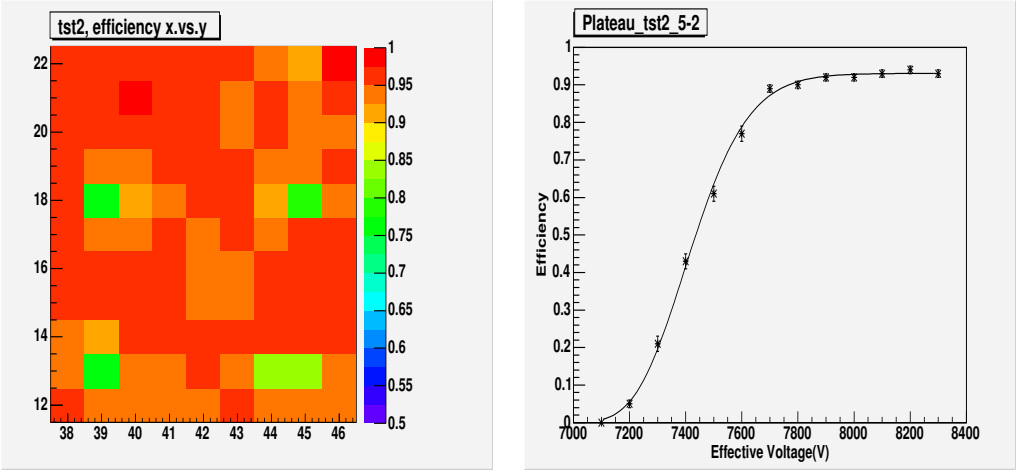

(a) (b)

Figure 4.32: (a) Efficiency map at 8200 V of a 20×20 cm^2 region of a RPC, showing good uniformity: the only inefficient spots correspond to the spacers (see Sec. 4.2.2)(b) Efficiency curve corresponding to the same region.

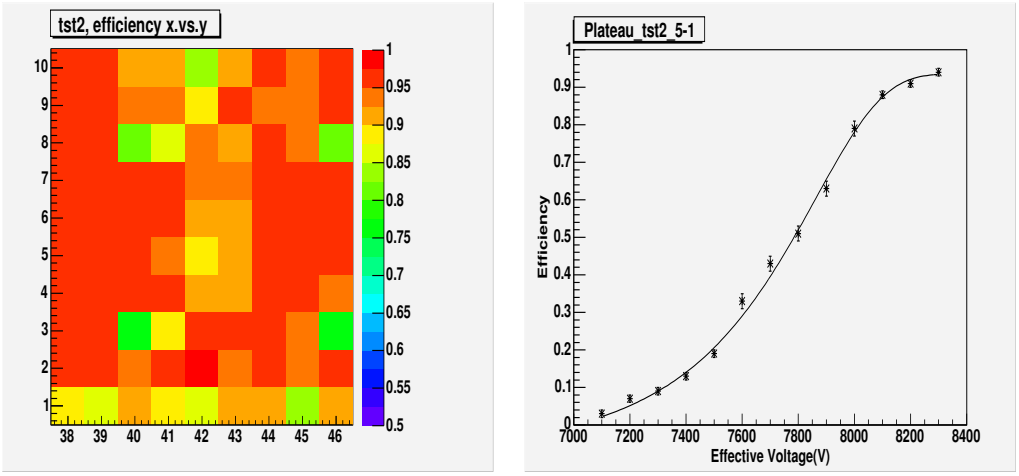

(a) (b)

Figure 4.33: (a) Efficiency map at 8200 V of a 20×20 cm^2 region of a RPC, showing non-uniform efficiency (b) Efficiency curve corresponding to the same region.

efficiency to 80% efficiency in about 300 V.

4.3.3 Current and noise rate

The characterisation of the performances of RPCs requires a parallel evaluation of the efficiency on one hand and of the noise and current on the other hand. This is due to the fact that all of these parameters increase with high voltage: a detector is fully efficient when it is possible to choose such a voltage that the efficiency is maximum throughout the whole surface and the noise and current do not exceed reasonable limits. This is why a few detectors, though showing good, uniform efficiency at 8200 V, have been discarded due to high current and noise rate. For the same reason, detector showing not perfect efficiency maps but very low current and noise rate have not been discarded, since it will be possible to recover the uniformity of efficiency by raising the voltage, without effect on the noise or ageing of the detector.

The typical current and noise working values of the detectors were not exactly known before the tests: they were determined from the statistical analysis of the population of tested detectors. The distribution of the dark current at 8200 V is shown in Fig. 4.35. The current drawn is proportional to

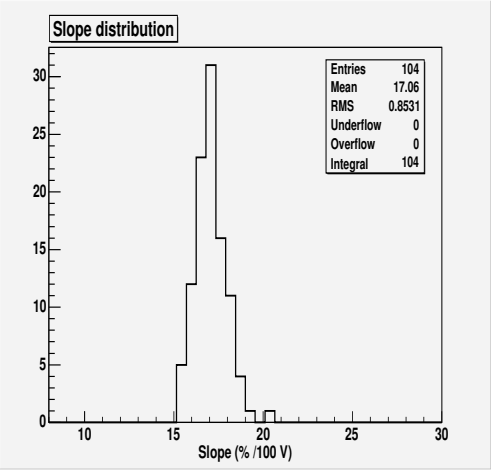

Figure 4.34: Distribution of the slope of the efficiency curve over all tested detectors.

the surface of the detector, so the measured current has been divided by the surface in order to be able to compare detectors of different areas. The peak value is about 0.10÷0.15 nA/cm^2 (i.e. about 2 μA for the biggest detectors), though the mean value is influenced by the tail of the distribution.

The distribution has also been plotted separately for detectors of the three types (Fig. 4.36), to evaluate any effect due to area, shape or resistivity of the detectors: no significant difference can be noticed between the three distributions.

The distribution of the noise rate (Fig. 4.37) has a very similar shape as the one of the current and, to a lesser extent, as the one of HV_{50}: again, there is a peak gathering most detectors and a tail where the problematic ones lie. The peak value of the noise rate is 0.1 Hz/cm^2. The distributions per type (Fig. 4.38) do not show differences between C, L and S-type detectors. In particular, the C and S detectors do no show a higher noise rate than the L ones, which have higher resistivities: this is important since, in principle, a smaller electrode resistivity might result in noisier detectors, due to the diminished discharge-quenching properties of the electrode itself. This topic will be addressed more in detail in Sec. 4.3.7.

As it was shown in Sec. 4.2.4, the measurement of the noise has been performed locally, in order to monitor not only the mean hit rate, but also the quantity and intensity of hot spots. Three intensity classes of hot spots have been defined: those with rate between 5 and 10 Hz/cm^2, those with rate between 10 and 20 Hz/cm^2 and those with rate higher than 20 Hz/cm^2. For

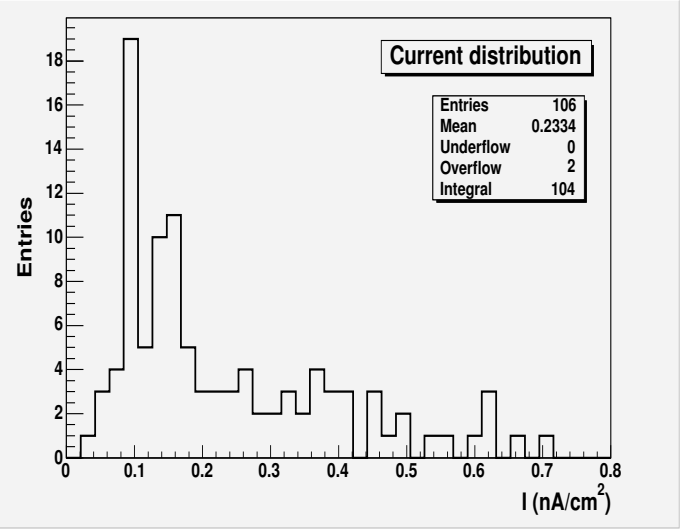

Figure 4.35: Distribution of the dark current absorbed at 8200 V over all tested detectors.

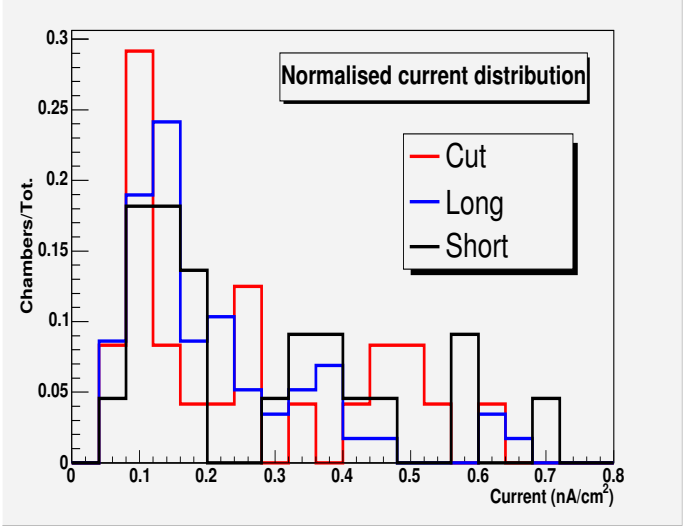

Figure 4.36: Distribution of the dark current absorbed at 8200 V for detectors of type C, L and S. The distributions are normalised to 1.

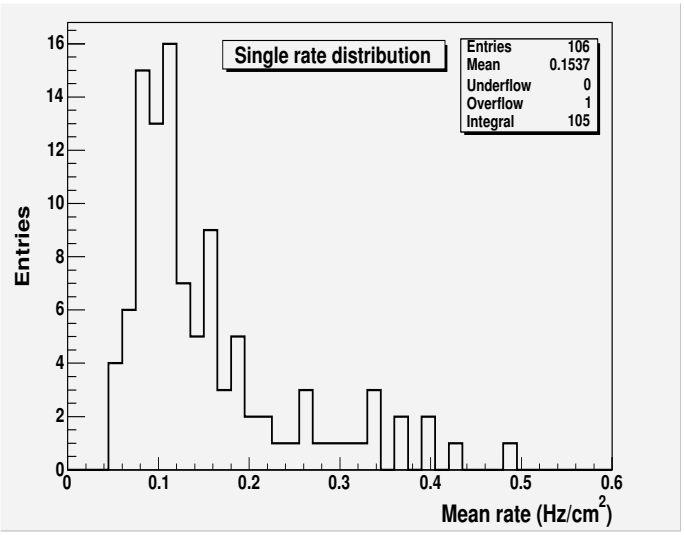

Figure 4.37: Distribution of the mean noise rate at 8200 V over all tested detectors.

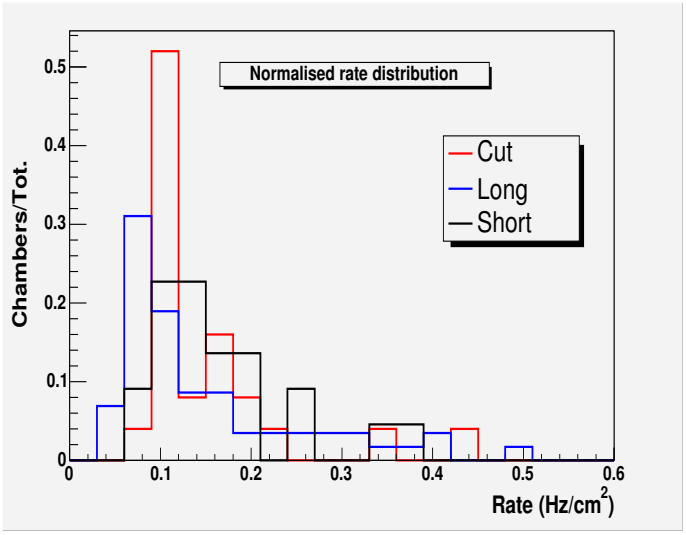

Figure 4.38: Distribution of the mean noise rate at 8200 V for detectors of type C, L and S. The distributions are normalised to 1.

each detector, the noise maps have been visually inspected and the number of hot spots in each class has been counted. The distribution over all detectors of the number of hot spots for each class is shown in Fig. 4.39. The number of hot spots is quite low, on average 6 for the first class, 3 for the second class and 2 for the third class. While a certain number of hot spots of the first two classes is physiological for RPCs, the number of hot spots of the third class should be as low as possible, since they may cause local inefficiencies due to continuous discharges, and/or speed up the ageing of the detector.

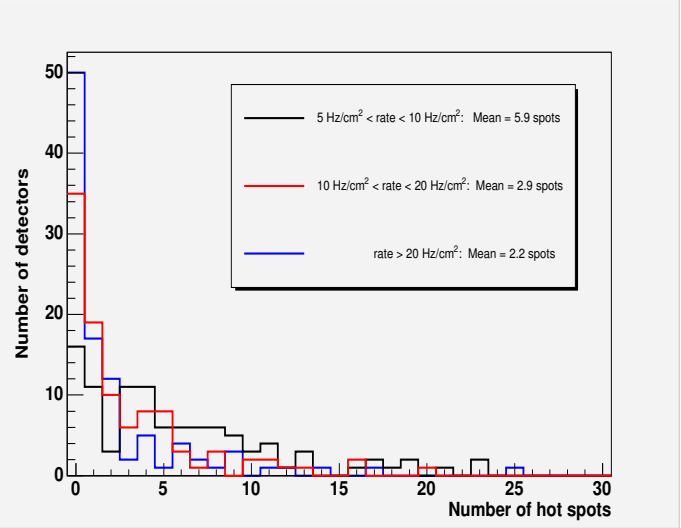

Figure 4.39: Distribution over all tested detectors of the number of hot spots, for three different intensity classes.

4.3.4 Working voltages

As explained above, the choice of the working voltage must be a compromise between efficiency, noise and current. The analysis of such elements allowed to assign an indicative working voltage to each detector:

- 7% of the detectors showed uniform efficiency at 8100 V;
- 72% of the detectors showed uniform efficiency at 8200 V;
- 21% of the detectors showed not fully uniform efficiency at 8200 V, but current and noise rate values low enough to allow operation at higher voltages.

The statistics reported here do not include those detectors that were discarded. It has to be pointed out that such results are not final, since the current, noise and (possibly) efficiency of the final detectors will be monitored again during the commissioning and first data-taking phases.

4.3.5 Selection criteria

After collecting a vast amount of data and characterising all detectors, criteria have been defined to select the final detectors and the spares. Since there are many elements to take into account when evaluating the performances of a RPC, it is not straightforward to define precise quantitative criteria for the selection or rejection of detectors. The following strategy has been adopted: the detectors have been evaluated one-by-one on the bases of efficiency, uniformity, noise rate, number of hot spots and absorbed current; every detector has been rated with a mark (0 to 4) that summarises the quality of its performance.

- detectors which have been discarded during the preliminary tests because of serious construction flaws have been rated 0;
- detectors with inefficient regions or very high absorbed current and noise rate have been rated 1;
- detectors with a few low-efficiency regions and/or medium to high noise rate and absorbed current have been rated 2;
- detectors with small efficiency imperfections and/or medium noise rate and current have been rated 3;
- detectors with uniform, high efficiency and low to medium noise rate and absorbed current have been rated 4.

A few detectors, showing very small efficiency imperfections and very low noise rate and current, have been rated 4 because it will be possible to recover the full efficiency by raising the voltage.

As it will be shown further in this section, detectors with a mark from 2 to 4 have been selected for use in ALICE: to characterise quantitatively the performances of the detectors in the three classes, four quantities have been considered:

- the mean noise rate at 8200 V;
- the number of hot spots with rate higher than 20 Hz/cm^2 at 8200 V;

- the dark current at 8200 V;
- the voltage range in which the efficiency curves of all the 20×20 cm^2 cells in which the detectors have been virtually divided reach 50% efficiency.

The distribution of such values for the detectors rated 2, 3 and 4 is shown in Figs. 4.40 through 4.43.

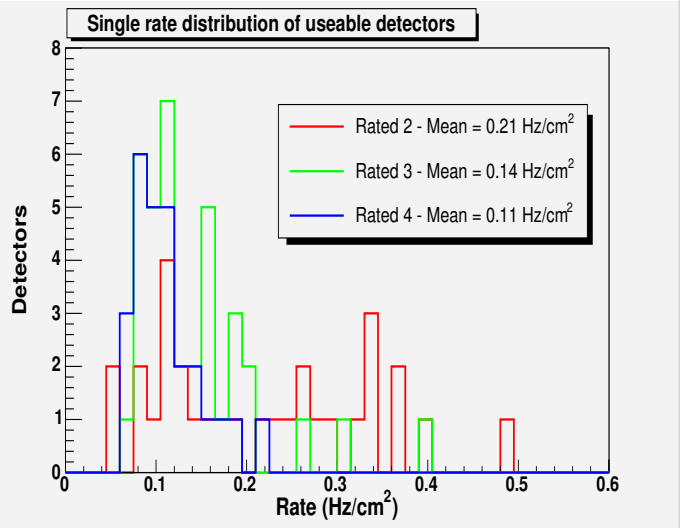

Figure 4.40: Distribution of the mean noise rate at 8200 V for detectors rated 2, 3 and 4.

The results of such analysis are summarised in Tab. 4.3, in which the mean and maximum values of the above parameters are reported for the three classes of detectors.

The classification of all tested detectors according to their rating is shown in Fig. 4.44. Figs. 4.45(a) and 4.45(b) show the classification separately for the two stations MT1 and MT2 and for all detector types.

According to the results presented so far, but also to the requirements shown in Tab. 4.1, the following selection criteria have been adopted:

- detectors rated 0 (8%) or 1 (9%) have been discarded;
- detectors rated 2 (26%) have been selected for use in ALICE only for the L tipology (with one exception);
- detectors rated 3 (33%) or 4 (24%) have been selected for use in ALICE.

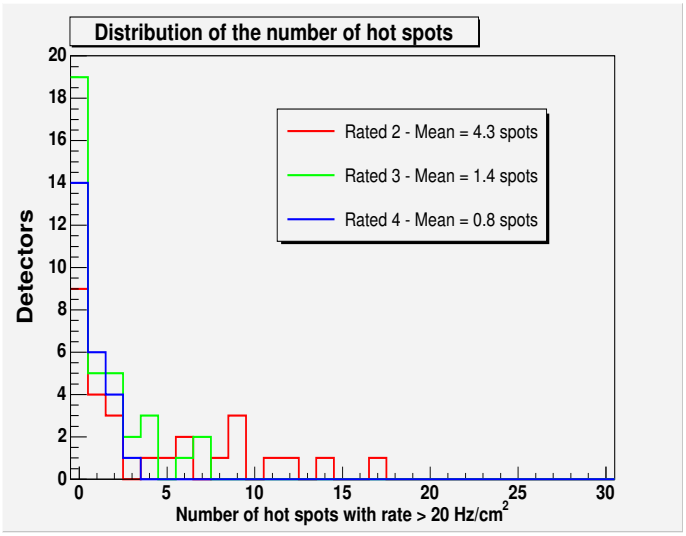

Figure 4.41: Distribution of the number of hot spots with rate higher than 20 Hz/cm^2 at 8200 V for detectors rated 2, 3 and 4.

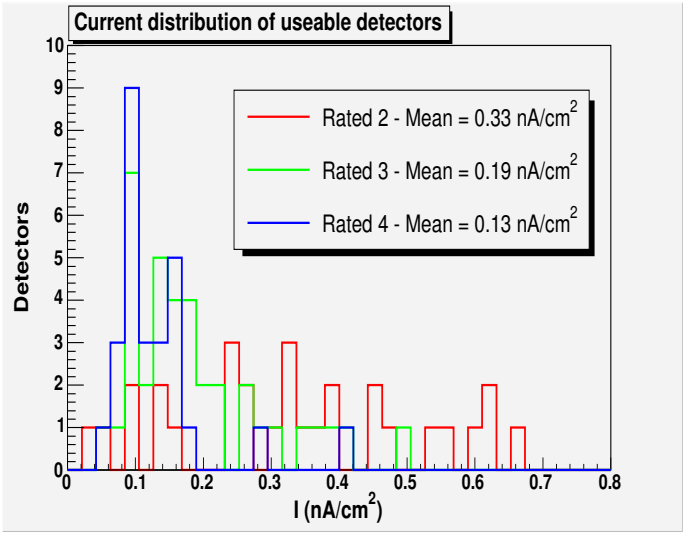

Figure 4.42: Distribution of the dark current absorbed per unit surface at 8200 V for detectors rated 2, 3 and 4.

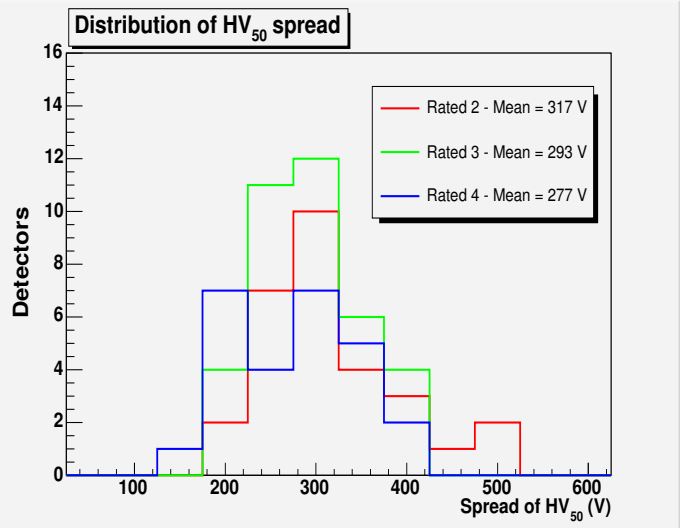

Figure 4.43: Distribution of the voltage range in which all regions of the same detector reach 50% efficiency, for detectors rated 2, 3 and 4.

Parameter	Rated 4	Rated 3	Rated 2
Mean noise rate (Hz/cm^2)	0.11	0.14	0.21
Max noise rate (Hz/cm^2)	0.22	0.40	0.49
Mean # of hot spots	0.7	1.4	4.3
Max # of hot spots	4	7	17
Mean absorbed current (nA/cm^2)	0.13	0.19	0.33
Max absorbed current (nA/cm^2)	0.41	0.50	0.86
Mean spread of HV_{50} (V)	277	293	317
Max spread of HV_{50} (V)	400	400	500

Table 4.3: Mean and maximum values for the four quality parameters, for detectors rated 2, 3 and 4.

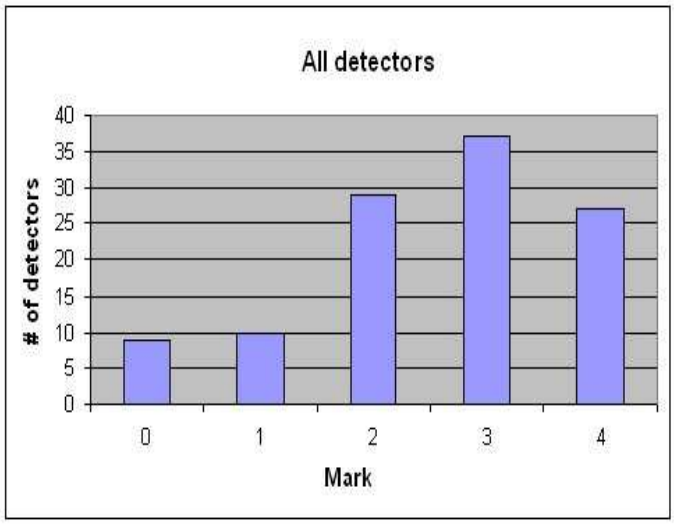

Figure 4.44: Classification of all tested detectors according to the rating of their performances.

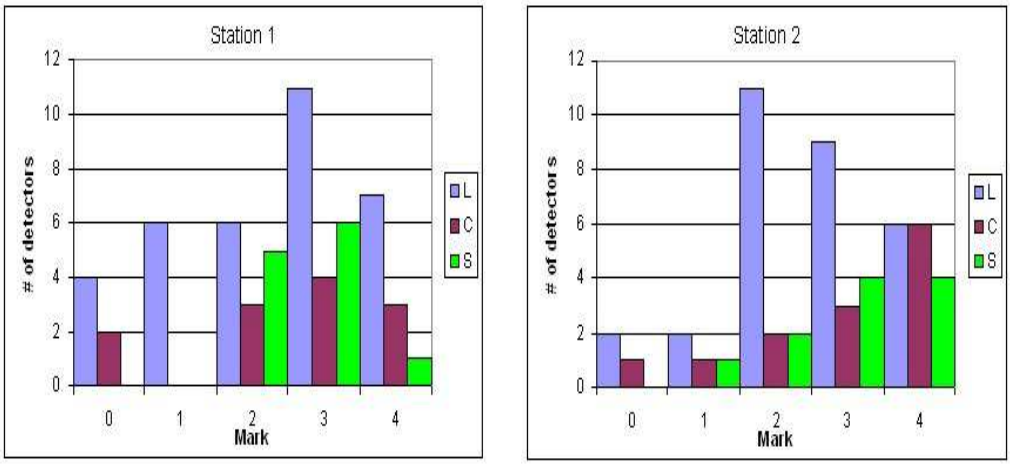

(a) (b)

Figure 4.45: Classification of the tested detectors of C, L and S-types according to the rating of their performances, for station MT1 (a) and MT2 (b).

Tab. 4.4 shows the present situation: the 72 detectors to be used in ALICE have been chosen according to the above criteria. A number of detectors have been selected as spares, but for the C and L types such a number is not sufficient yet (Tab. 4.5): this prompted the decision to start a new production and testing session, to match the established number of spares. Tab. 4.4 also shows that, in one case, a C-type detector which was rated 2 was selected for use in ALICE, due to the lack of detectors of that type with a higher mark. Should such detector exhibit insufficient performances during operation, it will be substituted with one of the spares selected during the forthcoming production and testing session.

Type	Required in ALICE	Rated 4	Rated 3	Rated 2
C	16	8	7	1
L	48	13	20	15
S	8	3	5	0
Total	72	24	32	16

Table 4.4: Classification of the detectors selected for use in ALICE according to the rating of their performances.

Type	Station	Required spares	Rated 4	Rated 3	Rated 2
C	MT1	4	0	0	1
C	MT2	4	1	0	2
L	MT1	6	0	0	0
L	MT2	6	0	0	2
S	MT1	4	0	3	3
S	MT2	4	2	2	2

Table 4.5: Classification of the detectors selected as spares in ALICE according to the rating of their performances.

4.3.6 Conclusions and status

After extensive tests, all the producted detectors have been fully characterised; the results of the tests have been stored in a database (Fig. 4.46) that will be made available for reference to the collaboration.

Concerning the quality of the production, the results shown in the previous section can be summarised as follows:

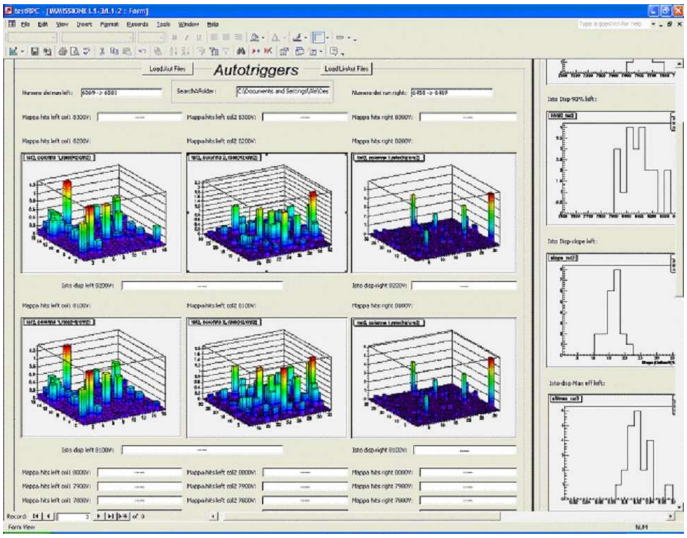

Figure 4.46: A glimpse of the database in which all data concerning the RPCs for the ALICE muon trigger have been stored.

- 17% of the produced detectors have been discarded because of major failures or unsatisfactory performances;
- 26% of the produced detectors have shown sufficient performances, allowing them to be used in peripheral regions of the trigger stations or as spares;
- 57% of the produced detectors have shown good or excellent performances. For a quantitative estimation of such performances, the reader should refer to Tab. 4.3;
- the 72 final RPCs for the ALICE Muon Trigger have been selected and characterised. They have been among the first detectors to be installed in the ALICE cavern[66].

4.3.7 Correlations: rate, current and resistivity

Further studies have been carried out to investigate the reciprocal dependence of parameters such as the resistivity of the electrodes, the noise rate of the detectors and the absorbed current. Since the current flowing through the electrodes, if there are no ohmic leaks, is mainly due to the discharges of electrons in the gas gap due to the RPC counts, one should expect a positive correlation between the dark absorbed current and the mean dark rate of

the detector. Such correlation is also suggested by Figs. 4.35 and 4.37: the distribution of the mean dark rate at 8200 V and that of the dark current at 8200 V have similar shapes.

Such effect can be better appreciated by plotting the two parameters in a 2-D histogram (Fig. 4.47). The histogram refers to 62 detectors, the ones for which a measurement of the current performed during the autotrigger run (in which the noise was measured) is available. The correlation coefficient between the two data sets is 0.40: such value exceeds the critical value of 0.325 for a 1% confidence level with 62-2 = 60 DF: the statistical analysis on the ALICE RPCs confirms the expected correlation between the dark rate and the dark current.

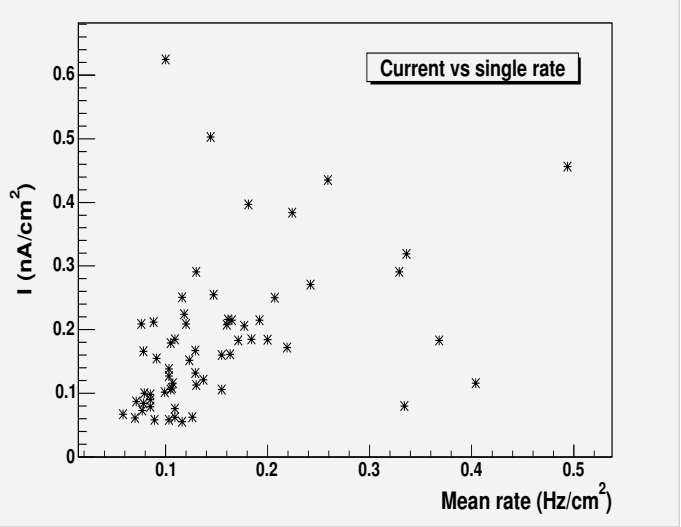

Figure 4.47: Mean dark rate at 8200 V versus current absorbed, measured during the same autrotrigger run in which the dark rate was measured, for 62 detectors.

The influence of resistivity on noise rate and current has also been investigated. In Fig. 4.48 the current absorbed at 8200 V is plotted versus the resistivity of the electrodes measured with the argon method, for 100 detectors: there appears to be no evident correlation. This is confirmed by statistical analysis: the correlation coefficient is 0.12, well below the critical value (0.164 with 100-2 = 98 DF), even for a confidence level of 10%. Such a result suggests that the ohmic component in the current drawn by the detectors during operation is negligible, the current being only due to the counts of the detector.

In Fig. 4.49 the dark rate at 8200 V is plotted versus the resistivity of the

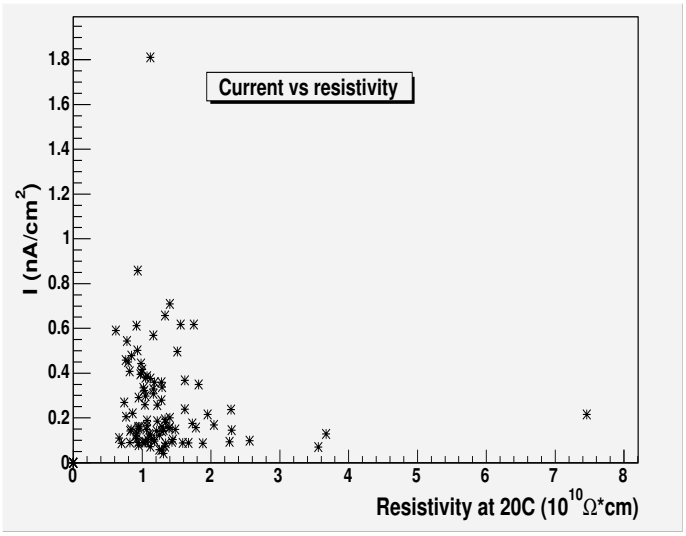

Figure 4.48: Dark current absorbed at 8200 V versus resistivity of the electrodes measured with the argon method, for 100 detectors.

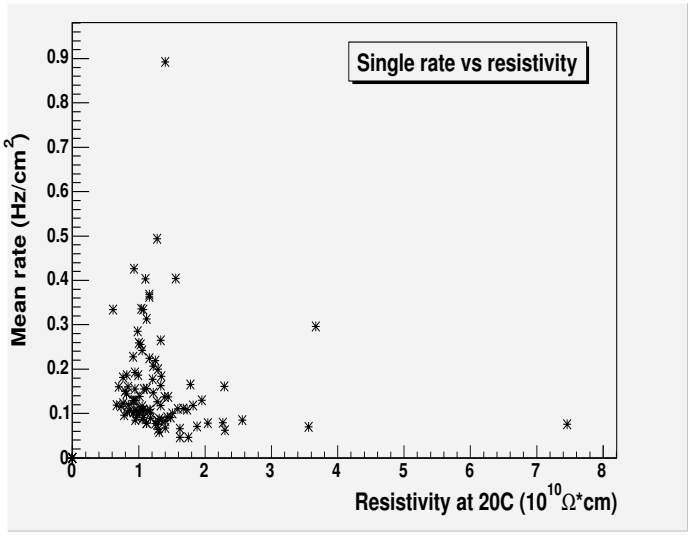

Figure 4.49: Dark rate at 8200 V versus resistivity of the electrodes measured with the argon method, for 100 detectors.

electrodes measured with the argon method, for 100 detectors: once again, no evident correlation can be detected and the correlation coefficient (0.11) is below the critical value, even for a 10% confidence level. Such result is interesting, since it shows that the choice of low resistivity electrodes does not enhance the noise of the detector, which is only influenced by the quality of the electrodes surface.

Chapter 5

Performances of aged RPCs

In Sec. 3.2.3, the results of extensive ageing tests[54, 56, 57] on the RPCs for the ALICE muon trigger have been summarised. Three detectors among those tested for ageing have later been tested in Torino with the test station described in Chap. 4, in order to detect possible alterations due to the long term operation: in particular, the possibility to obtain high granularity efficiency maps was exploited.

The detectors considered are:

- RPC1: a pre-production full-size RPC which was tested at GIF, with the final streamer mixture with 1% SF_6;
- RAV3 and RAV4: two 50×50 cm^2 prototypes which were tested at GIF, with the final avalanche mixture with 0.3% SF_6;

5.1 Ageing in streamer: RPC1

The RPC1 detector was tested for ageing at the Gamma Irradiation Facility. The set-up for the test and the behaviour of dark rate, dark current and efficiency as a function of the integrated hits are shown in Figs. 3.9 and 3.10, respectively. During that test, Pb filters where placed in front of RPC1, so that different regions of the detector were differently irradiated. The location of the filters with respect to the detector surface is shown in Fig. 5.1. Thinner filters were placed in front of the detector region which will be located nearer to the beam, in order to obtain an ALICE-like rate distribution. The resulting rate on the detector ranges from 6 to 60 Hz/cm^2, i.e. one order of magnitude larger than expected in ALICE in Pb-Pb collisions. The efficiency was measured with a cosmic ray telescope, in the most irradiated part of the detector. The efficiency plateau as measured with source-on at

the beginning of the ageing test and after about 100 Mhit/cm^2 is shown in Fig. 5.2(a). Ageing appears to cause a displacement of the curve towards higher HV values, and a less steep slope: a possible explanation may be a progressive increase of the bakelite resistivity, resulting in a decreased rate capability under irradiation. The lower slope can be explained with the different irradiation on different regions of the detector, causing some spread in the values at which full efficiency is reached.

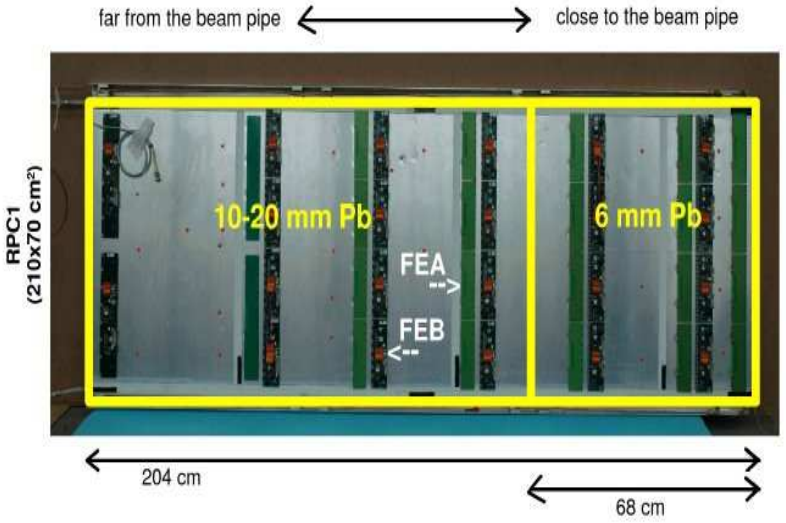

Figure 5.1: The RPC1 detector during the ageing test at GIF. Regions corresponding to different lead shieldings and the corresponding position with respect to the LHC beam pipe are also shown.

About one year after the end of the ageing test, the detector has been tested in Torino with cosmic rays. Only the rightmost half of the detector in Fig. 5.1 has been tested, so that the efficiency measurement roughly refers to the same region as the GIF measurement. The efficiency curve (Fig. 5.2(b)) is shifted back towards lower HV values, and the original slope is restored, as expected for a source-off measurement. A comparison between the values of efficiency reached is of course difficult, since the efficiency has been measured in very different conditions: in particular, the measurement with cosmic rays is affected by the systematic error discussed in Sec. 4.2.3.

The efficiency curve has also been measured locally, in cells 17×23 cm^2 large. The spread of the HV_{50} parameter defined in Chap. 4 is shown in Fig. 5.3: all cells reach 50% efficiency in a 200 V range: this value represents a 3% spread, and is in line with the values obtained with new RPCs and reported in Sec. 4.3.2.

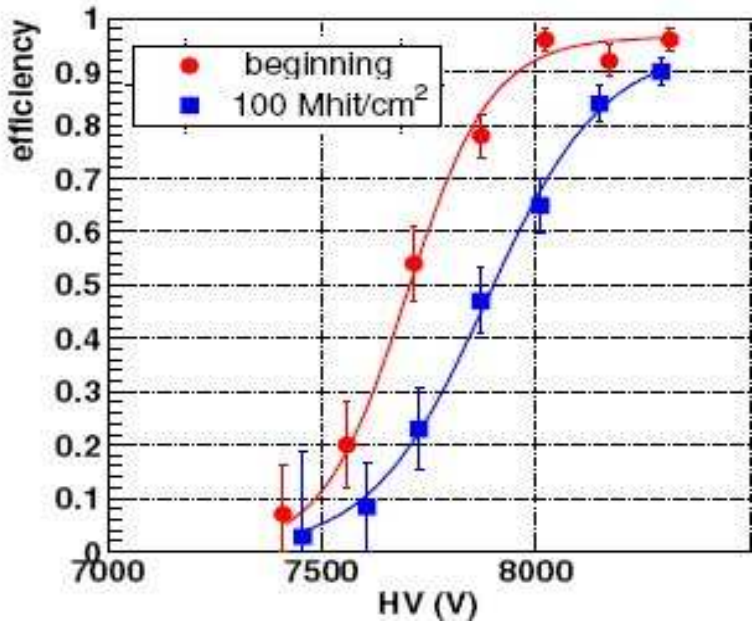

(a)

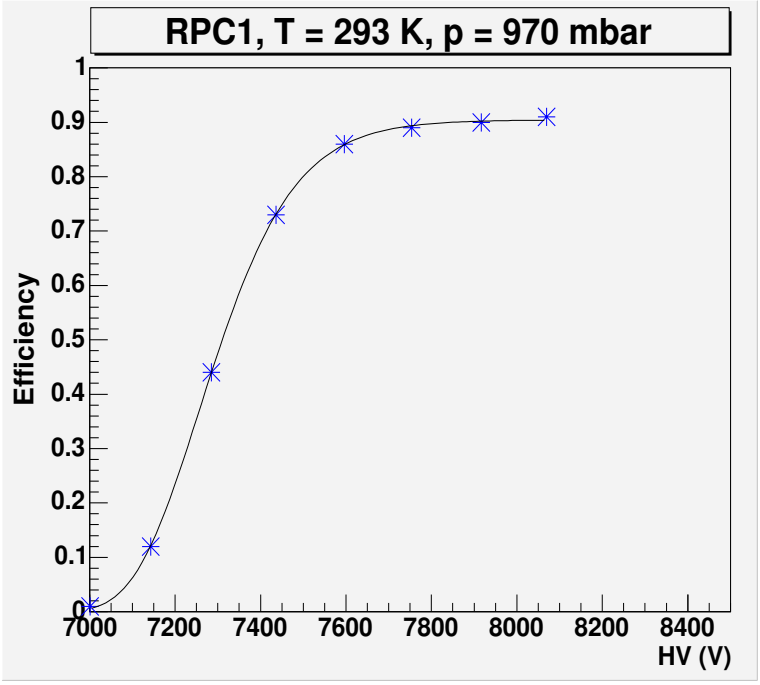

(b)

Figure 5.2: Cosmic rays efficiency curve of RPC1 as measured at GIF under irradiation (a) and with the Torino test station (b). All voltages are rescaled to p=970 mbar and T=293 K.

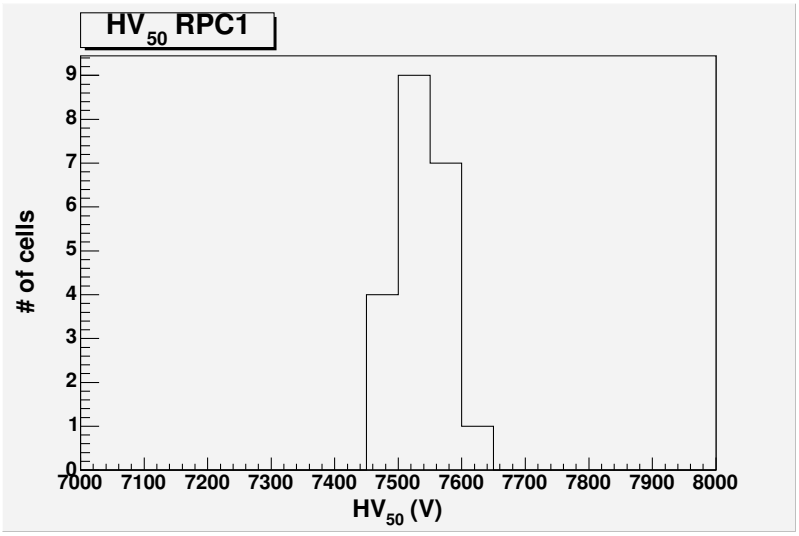

Figure 5.3: Distribution of the voltage values at 50% efficiency, over 21 17×23 cm^2 cells in which RPC1 was divided for the analysis.

The high granularity efficiency map in cells of 1.5×1.5 cm^2 has been measured: it is shown in Fig. 5.4. The leftmost area of the map contains no events, due to the vanishing acceptance of the tracking system. The detector exhibits good uniformity throughout its surface: with the exception of a narrow band on the rightmost side, the efficiency is above 90%, everywhere. Once more, it is worth pointing out that the efficiency is underestimated by about 4% due to the systematic error arising from fake tracks. The lower efficiency region on the right side happens to be in the most weakly shielded area; however, its dimensions (about 20×70 cm^2) are much smaller than the most irradiated area (about 70×70 cm^2) in Fig. 5.1, so that no evident correlation with ageing can be inferred: the efficiency problem is most likely intrinsic to the detector.

In conclusion, no permanent alteration in the detector seems to have occurred after a 100 Mhits/cm^2 irradiation. The performances of the detector (at least at source-off) are completely restored after switching it off for a while. This is confirmed by the dark current value measured at 8100 V: 2.4 μA, much lower than the value measured at similar voltages at the end of the ageing test (about 12 μA, see Fig. 3.10). Moreover, it has to be pointed out that the irradiation rate of the detectors in ALICE during heavy ion operation will not be as high as at GIF. In the case of Pb-Pb collisions, the rate (1$\div$5 Hz/cm^2) will be closer to the one in Turin (no source, only cosmic rays) than to the one at GIF ($\simeq$60 Hz/cm^2 in the most irradiated area).

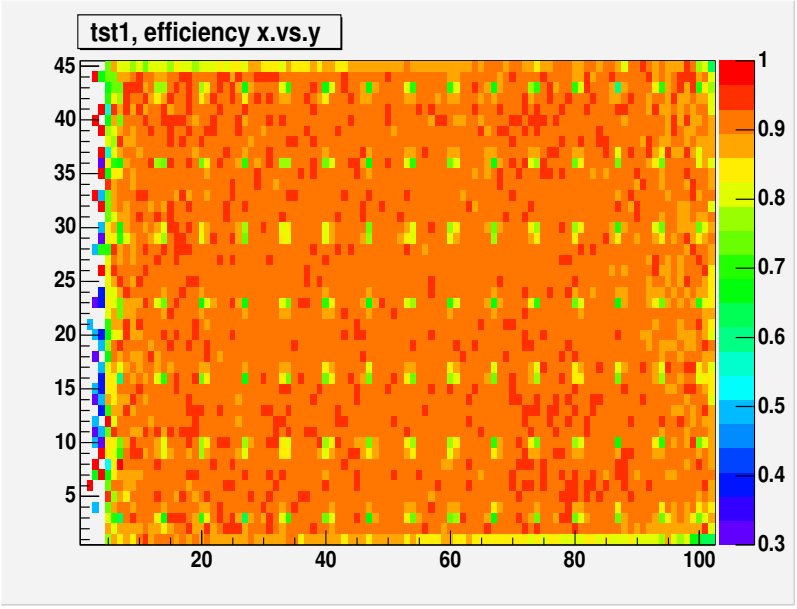

Figure 5.4: Efficiency map of RPC1 measured in Torino at 8100 V (voltage rescaled at GIF conditions). Units are given in cells. The area of the cells is 1.5×1.5 cm^2.

5.2 Ageing in highly saturated avalanche: RAV3 and RAV4

The prototypes RAV3 and RAV4 have been tested with a muon beam at the X5-GIF facility[1], with the avalanche mixture with 0.3% SF_6 adopted for p-p operation. After the beam test, they have undergone an ageing test (about 550 Mhit/cm^2), whose results are summarised in Sec. 3.2.3. The same prototypes have later been tested in Torino. Concerning the test in Torino, it is important to remark that, since the two prototypes have been tested together, it has been possible to measure the efficiency with the corrected method described in Sec. 4.2.3, i.e. by reconstructing the tracks with three points instead of two, thus reducing drastically the systematics. This allows a much more meaningful comparison of the results with those obtained in the beam test.

The efficiency curve for RAV3 at source-off measured during the beam test is shown in Fig. 5.5(a), while the one measured in Torino is shown in Fig. 5.5(b). The curves have been both rescaled to common temperature and

[1]The X5 beam is extracted from the SPS and brought to the GIF area.

pressure values, so that effective voltages are well defined. Analogous plots are shown for RAV4 in Figs. 5.6(a) and 5.6(b). For both prototypes, no significant displacement or deformation of the curve can be appreciated. In Figs. 5.5(b) and 5.6(b), the streamer contamination as measured in Torino is also shown: it has been measured by setting the 80 mV threshold for streamer operation on the front-end electronics of one of the two read-out planes, and computing the ratio between the efficiencies of the two planes. The behaviour of the streamer contamination is compatible with the one measured during the beam test before the ageing period (Figs. 5.7(a) and 5.7(b)).

During the beam tests, the efficiency has been measured in different positions of the prototypes, by means of moving supports allowing to place different zones of the detectors in front of the beam. The area of the tested cells was 10×10 cm^2. An efficiency map with the same granularity at the same voltage has been measured in Torino after the ageing period, to look for possible alterations in the uniformity of the detector. The comparison between the two measurements is shown in Figs. 5.8(a) and 5.8(b) for RAV3, in Figs. 5.9(a) and 5.9(b) for RAV4.

It is worth nothing that the inefficient zones of RAV4 are essentially the same as before the ageing period: they are thus intrinsical to the detector and not related to ageing. Concerning RAV3, the picture is similar but three out of the four corner cells show lower efficiency; this is not observed in the map measured during the beam test. Nevertheless, the effect can be explained by considering that the beam spot is actually smaller than the size of the cells, so that the efficiency associated to the cell in the beam test is actually the efficiency in the most central region of the cell. The cosmic ray map, instead, can probe the corners of the detectors, where inefficiencies are most likely to occur. This is confirmed by the analysis of a higher granularity map of the same detector (Fig. 5.10): it emerges clearly that only small regions in the corner of the detector are inefficient, while the rest shows good uniformity.

The conclusion that can be drawn from the comparison between pre-ageing and post-ageing data is that there is no evidence for a permanent performance degradation of the detectors due to ageing effects.

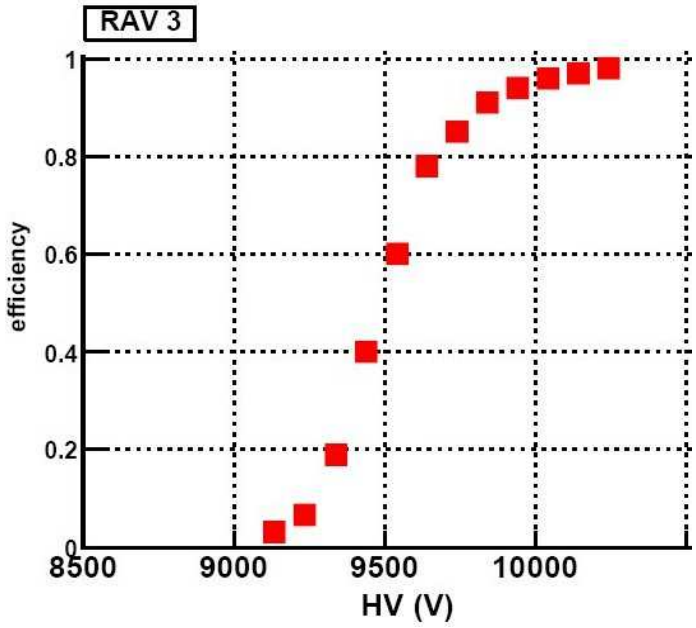

(a)

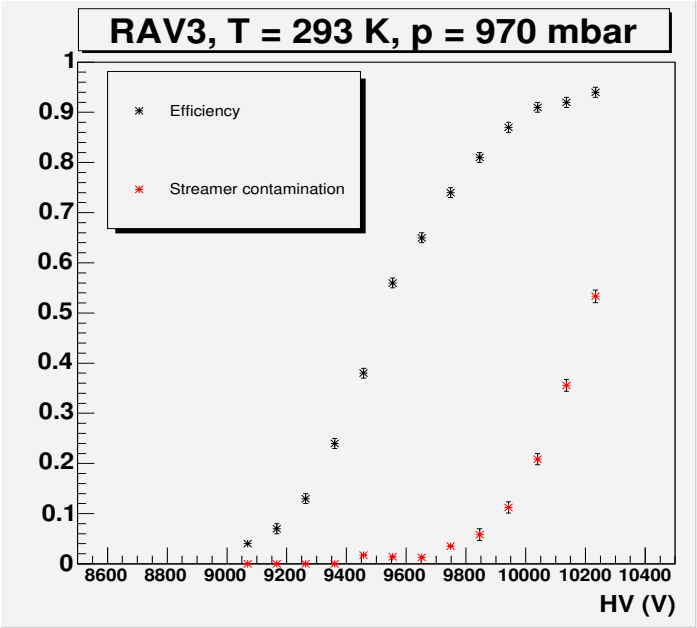

(b)

Figure 5.5: Cosmic rays efficiency curve of RAV3 as measured at GIF under irradiation (a) and with the Torino test station (b). All voltages are rescaled to p=970 mbar and T=293 K. The streamer contamination as measured in Torino is also shown.

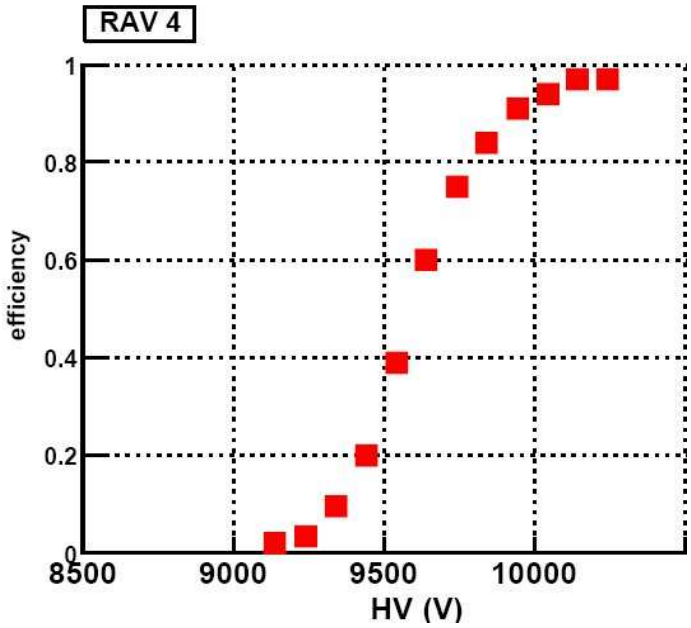

(a)

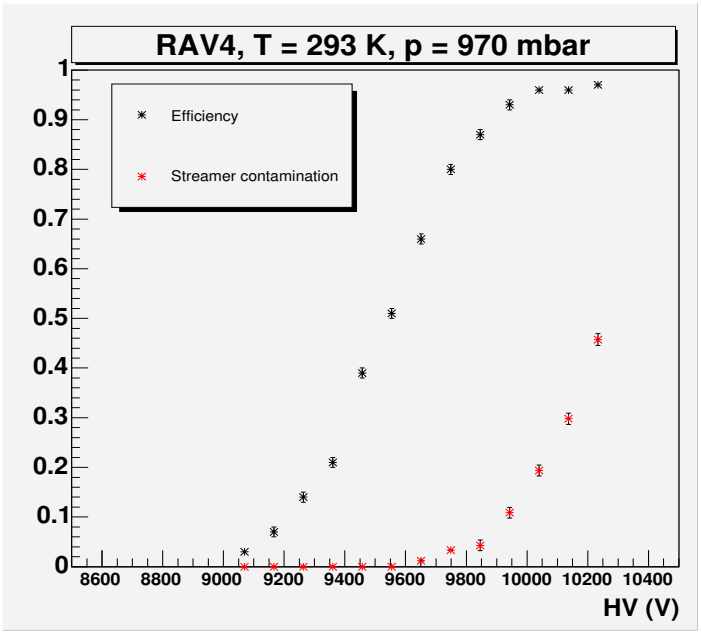

(b)

Figure 5.6: Cosmic rays efficiency curve of RAV4 as measured at GIF under irradiation (a) and with the Torino test station (b). All voltages are rescaled to p=970 mbar and T=293 K. The streamer contamination as measured in Torino is also shown.

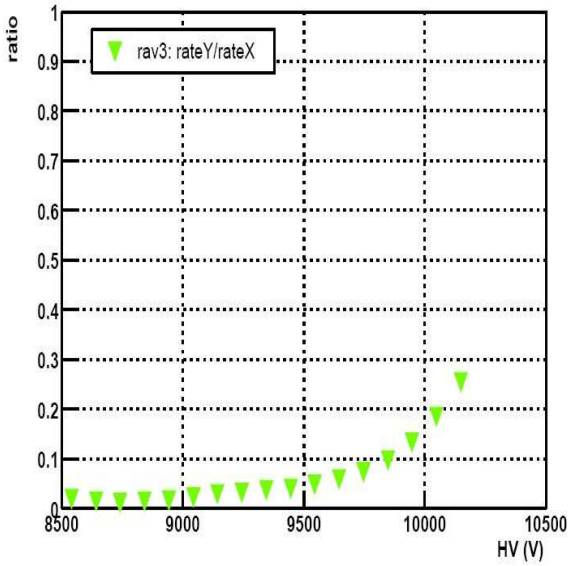

(a)

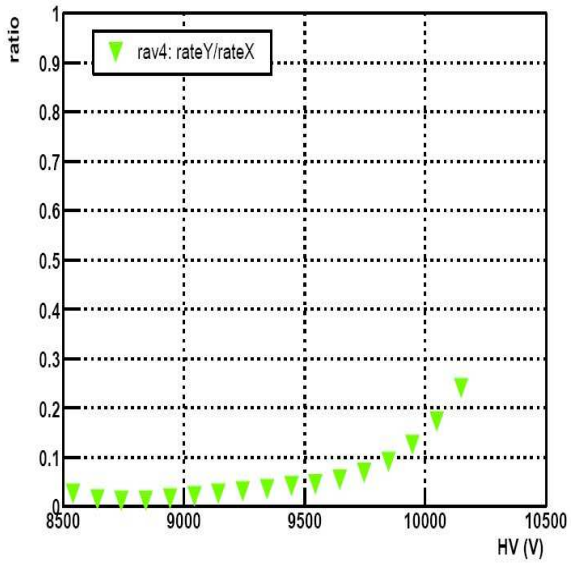

(b)

Figure 5.7: RAV3 (a) and RAV4 (b) streamer contamination as measured during the beam test at GIF, for a 25 Hz/cm^2 irradiation rate.

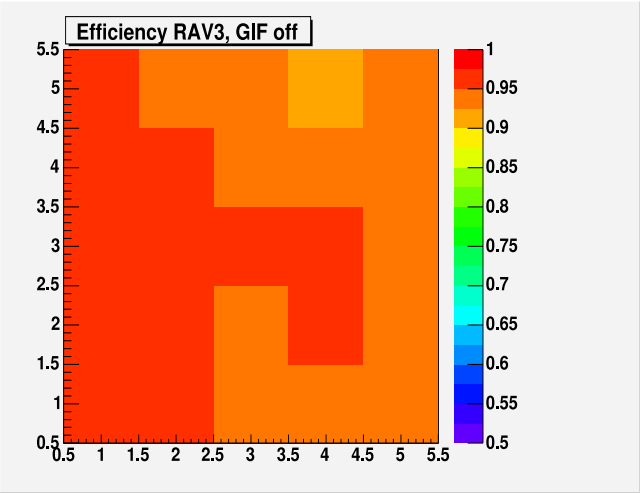

(a)

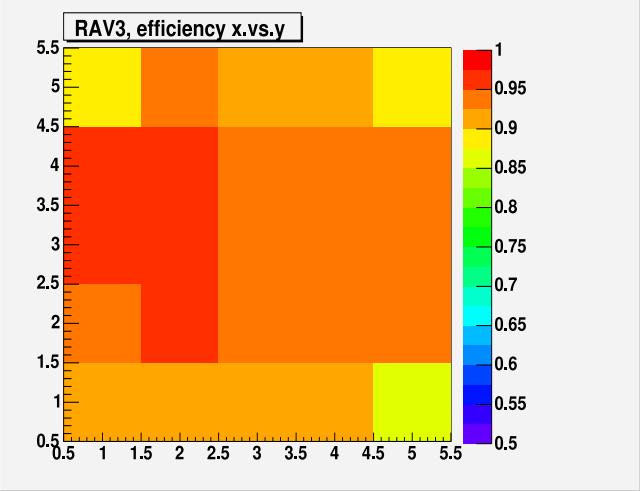

(b)

Figure 5.8: Efficiency map of RAV3 at 10100 V, as measured during the beam test(a) and with the Torino test station (b). Units are given in cells. The area of the cells is 10×10 cm^2.

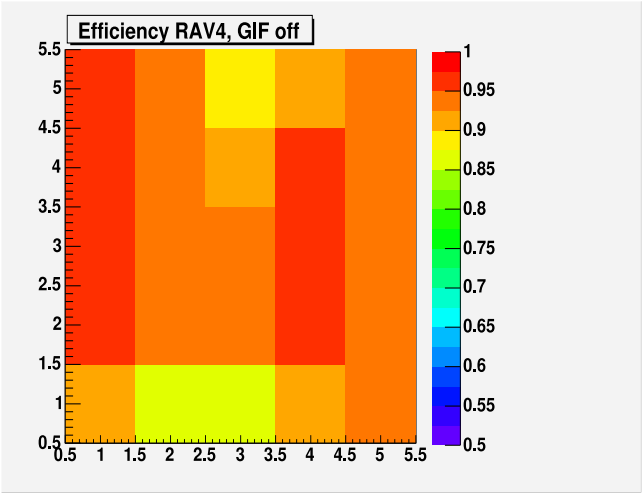

(a)

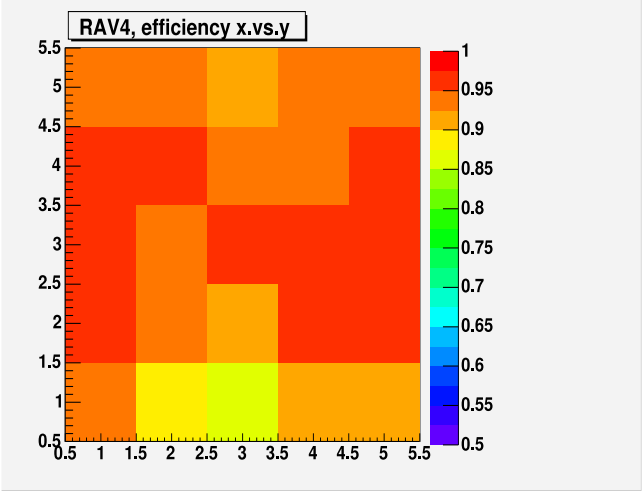

(b)

Figure 5.9: Efficiency map of RAV4 at 10100 V, as measured during the beam test(a) and with the Torino test station (b). Units are given in cells. The area of the cells is 10×10 cm^2.

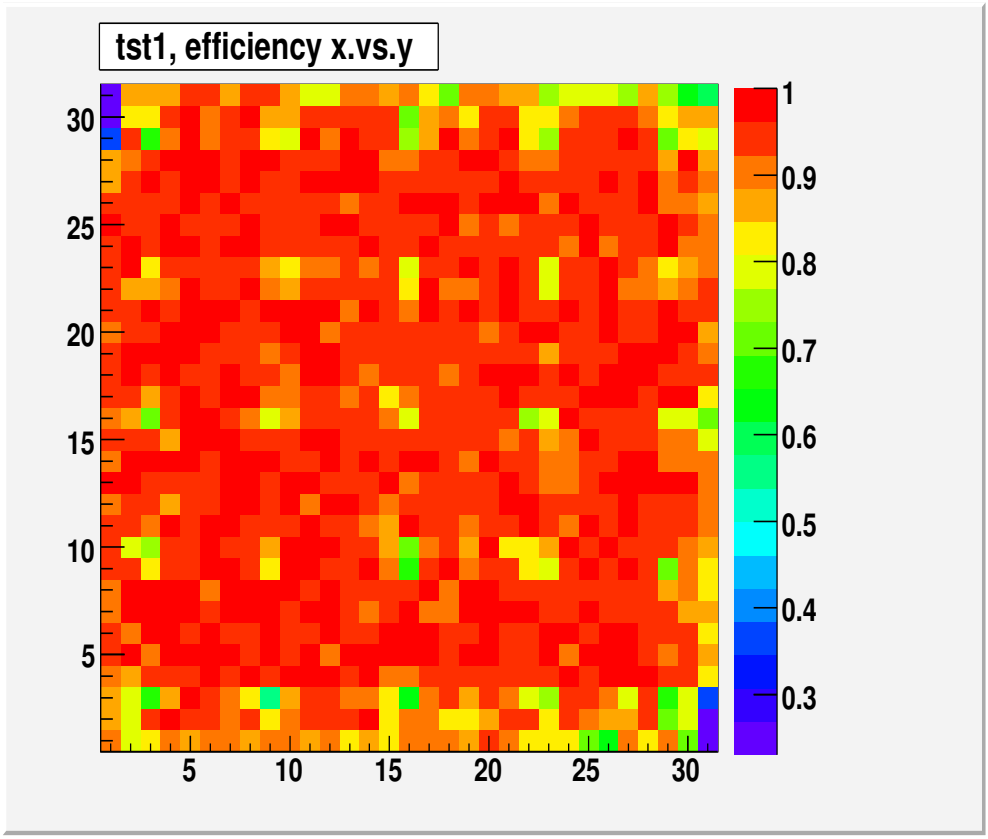

Figure 5.10: Efficiency map of RAV3 at 10100 V, as measured during the beam test(a) and with the Torino test station (b). Units are given in cells. The area of the cells is 1.5×1.5 cm^2.

Chapter 6

Quarkonia detection in p-p collisions

6.1 Quarkonia suppression studies: the problem of normalisation

As it was explained in Sec. 1.2.3, one of the relevant variables to study quarkonia suppression is the nuclear modification factor R^{AA} (see e. g. Fig. 1.24). It has already been defined, but it is worth recalling it here:

$$R_C^{AA}(c) = \frac{\sigma_{inel}^{pp} N_C^{AA}(c)}{\sigma_C^{pp} N_{binary}(c)} \tag{6.1}$$

where σ_{inel}^{pp} and σ_C^{pp} are the inelastic cross section and the measured cross section for the production of the quarkonium state C in p-p collisions, respectively, $N_C^{AA}(c)$ is the measured number of quarkonia C per A-A collision at centrality c and $N_{binary}(c)$ is the number of binary collisions for the same centrality. The centrality is estimated from experimental quantities such as the total number of charged particles, the transverse energy or the energy deposited in a Zero Degree Calorimeter by the spectator nucleons. $N_{binary}(c)$ is calculated according to models. The $R^{AA}(c)$ pattern must be compared with the pattern one would obtain if only cold nuclear matter effects such as shadowing and nuclear absorption were present, to disentangle the genuine effects of Quark Gluon Plasma formation.

The σ_C^{pp} appearing in the denominator of $R_C^{AA}(c)$ must of course refer to the same p-p energy in the centre of mass as the energy per nucleon pair of the A-A collisions. At the LHC, the energy per nucleon pair in Pb-Pb collisions will be 5.5 TeV, while the centre-of-mass energy of p-p collisions will be 14 TeV. The correct cross section value must then be obtained either

by rescaling p-p cross sections measured at 14 TeV or by applying for a dedicated p-p run at 5.5 TeV. In the first case, the measurement will be affected by systematic errors that will have to be estimated, while in the second case the statistical error will be dominant.

In the following sections, the two approaches have been considered: in Sec. 6.2 the physics performance of the ALICE muon spectrometer in a p-p run at 5.5 TeV will be presented, evaluated by means of simulations in the AliROOT[67, 68] framework, while in Sec. 6.3 the scaling factors to an energy of 5.5 TeV of Υ and J/ψ production cross sections measured at 14 TeV (and relative theoretical uncertainties) are evaluated in the frame of the Color Evaporation Model production scheme.

6.2 Physics performance of the ALICE muon spectrometer in p-p collisions at 5.5 TeV

A proton-proton run at $\sqrt{s} = 5.5$ TeV is not scheduled at the moment in the LHC program. Nevertheless, such a run would be of great interest for the purposes of ALICE and of the other experiments with a heavy ion program at the LHC, so the collaborations will most likely apply for such a run. It is interesting to evaluate what the performances of the ALICE Muon Spectromer would be in such a run, and what Υ and J/ψ statistics could be collected in a 1-month (10^6 s) run at the nominal luminosity of $3\times\ 10^{30}$ cm^{-2} s^{-1}.

6.2.1 Simulation approach and input

The muon spectrometer performance has been evaluated by means of simulation. The same strategy that was developed for the nominal p-p program at 14 TeV[39, 40] was used; it is the following:

- quarkonia (J/ψ and Υ) have been generated according to parametrisations given by the Color Evaporation Model[15] The number of expected particles is calculated assuming Next-to-Leading order Color Evaporation Model cross sections[39, 69], summarised in Tab. 6.1;

- the kinematics of quarkonia decay into muons has been generated with the PYTHIA[70] decayer tool;

- the response of the muon spectrometer has been evaluated by means of the AliROOT Fast Simulation classes, thus obtaining the p_T and

rapidity yields as measured by the muon spectrometer, which can be integrated to obtain the total yield of detected quarkonia;

- the detection probability has been evaluated as a function of p_T and rapidity by means of high statistics generations;

- the p_T and rapidity yields have been corrected with the detection probabilities, to evaluate how well the differential cross sections are reproduced by the muon spectrometer.

Since such a study should be considered preliminary, the background was not included and the J/ψ feed down from B-meson decays ($\simeq$ 20% of the total J/ψ yield) was neglected. The J/ψ yields and cross sections mentioned in the following refer to prompt J/ψ, i.e.:

- J/ψ directly produced in the primary collision;

- J/ψ decays of higher charmonium states such as ψ' or χ_C produced in the primary collision (about 40% of the total prompt J/ψ yield).

In case the possibility for a p-p run at 5.5 TeV becomes more than a hypothesis, a more detailed study including background and the B-decay J/ψ feed down will be needed, as it was carried out for the 14 TeV case.

$\sqrt{s}$	5.5 TeV	14 TeV
$BR^{\mu\mu}\sigma_{J/\psi}$	1.8μb	3.2 μb
$BR^{\mu\mu}\sigma_{\Upsilon}$	12 nb	28 nb

Table 6.1: Cross sections for J/ψ and Υ production in proton-proton collisions at an energy in the centre of mass of 5.5 and 14 TeV, calculated at NLO with MRSTHO PDF according to the Color Evaporation Model.

Rapidity distributions

The input J/ψ and Υ rapidity distributions at 5.5 TeV have been obtained from the plots in Ref. [69]: they are the result of a Next-to-Leading Order Color Evaporation Model calculation using the MRSTHO[71] Parton Distribution Functions set. They are shown in Figs. 6.1 and 6.2, together with the rapidity distributions at 14 TeV.

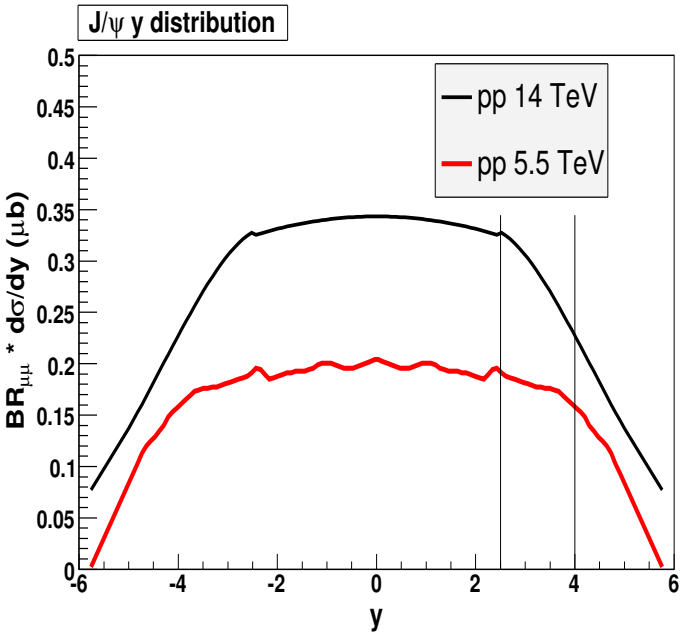

Figure 6.1: Color Evaporation Model J/ψ rapidity-differential cross section at 5.5 TeV and 14 TeV, calculated at NLO with the MRSTHO PDF set. The two black vertical lines represent the rapidity window covered by the muon spectrometer.

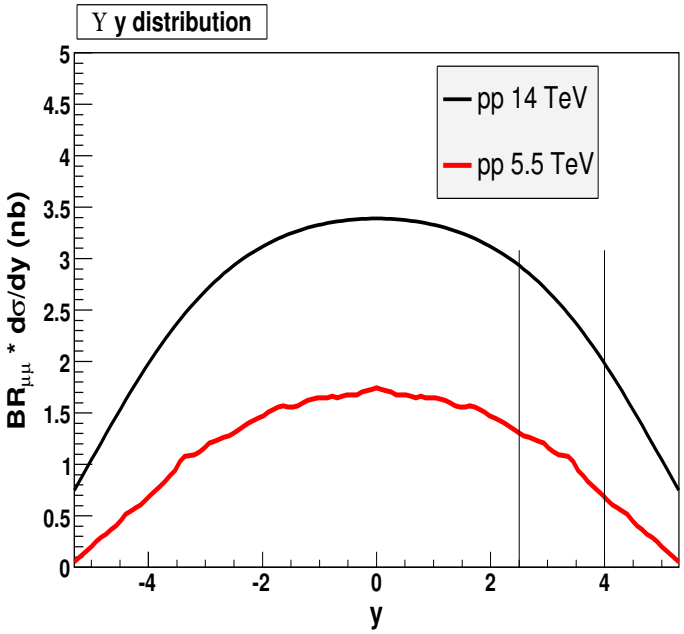

Figure 6.2: Color Evaporation Model Υ rapidity-differential cross section at 5.5 TeV and 14 TeV, calculated at NLO with the MRSTHO PDF set. The two black vertical lines represent the rapidity window covered by the muon spectrometer.

Transverse momentum distributions

The p_T distributions have been obtained by rescaling the ones measured by the CDF collaboration[72] at an energy in the centre of mass of 1.96 TeV. The Color Evaporation Model predicts a broadening of such distributions[73] with increasing energy due to initial state interactions with gluons. In particular, predictions are available for the evolution with $\sqrt{s}$ of the $< p_T^2 >$ of the distribution (Figs. 6.3(a) and 6.3(b)).

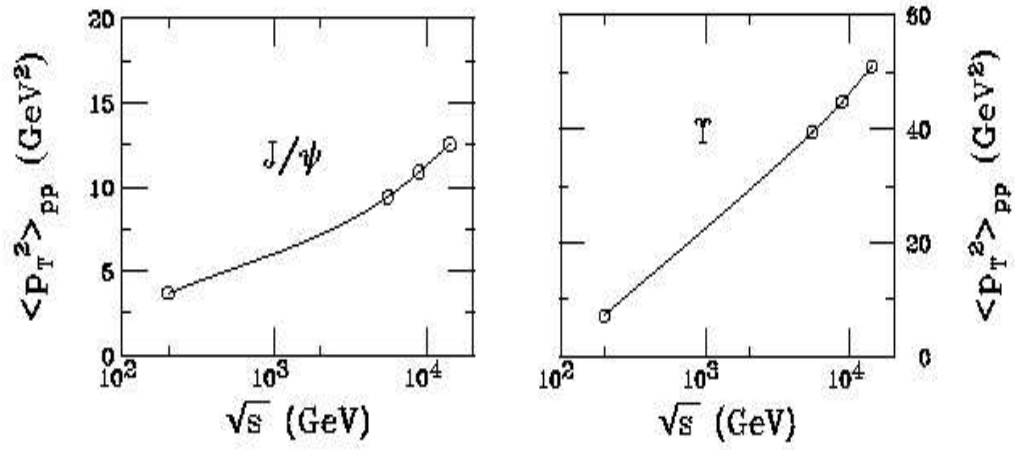

(a) (b)

Figure 6.3: Energy evolution of the $< p_T^2 >$ of the distribution for J/ψ (a) and Υ (b), according to the Color Evaporation Model predictions, from Ref. [73].

In order to perform the rescaling, the CDF distribution has been fitted with a suitable function:

$$\frac{dN}{dp_T} = C \frac{p_T}{[1 + (\frac{p_T}{A})^2]^n} \tag{6.2}$$

The $< p_T^2 >$ of the distribution is given by:

$$< p_T^2 >= \frac{A^2}{n-2} \tag{6.3}$$

The adopted strategy is to keep n constant and vary A in order to match the Color Evaporation Model prediction. The new value of the A parameter is

fed back into Eq. 6.2 to obtain the rescaled p_T distribution. The resulting p_T distributions for J/ψ and Υ are shown in Figs. 6.4 and 6.5.

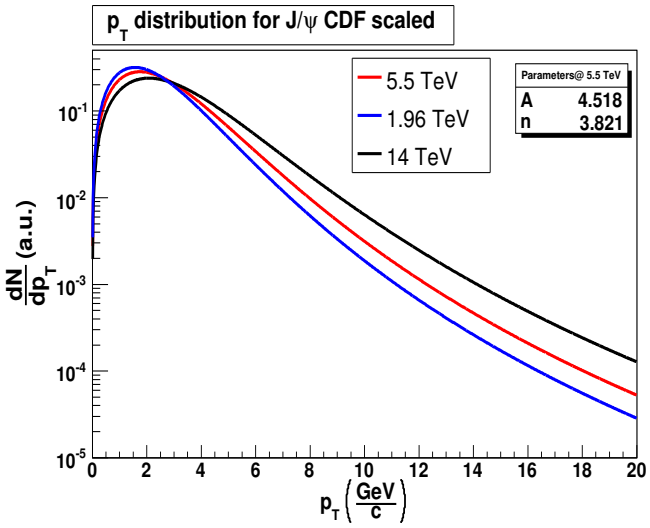

Figure 6.4: J/ψ p_T distribution at 1.96 TeV (fit from CDF), 5.5 TeV and 14 TeV (rescaled). All distributions are normalised to 1.

6.2.2 Muon spectrometer response

The AliROOT Fast Simulation[39] tool provides classes that evaluate the detector response according to parametrisations, without performing a time-consuming full simulation. Such parametrisations account for the acceptance and efficiency of both the trigger and the tracking system for a muon with a given set of kinematical variables (p_T, θ, ϕ). Such classes are:

- `AliFastMuonTriggerEff`: evaluates the probability that the muon be triggered by the trigger system;
- `AliFastMuonTrackingAcc`: evaluates the probability that the muon track be in the acceptance of the tracking system;
- `AliFastMuonTrackingEff`: evaluates the probability that a track in the acceptance of the tracking system be reconstructed.

The probabilities evaluated by the above classes result in a weight assigned to the particle. The overall detection probability for each particle, i.e. the convolution of all weights, is taken into account when counting the particles

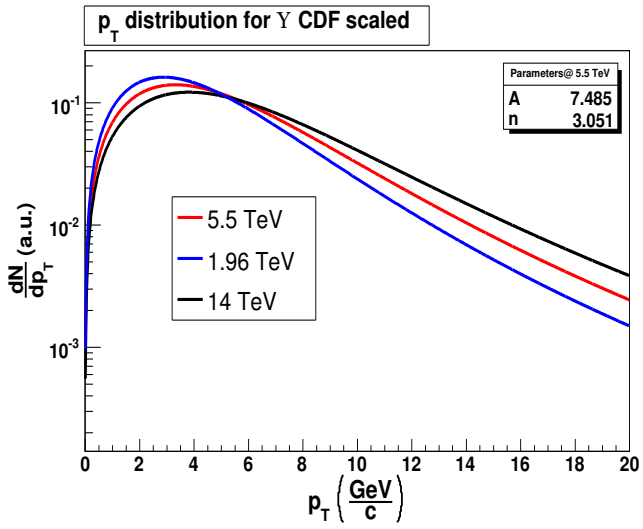

Figure 6.5: Υ p_T distribution at 1.96 TeV (fit from CDF), 5.5 TeV and 14 TeV (rescaled). All distributions are normalised to 1.

and filling the histograms. One more class (`AliFastMuonTrackingRes`) performs the smearing, i.e. extracts the reconstructed kinematical variables of the muon according to a probability distribution that takes into account the detector resolution.

Raw yields

The number of detected J/ψ (Υ) in 10^6 s is about 15200 (1300) for a luminosity of $3{\times}10^{30}$ $s^{-1}cm^{-2}$. A more precise estimation of such numbers will be given in the following, together with the determination of the absolute muon spectrometer efficiency.

The raw p_T-differential yields for J/ψ and Υ are shown in Figs. 6.6 and 6.7 respectively. The J/ψ yield ranges from about 30 $(GeV/c)^{-1}$ at $p_T \simeq$20 GeV/c to about 30000 $(GeV/c)^{-1}$ at $p_T \simeq$2 GeV/c, while the Υ yield ranges from about 10 $(GeV/c)^{-1}$ at $p_T \simeq$15 GeV/c to about 200 $(GeV/c)^{-1}$ at $p_T \simeq$4 GeV/c.

The raw rapidity-differential yields for J/ψ and Υ are shown in Figs. 6.8 and 6.9 respectively. The J/ψ yield ranges from about 20000$\div$40000 per rapidity unit at the edges of the muon spectrometer rapidity window to about 170000 per rapidity unit at y$\simeq$3.3, while the Υ yield ranges from about 400$\div$600 per rapidity unit at the edges of the muon spectrometer rapidity window to about 1400 per rapidity unit at y$\simeq$3.1.

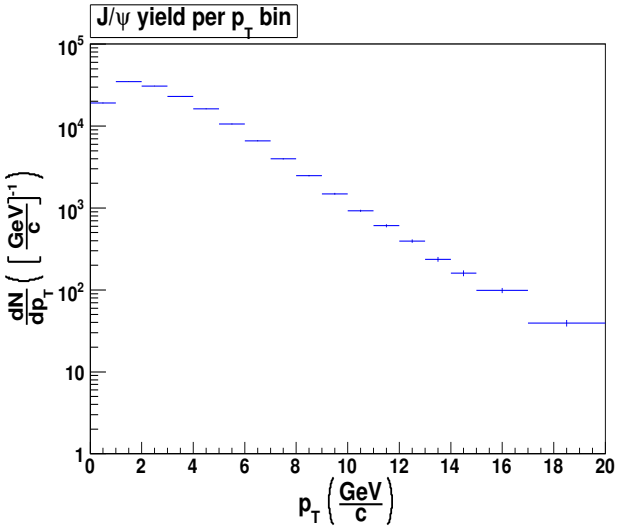

Figure 6.6: Expected p_T-differential J/ψ yield in the muon spectrometer in a p-p run of 10^6 s at $\sqrt{s}$=5.5 TeV, for a luminosity of 3×10^{30} $s^{-1}cm^{-2}$.

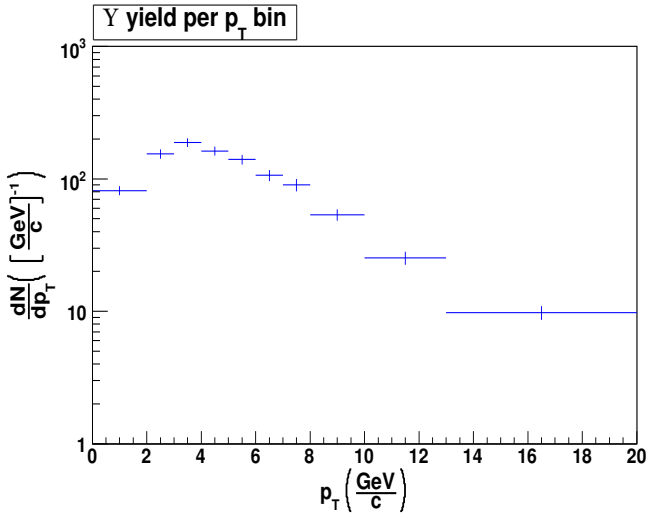

Figure 6.7: Expected p_T-differential Υ yield in the muon spectrometer in a p-p run of 10^6 s at $\sqrt{s}$=5.5 TeV, for a luminosity of 3×10^{30} $s^{-1}cm^{-2}$.

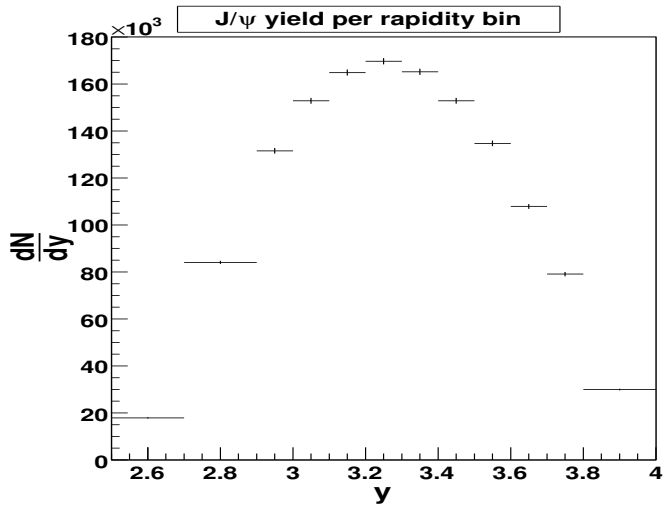

Figure 6.8: Expected rapidity-differential J/ψ yield in the muon spectrometer in a p-p run of 10^6 s at $\sqrt{s}$=5.5 TeV, for a luminosity of 3×10^{30} s^{-1}cm^{-2}.

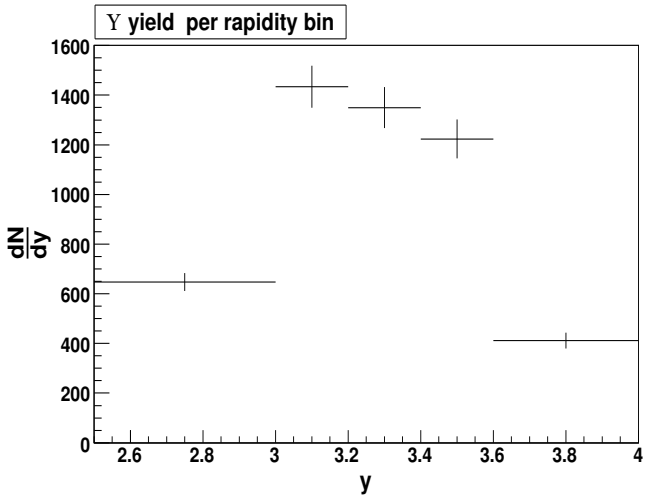

Figure 6.9: Expected rapidity-differential Υ yield in the muon spectrometer in a p-p run of 10^6 s at $\sqrt{s}$=5.5 TeV, for a luminosity of 3×10^{30} s^{-1}cm^{-2}.

Efficiencies

The quarkonia acceptance and efficiency of the muon spectrometer have been evaluated by generating a high statistics sample (10^8 in the y>0 rapidity interval) of J/ψ and Υ. The total quarkonia detection probability as a function of p_T (rapidity) can be obtained as the ratio of detected to generated quarkonia in a given p_T (y) bin.

The J/ψ and Υ detection efficiency as a function of rapidity is shown in Figs. 6.10 and 6.11: it is maximum for rapidities around 3.2 (where it is 32% for J/ψ and 45% for Υ) and vanishes at the edges of the muon spectrometer window (y =2.5 and y =4).

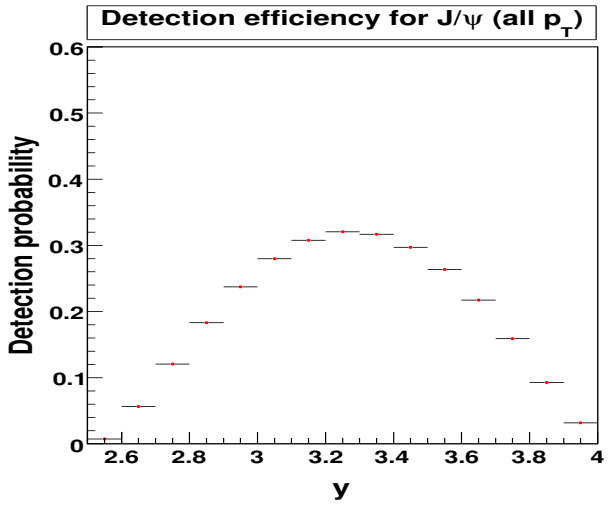

Figure 6.10: J/ψ detection probability in the muon spectrometer as a function of rapidity.

The detection efficiency as a function of p_T for J/ψ and Υ with 2.5<y<4 is shown in Figs. 6.12 and 6.13: such a detection probability increases with p_T, but it is non-vanishing at zero p_T for both quarkonium states: this is a peculiar feature of the ALICE muon spectrometer.

The total efficiency of the muon spectrometer, defined as the ratio between detected and generated quarkonia (over the whole phase space) is 2.8% for J/ψ and 3.6% for Υ. By multiplying such efficiencies by the cross section, branching ratio, luminosity and data-taking time, the total expected quarkonia yields can be obtained: such yields are 152350 for J/ψ and 1294 for Υ. The statistical error on the determination of efficiency is negligible with respect to the expected poissonian fluctuations of the yield. The expected

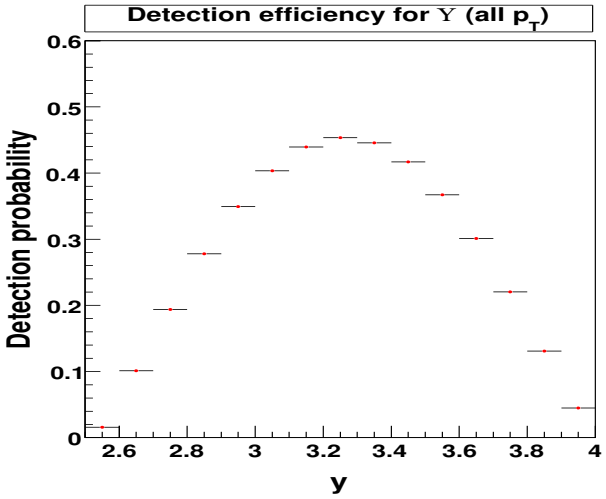

Figure 6.11: Υ detection probability in the muon spectrometer as a function of rapidity.

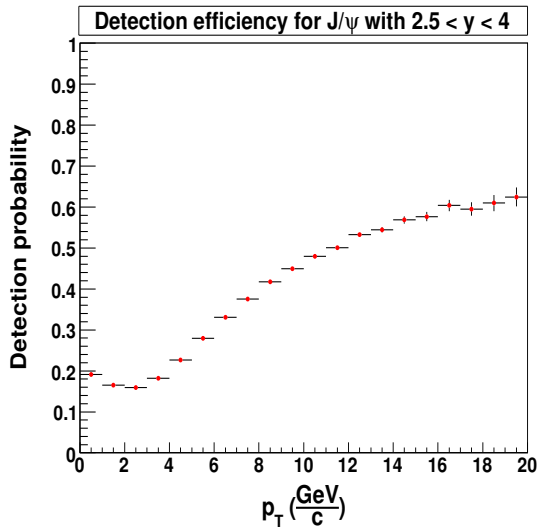

Figure 6.12: Detection probability in the muon spectrometer as a function of p_T for J/ψ with $2.5 < y < 4$.

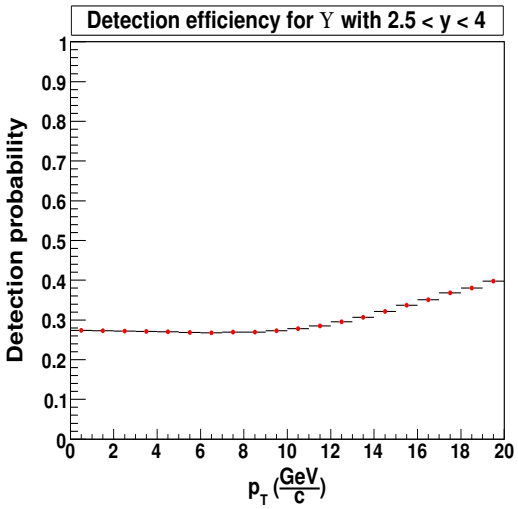

Figure 6.13: Detection probability in the muon spectrometer as a function of p_T for Υ with $2.5 < y < 4$.

number of detected quarkonia is:

$$152400 \pm 400\ J/\psi; \quad 1290 \pm 40\ \Upsilon$$

Of course the uncertainties on the measured cross sections will be larger, due to the error on background subtraction and on the measurement of luminosity. These are not taken into account in this study, since the aim of this work is to give an estimate of how much statistics will be available in such a data-taking scenario.

To summarise the muon spectrometer performances at 5.5 TeV, the total efficiency and the quarkonia yields are reported in Tab. 6.2. For comparison, the results at 14 TeV are also reported. The values of acceptance and efficiency are substantially the same as those found at 14 TeV: the large difference in yield is mainly due to the cross section and to the scheduled data-taking time. The reader should note that the J/ψ yield at 14 TeV includes the contribution from B meson decays, not included in the yield at 5.5 TeV reported here.

6.2.3 Measurement of the differential cross sections

Once the efficiency ϵ for each p_T and rapidity bin is known, the raw p_T and rapidity differential yields shown in Figs. 6.6 through 6.9 can be corrected

$\sqrt{s}$	5.5 TeV	14 TeV
Data taking time per year	10^6 s	10^7 s
J/ψ acceptance	4.3%	4.2%
J/ψ efficiency	2.8%	2.7%
J/ψ yield	1.5×10^5	2.4×10^6
Υ acceptance	4.2%	4.2%
Υ efficiency	3.6%	3.6%
Υ yield	1.3×10^3	2.9×10^4

Table 6.2: Muon spectrometer expected yields and efficiencies for heavy quarkonia detection at 5.5 TeV and 14 TeV. All the reported yields refer to a luminosity of 3×10^{30} cm^{-2} s^{-1}.

and divided by the luminosity $\mathcal{L}$ and data-taking time Δt to obtain the differential cross sections:

$$BR_{\mu\mu}\frac{d\sigma}{dp_T} = \frac{1}{\Delta t \mathcal{L}}\frac{1}{\epsilon(p_T)}\frac{dN}{dp_T}; \quad BR_{\mu\mu}\frac{d\sigma}{dy} = \frac{1}{\Delta t \mathcal{L}}\frac{1}{\epsilon(y)}\frac{dN}{dy} \tag{6.4}$$

The p_T-differential cross sections for J/ψ and Υ, obtained with eq. 6.4, are shown in Figs. 6.14 and 6.15 respectively. In both cases the input parametrisations are reproduced within the errors by the measured cross sections. The J/ψ cross section can be measured in bins of 1 GeV/c with a statistical error ranging from 1% to 8% up to p_T = 15 GeV/c, while the measurement at higher transverse momenta is possibile in bins of 2$\div$3 GeV/c with a statistical error smaller than 10%. The Υ cross section can be measured in bins of 1$\div$2 GeV/c with a statistical error of about 10% up to p_T = 10 GeV/c, while the measurement at higher transverse momenta is possibile in bins of 3$\div$5 GeV/c with a statistical error of aboout 12%.

The rapidity-differential cross sections for J/ψ and Υ, obtained with eq. 6.4, are shown in Figs. 6.16 and 6.17 respectively. In both cases the input parametrisations are reproduced within the errors by the measured cross sections. The J/ψ cross section can be measured in bins of 0.1 units of rapidity with a statistical error lower than 1% for rapidities between 2.7 and 3.6, while in the rest of the rapidity window the statistical error ranges from 1% to 2% in bins of 0.2 units of rapidity. The Υ cross section can be measured with a statistical error ranging from 5% to 8%, with bin sizes ranging from 0.2 to 0.5 units of rapidity.

Once more, it has to be pointed out that the errors reported here only take into account the statistical error, since background subtraction (and the consequent systematic uncertainties) has not been included in this work.

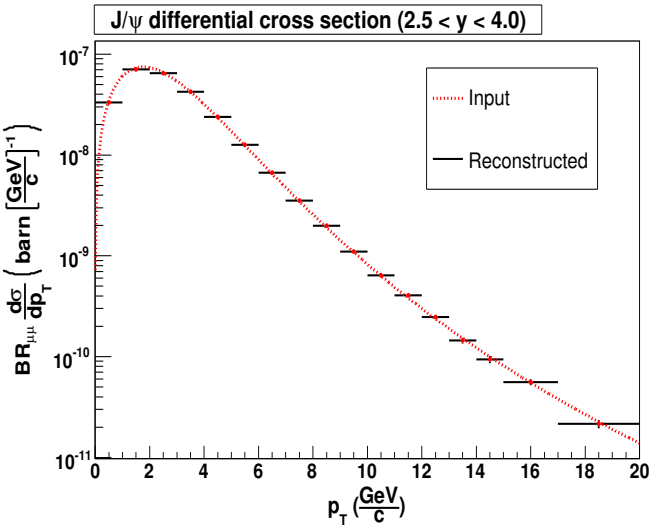

Figure 6.14: Monte Carlo J/ψ p_T-differential cross section at 5.5 TeV as measured by the ALICE muon spectrometer in a p-p run of 10^6 s, for a luminosity of 3×10^{30} $s^{-1}cm^{-2}$. The input parametrisation used for the simulation is also shown.

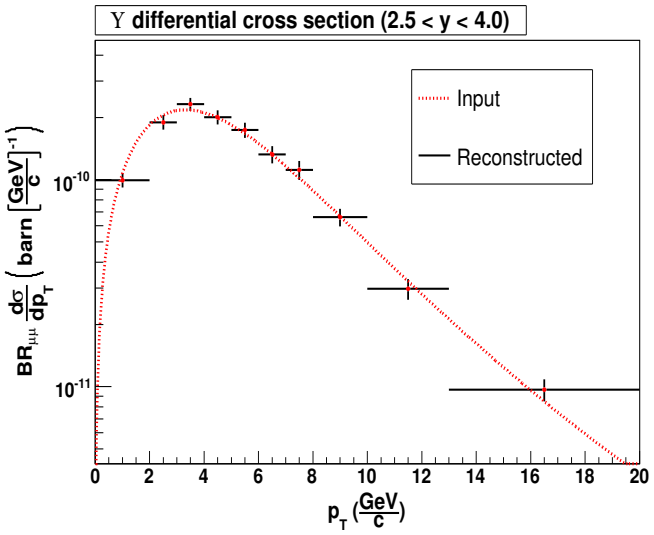

Figure 6.15: Monte Carlo Υ p_T-differential cross section at 5.5 TeV as measured by the ALICE muon spectrometer in a p-p run of 10^6 s, for a luminosity of 3×10^{30} $s^{-1}cm^{-2}$. The input parametrisation used for the simulation is also shown.

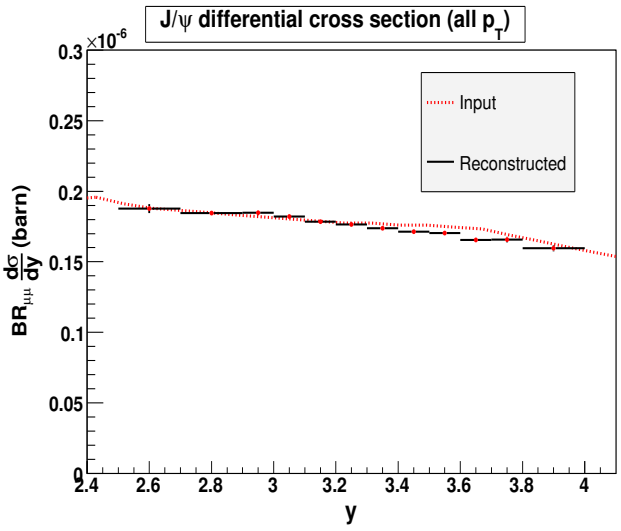

Figure 6.16: Monte Carlo J/ψ rapidity-differential cross section at 5.5 TeV as measured by the ALICE muon spectrometer in a p-p run of 10^6 s, for a luminosity of 3×10^{30} $s^{-1}cm^{-2}$. The input parametrisation used for the simulation is also shown.

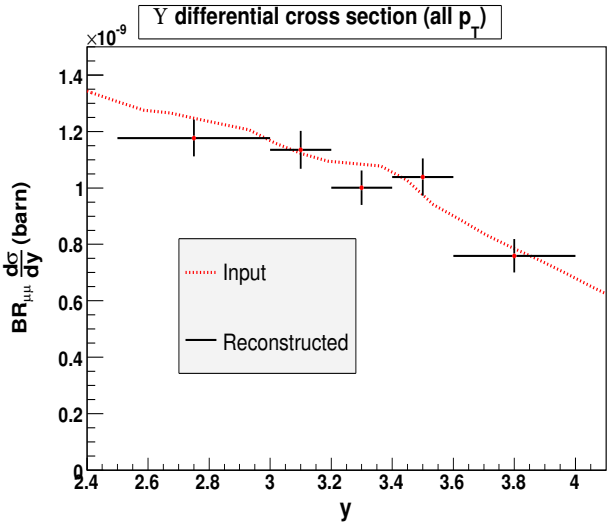

Figure 6.17: Monte Carlo Υ rapidity-differential cross section at 5.5 TeV as measured by the ALICE muon spectrometer in a p-p run of 10^6 s, for a luminosity of 3×10^{30} $s^{-1}cm^{-2}$. The input parametrisation used for the simulation is also shown.

6.3 Rescaling of p-p data at 14 TeV

In the previous section, the physics performance of the ALICE muon spectrometer in a dedicated p-p run at $\sqrt{s} = 5.5$ TeV has been analysed. As pointed out in Sec. 2.1.1, such a run is not in the present LHC schedule, so it is mandatory to develop a different strategy to estimate the denominator of R^{AA} as defined in Eq. 6.1, so that the quarkonia suppression patterns can be studied as soon as the first Pb-Pb data are available.

The measurement of quarkonia cross sections[1] in the ALICE muon spectrometer is limited to the rapidity region 2.5<y<4. In the following, the quantity σ_{MS} will be used to address the amount of cross section for quarkonium production that can be measured in the ALICE muon spectrometer:

$$\sigma_{MS} = \int_{2.5}^{4} \frac{d\sigma}{dy} dy \tag{6.5}$$

The rescaling of quarkonia cross sections from 14 TeV to 5.5 TeV can be performed by calculating σ_{MS} at the two energies and by determining the scaling factor:

$$S = \frac{\sigma_{MS}^{5.5}}{\sigma_{MS}^{14}} = \frac{\int_{2.5}^{4} \frac{d\sigma}{dy}^{5.5} dy}{\int_{2.5}^{4} \frac{d\sigma}{dy}^{14} dy} \tag{6.6}$$

The choice of the scaling factor is of course model-dependent: to be consistent with the choice made by the collaboration for the evaluation of the muon spectrometer physics performance in p-p (at 14 TeV) and Pb-Pb collisions, the calculation of the scaling factor will be carried out according to the Color Evaporation Model.
Since the considered quantity S is a ratio, possible uncertainties due to the overall normalisation of the cross section should eventually cancel out.

In Sec. 6.3.1 some useful Color Evaporation Model cross sections will be recalled; in Sec. 6.3.2 the expected scaling factors for σ_{MS} (total and in p_T bins) will be computed; in Sec. 6.3.3 the theoretical uncertainty on such values will be evaluated within the frame of Leading Order CEM.

6.3.1 The CEM framework

The production cross section for the quarkonium state C according to the Color Evaporation Model can be written as:

[1] In this section, as in the previous, the J/ψ cross sections only include prompt J/ψ.

$$\sigma_C = F_C \sum_{i,j} \int_{4m_Q^2}^{4m_H^2} d\hat{s} \int dx_1 dx_2 f_{i/A}(x_1, \mu_F^2) f_{j/B}(x_2, \mu_F^2) \hat{\sigma}_{ij}(\hat{s}) \delta(\hat{s} - x_1 x_2 s) \tag{6.7}$$

where:

- the indexes i and j run along the partons (quarks and gluons) in the two colliding hadrons A and B respectively;
- m_Q is the mass of the heavy quark Q forming the quarkonium state;
- m_H is the mass of the lightest meson containing the heavy quark Q;
- $\sqrt{\hat{s}}$ is the energy in the centre of mass of the elementary collision;
- $\hat{\sigma}_{ij}(\hat{s})$ is the elementary cross section for the process ij$\rightarrow Q\overline{Q}$;
- $f_{i/A}(x_1, \mu_F^2)$ is the parton distribution function of parton i in the hadron A, evaluated at the value x_1 of the Bjorken variable and at factorisation scale μ_F^2; the meaning of $f_{j/B}(x_2, \mu_F^2)$ is analogous;
- F_C is a constant, typical of the quarkonium state C but process- and kinematics-independent, representing the fraction of produced $Q\overline{Q}$ pairs that hadronise into the quarkonium state C.

The expected scaling factors will be determined using the Next-to-Leading Order calculations already mentioned in Sec. 6.2.1, and reported in Refs. [39] and [69]. Nevertheless, it is interesting to briefly recall the Leading Order Color Evaporation Model rapidity-differential cross section, for two reasons. First of all, because it gives information on how the difference in $\sqrt{s}$ affects the quarkonia cross section measurements in the ALICE muon spectrometer. Secondly, because the estimation of the theoretical uncertainty on the scaling factors (i.e. the uncertainty arising from the choice of the PDF set and of the factorisation scale), which will be described in Sec. 6.3.3, has been performed at Leading Order.

At Leading Order, the rapidity of the $Q\overline{Q}$ pair is given by:

$$y_{Q\overline{Q}} = \frac{1}{2} \ln \frac{x_1}{x_2} \tag{6.8}$$

so that[2]:

$$x_1 = \sqrt{\frac{\hat{s}}{s}} e^{y_{Q\overline{Q}}}; \quad x_2 = \sqrt{\frac{\hat{s}}{s}} e^{-y_{Q\overline{Q}}} \tag{6.9}$$

[2]Since $\hat{s}$=$x_1 x_2 s$.

Putting together Eqs. 6.7 and 6.9, integrating over x_1 and x_2 and deriving, one obtains for the rapidity-differential cross section:

$$\frac{d\sigma_C}{dy} = \frac{F_C}{s}\sum_{i,j}\int_{4m_Q^2}^{4m_H^2} d\hat{s}\hat{\sigma}_{ij}(\hat{s}) f_{i/A}(\sqrt{\frac{\hat{s}}{s}}e^{y}, \mu_F^2) f_{j/B}(\sqrt{\frac{\hat{s}}{s}}e^{-y}, \mu_F^2) \qquad (6.10)$$

The formulae in Eq. 6.9 provide an estimate of the regions of x_1 and x_2 corresponding to the ALICE muon spectrometer rapidity window. It is clear that such regions vary with $\sqrt{s}$: as a consequence, the shape of the rapidity distributions will be different at different energies.
Since in the CEM approximation $\hat{s}$ varies from $4m_Q^2$ to $4m_H^2$ (see the integral in Eq. 6.10), and in the muon spectrometer y varies from 2.5 to 4, the x_1 and x_2 regions can be estimated as:

$$\sqrt{\frac{4m_Q^2}{s}}e^{2.5} < x_1 < \sqrt{\frac{4m_H^2}{s}}e^{4}; \quad \sqrt{\frac{4m_Q^2}{s}}e^{-4} < x_2 < \sqrt{\frac{4m_H^2}{s}}e^{-2.5} \qquad (6.11)$$

The x_1 and x_2 region probed by J/ψ and Υ in the ALICE muon spectrometer, calculated with Eqs. 6.11, are shown in Tab. 6.3. Though such numbers are approximate results, they give an estimate of how small the x-values involved in the processes studied are: in such domain the measurements are scarce, and different collaborations have published different results. This is the reason why it will be interesting to calculate the scaling factor S defined in Eq. 6.6 for different choices of PDFs, thus evaluating the influence of the PDFs on the uncertainty affecting the rescaling process.

Resonance	J/ψ	Υ
m_Q (GeV/c^2)	1.2	4.5
m_H (GeV/c^2)	1.86	5.28
x_1 range at 5.5 TeV	$5.3\times10^{-3}\div3.7\times10^{-2}$	$2.0\times10^{-2}\div1.0\times10^{-1}$
x_1 range at 14 TeV	$2.1\times10^{-3}\div1.5\times10^{-2}$	$7.8\times10^{-3}\div4.1\times10^{-2}$
x_2 range at 5.5 TeV	$8.0\times10^{-6}\div5.6\times10^{-5}$	$3.0\times10^{-5}\div1.6\times10^{-4}$
x_2 range at 14 TeV	$3.1\times10^{-6}\div2.2\times10^{-5}$	$1.2\times10^{-5}\div6.2\times10^{-5}$

Table 6.3: Regions of x_1 and x_2 probed by J/ψ and Υ in the ALICE muon spectrometer at 5.5 TeV and 14 TeV, according to Eq. 6.9.

Since, as pointed out in Sec. 1.2.1, heavy quarkonia production proceeds mainly via gluon fusion, the calculation of the cross section can be performed considering the gg$\rightarrow Q\overline{Q}$ diagram only. The elementary cross section for such

process is[74]:

$$\hat{\sigma}_{gg} = \frac{\pi\alpha_S^2}{3\hat{s}}\left[-\frac{1}{4}\chi(7+31\frac{m_Q^2}{\hat{s}}) + (1+4\frac{m_Q^2}{\hat{s}}+\frac{m_Q^4}{\hat{s}^2})\ln(\frac{1+\chi}{1-\chi})\right] \quad (6.12)$$

where

$$\chi = \sqrt{1-4\frac{m_Q^2}{\hat{s}}} \quad (6.13)$$

As it was pointed out, the above formulae only hold at Leading Order. Next-to-Leading order calculations of total and differential cross sections are available: they were used for the evaluation of the physics performance of the ALICE muon spectrometer in Pb-Pb collisions at 5.5 TeV per nucleon pair and in p-p collisions at 14 TeV (both reported in Ref. [39]), and in p-p collisions at 5.5 TeV (described earlier in this chapter). Such calculations are based on the MRSTHO PDF set. The determination of the scaling factors will be performed according to the same calculations, but the LO equations 6.10 and 6.12 will be used in Sec. 6.3.3 to explore different choices of PDF (and factorisation scheme) in order to evaluate the systematic theoretical uncertainty.

To evaluate the transverse momentum dependence of the scaling factors, the p_T distributions obtained by rescaling the CDF data with the procedure described in Sec. 6.2.1 will be used.

6.3.2 Expected scaling factors

Figures. 6.18 and 6.19 show the NLO rapidity-differential cross sections at 5.5 TeV and 14 TeV, for J/ψ and Υ respectively, in the rapidity interval covered by the muon spectrometer.

The scaling factors for the J/ψ and Υ cross sections are calculated according to Eq. 6.6, recalled here:

$$S = \frac{\sigma_{MS}^{5.5}}{\sigma_{MS}^{14}} = \frac{\int_{2.5}^{4}\frac{d\sigma}{dy}^{5.5}dy}{\int_{2.5}^{4}\frac{d\sigma}{dy}^{14}dy}$$

The results for σ_{MS} and the scaling factors for J/ψ and Υ are shown in Tab. 6.4: according to NLO Color Evaporation Model with the MRSTHO PDF set, the cross section for J/ψ production in the muon spectrometer rapidity window at 5.5 TeV is 63% of the one at 14 TeV, while the same ratio for the Υ amounts to 43%.

Resonance	J/ψ	Υ
$BR_{\mu\mu}\sigma^{5.5}$(nb)	1.83×10^3	12
$BR_{\mu\mu}\sigma^{14}$(nb)	3.18×10^3	28
$BR_{\mu\mu}\sigma^{5.5}_{MS}$ (nb)	0.27×10^3	1.6
$BR_{\mu\mu}\sigma^{14}_{MS}$(nb)	0.43×10^3	3.8
$S = \sigma^{5.5}_{MS}/\sigma^{14}_{MS}$	0.63	0.43

Table 6.4: Cross sections for J/ψ and Υ production in p-p collisions at 5.5 TeV and at 14 TeV and scaling factors between them.

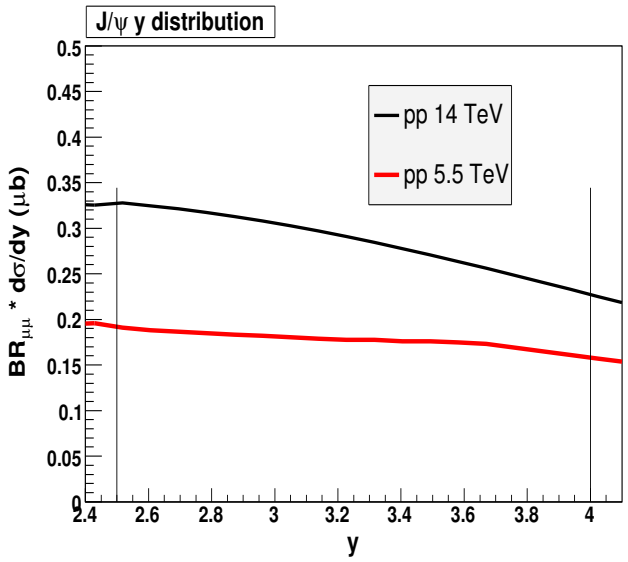

Figure 6.18: Color Evaporation Model J/ψ rapidity-differential cross section at 5.5 TeV and 14 TeV in the ALICE muon spectrometer rapidity window, calculated at NLO with the MRSTHO PDF set (detail from Fig. 6.1).

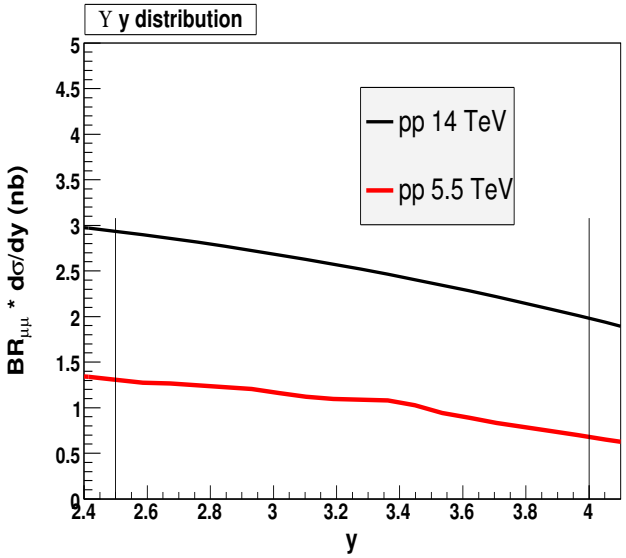

Figure 6.19: Color Evaporation Model Υ rapidity-differential cross section at 5.5 TeV and 14 TeV in the ALICE muon spectrometer rapidity window, calculated at NLO with the MRSTHO PDF set (detail from Fig. 6.2).

Scaling factors in p_T bins

The p_T-dependence of the scaling factors has been evaluated for a few p_T bins.

It has been assumed that the p_T and rapidity dependence of the cross section can be factorised, so that:

$$\frac{d^2\sigma}{dp_T dy} = \frac{d\sigma}{dy}\frac{dN}{dp_T} \tag{6.14}$$

with dN/dp_T normalised to unity, so that:

$$\int_{2.5}^{4} dy \int_{0}^{+\infty} dp_T \frac{d^2\sigma}{dp_T dy} = \int_{2.5}^{4} dy \frac{d\sigma}{dy} \int_{0}^{+\infty} dp_T \frac{dN}{dp_T} = \sigma_{MS} \tag{6.15}$$

and

$$\frac{d\sigma_{MS}}{dp_T} = \sigma_{MS}\frac{dN}{dp_T} \tag{6.16}$$

The values of dN/dp_T can be obtained from the distributions shown in Figs. 6.4 and 6.5, obtained by rescaling the CDF data.

The scaling factor needed in order to rescale from 14 TeV to 5.5 TeV the differential cross section in the p_T bin $[p_{T,1}, p_{T,2}]$ will then be given by

the convolution of the factor $S = \sigma^{5.5}_{MS}/\sigma^{14}_{MS}$ determined above with the ratio between integrals of the p_T distribution in that bin at the two energies:

$$S_{[1,2]} = \frac{\int_{p_{T,1}}^{p_{T,2}} \frac{d\sigma^{5.5}_{MS}}{dp_T} dp_T}{\int_{p_{T,1}}^{p_{T,2}} \frac{d\sigma^{14}_{MS}}{dp_T} dp_T} = \frac{\sigma^{5.5}_{MS}}{\sigma^{14}_{MS}} \frac{\int_{p_{T,1}}^{p_{T,2}} \frac{dN}{dp_T}^{5.5} dp_T}{\int_{p_{T,1}}^{p_{T,2}} \frac{dN}{dp_T}^{14} dp_T} = S \frac{\int_{p_{T,1}}^{p_{T,2}} \frac{dN}{dp_T}^{5.5} dp_T}{\int_{p_{T,1}}^{p_{T,2}} \frac{dN}{dp_T}^{14} dp_T} \quad (6.17)$$

Five p_T bins have been considered. The scaling factors for each p_T bin, for J/ψ and Υ, are shown in Tab. 6.5. Such factors are decreasing with p_T, since the increase in $\sqrt{s}$ populates the high p_T regions (see Figs. 6.3(a) and 6.3(b) in Sec. 6.2.1).

p_T bin (GeV/c)	$S^{J/\psi}$	S^{Υ}
[0,2]	0.81	0.55
[2,4]	0.64	0.51
[4,6]	0.47	0.45
[6,8]	0.38	0.39
[8,20]	0.32	0.33

Table 6.5: Scaling factors from 14 TeV to 5.5 TeV of the cross sections for J/ψ and Υ production, for five p_T bins.

6.3.3 Estimation of theoretical uncertainties

The estimation of the scaling factors is affected by theoretical uncertainties arising from:

- the choice of perturbative QCD parameters such as the renormalisation scale μ_R and the factorisation scale μ_F;
- the non-perfect knowledge of the PDFs.

The aim of this paragraph is to use the Leading Order equations presented in Sec. 6.3.1 to estimate such uncertainties.

Renormalisation scale

The choice of μ_R is hidden in the strong coupling constant α_S in Eq. 6.12: at LO, such constant is an overall factor in front of the cross section, with no or little $\sqrt{s}$-dependence[75], so that its choice is not relevant when computing the ratio between cross sections at different energies.

Gluon distribution functions

The scaling factors have been evaluated at Leading Order for four different choices of LO PDF sets[3]: MRST98[71], MRST01[76], CTEQ5[77], CTEQ6[78]. The Parton Distribution Functions in the proton do not change with $\sqrt{s}$: what changes are the x_1 and x_2 regions corresponding to the ALICE muon spectrometer rapidity window, as shown in Sec. 6.3.1. Since the only diagram included in the calculation presented here is the gluon fusion, the only relevant PDF is the gluon distribution function g(x): the four different choices of g(x) are shown in Fig. 6.20 for the J/ψ (evaluated at $\mu_F = 2m_c$) and in Fig. 6.21 for the Υ (evaluated at $\mu_F = 2m_b$), together with the x_1 and x_2 intervals probed by the two resonances in the ALICE muon spectrometer rapidity window at 5.5 TeV and 14 TeV. The reasons for the choice of μ_F will be explained in the next paragraph.

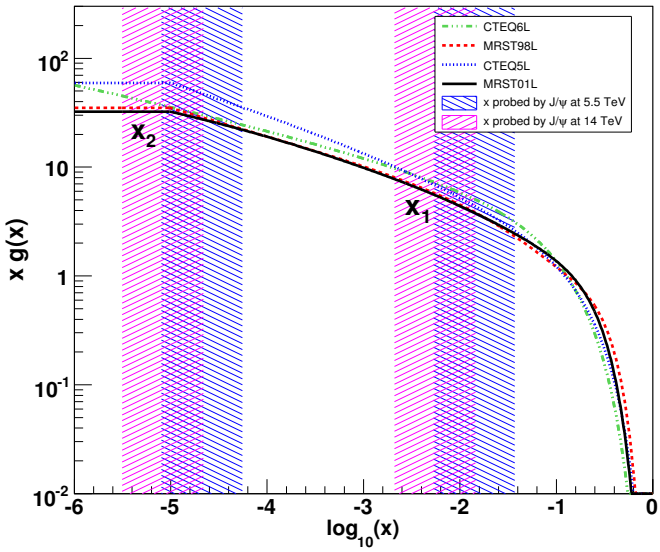

Figure 6.20: LO gluon distribution function in the proton, evaluated at $\mu_F = 2m_c$. The regions of x_1 and x_2 probed by J/ψ in the ALICE muon spectrometer rapidity window at 5.5 TeV and 14 TeV are also shown.

As it is clear from Eq. 6.10, different choices of the PDF lead to different rapidity distributions. The rapidity distributions for J/ψ and Υ obtained with the above gluon distribution functions at the two different energies are

[3]The order of a PDF set is the order of the elementary cross sections $\hat{\sigma}$ that were used in the fitting process for that PDF set.

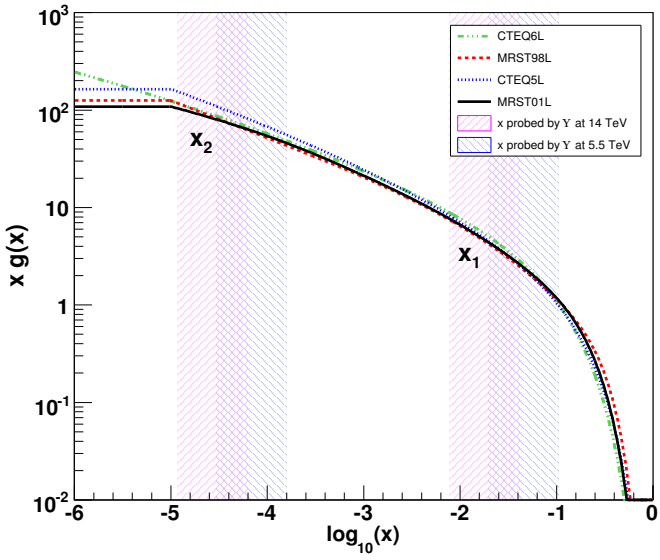

Figure 6.21: LO gluon distribution function in the proton, evaluated at $\mu_F = 2m_b$. The regions of x_1 and x_2 probed by Υ in the ALICE muon spectrometer rapidity window at 5.5 TeV and 14 TeV are also shown.

shown in Figs. 6.22(a) through 6.23(b), compared with the NLO distribution already shown.

To evaluate the uncertainty due to the choice of the PDF, the ratio $\sigma^{5.5}_{MS}/\sigma^{14}_{MS}$ has been computed for the four PDFs. The results are shown in Tab. 6.6; they can be summarised as follows:

PDF	CTEQ5	CTEQ6	MRST98	MRST01
$\sigma^{5.5}_{MS}/\sigma^{14}_{MS}$ for J/ψ	0.52	0.56	0.54	0.56
$\sigma^{5.5}_{MS}/\sigma^{14}_{MS}$ for Υ	0.33	0.35	0.36	0.39

Table 6.6: Scaling factors for the J/ψ and Υ cross section from 14 TeV to 5.5 TeV, calculated at LO with $\mu_F = 2m_Q$, for four different gluon distribution functions.

- the relative spread of the scaling factor for the J/ψ is of about 4%;
- the relative spread of the scaling factor for the Υ is of about 8%;
- the MRST98 LO result for J/ψ (54%) is 14% lower than the MRST NLO result (63%);

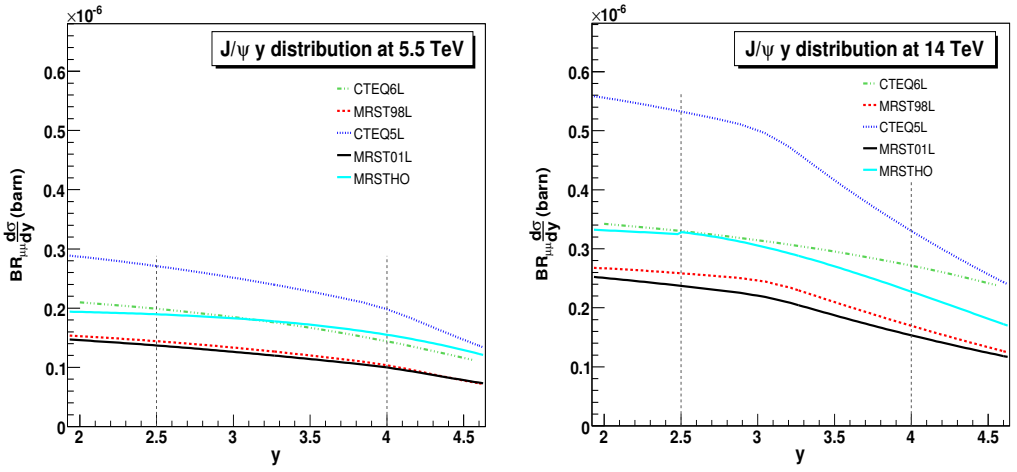

(a) (b)

Figure 6.22: CEM J/ψ rapidity-differential cross section at 5.5 TeV (a) and 14 TeV (b), calculated at LO with four different gluon distribution functions and at NLO with the MRSTHO gluon distribution function.

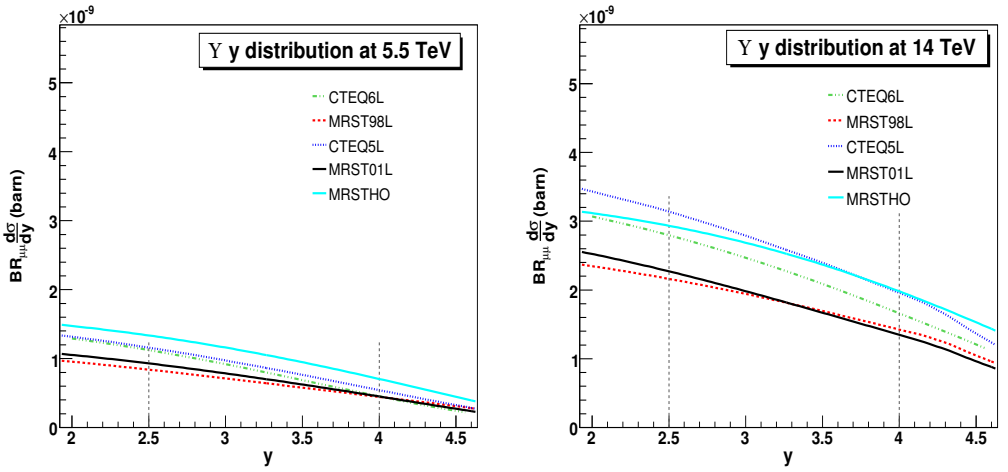

(a) (b)

Figure 6.23: CEM Υ rapidity-differential cross section at 5.5 TeV (a) and 14 TeV (b), calculated at LO with four different gluon distribution functions and at NLO with the MRSTHO gluon distribution function.

- the MRST98 LO result for Υ (36%) is 16% lower than the MRST NLO result (43%).

The relative spread reported above is defined as half the difference between the maximum and minimum value, divided by the mean value.

No PDF or scale dependence of the p_T distribution has been included in the present work: this is a consequence of the fact that the p_T distributions adopted have been obtained from experimental results (though rescaled according to CEM predictions), and not from a theoretical calculation. The relative spread of the scaling factor when varying the PDF is the same for all p_T bins.

Factorisation scale

The factorisation scale μ_F appears in the cross section as an argument of the Parton Distribution Functions f(x,μ^2), setting the scale at which such functions are evaluated. When studying some physics process, the PDF should be evaluated at a scale compatible with the energies and masses involved in the process: for example, the scale at which the J/ψ is produced is of the order of the charm quark mass, while the scale at which the Υ is produced is of the order of the beauty quark mass. The NLO calculations that were used throughout this work to evaluate quarkonia cross sections use μ_F=2m$_c$=2.4 GeV for the J/ψ and μ_F=2m$_b$=9.0 GeV for the Υ, since such choices give the best agreement with the available data at lower energies[69, 40]. To be consistent with this, the LO calculations carried out in the previous paragraph to evaluate the uncertainty due to the choice of the PDF assume a scale of twice the heavy quark mass. Nevertheless, some more information can be obtained by varying μ_F, because the scale dependence of results in perturbative QCD can be used to evaluate the theoretical uncertainties on the results themselves.

To evaluate the effect of the factorisation scale on the scaling factor, the ratio $\sigma^{5.5}_{MS}/\sigma^{14}_{MS}$ has been calculated as a function of μ_F for each gluon distribution function: the results are shown in Figs. 6.24 and 6.25. The dots of different colours mark the points of the curves corresponding to a scale of twice the heavy quark mass[4] on one hand and to a scale of twice the D (B) meson mass for the J/ψ (Υ) on the other hand: these are the limits of the $\hat{s}$ integration in Eq. 6.10 and correspond to the most reasonable interval for the choice of the scale. It is clear from the figures that within such interval, for all the curves, the ratio has a very weak dependence on the scale, the dominant uncertainty being the one related to the choice of the

[4]The heavy quak mass adopted for the fitting process is different from collaboration to collaboration.

gluon distribution function. It is interesting to note that the cross sections at 5.5 TeV and at 14 TeV have a strong dependence from the scale (Figs. 6.26(a) and 6.26(b)), which seems to cancel out when considering the ratio between the two.

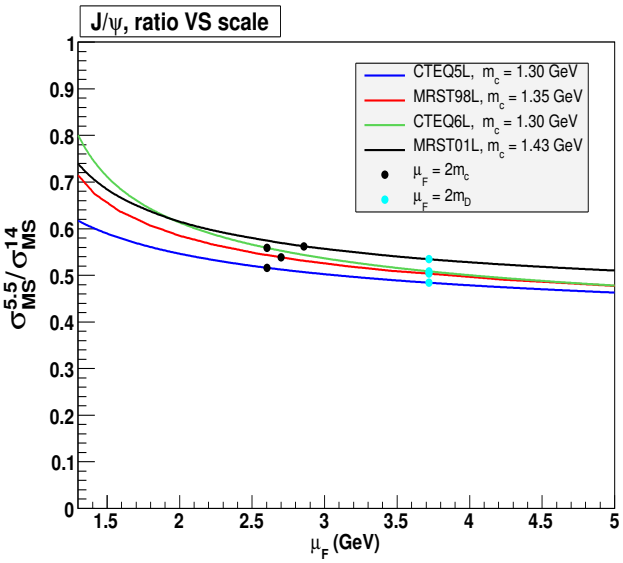

Figure 6.24: Scaling factor for the J/ψ cross section from 14 TeV to 5.5 TeV, as a function of the factorisation scale μ_F, calculated at LO for four different gluon distribution functions.

Conclusions

To summarise the results of this section, the scaling factors in p_T bins obtained in Sec. 6.3.2 have been compared with the LO results reported in this section (Figs. 6.27 and 6.28). The large discrepancy between Next-to-Leading and Leading Order makes it difficult to evaluate the systematic error due to the choice of the PDF by means of LO results. If one assumes that the spread obtained at LO with different PDFs remains unchanged at NLO, the error can be estimated by taking the LO relative spread as a relative error for the NLO result, thus obtaining for the p_T-integrated scaling factors:

$$S_{J/\psi} = 0.63 \pm 4\% = 0.63 \pm 0.03; \quad S_{\Upsilon} = 0.43 \pm 8\% = 0.43 \pm 0.03$$

The J/ψ scaling factor reported here only refers to prompt J/ψ. Since the ALICE muon spectrometer can not distinguish between prompt and

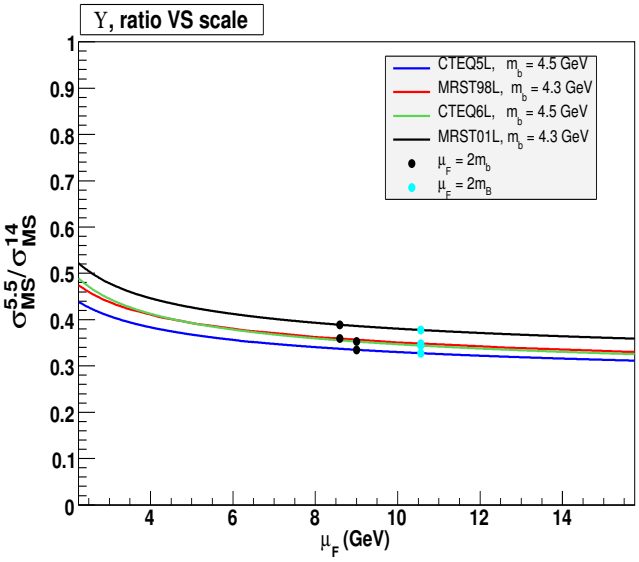

Figure 6.25: Scaling factor for the Υ cross section from 14 TeV to 5.5 TeV, as a function of the factorisation scale μ_F, calculated at LO for four different gluon distribution functions.

non-prompt J/ψ, an analogous scaling factor shall be determined for the non-prompt J/ψ contribution.

It has to be pointed out that the uncertainties discussed here may be reduced once p-p data at 14 TeV are available: the measurement of the total cross section shall tell how reliable are the NLO calculations used to estimate both the physics performance of the ALICE muon spectrometer and the scaling factors, while the measured shape of the rapidity distribution may constrain the choice of the PDF set[40], thus reducing the spread reported above.

Finally, it is interesting to compare the relative spread obtained for the scaling factors with the precision expected for the measurement of the beam luminosity (and, consequently, of the cross section): the present methods based on beam currents and profiles[79] achieve a precision of about 10%, while more refined methods[80] are under development, that aim at improving the precision to about 5%: the uncertainty on the scaling factor obtained in this section (4% for the J/ψ and 8% for the Υ) is roughly compatible with such values.

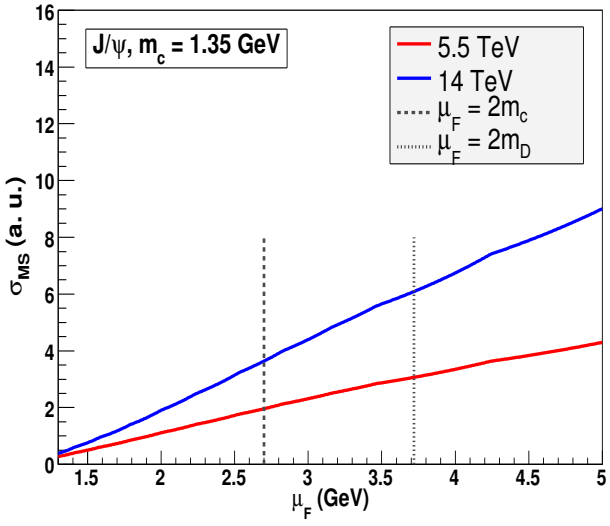

(a)

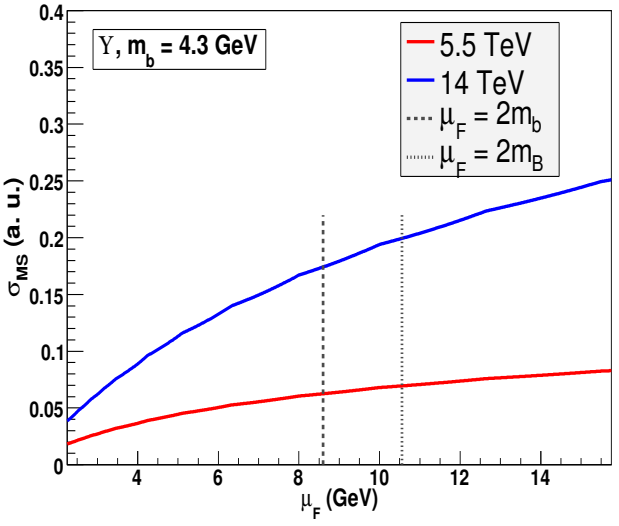

(b)

Figure 6.26: Cross section for J/ψ (a) and Υ (b) production in the ALICE muon spectrometer rapidity window in p-p collisions at 5.5 TeV and 14 TeV, as a function of the factorisation scale μ_F, calculated at LO with the MRST98 gluon distribution function. The vertical bars represent the values of μ_F corresponding to twice the charm (beauty) quark mass and to twice the D (B) meson mass for the J/ψ (Υ).

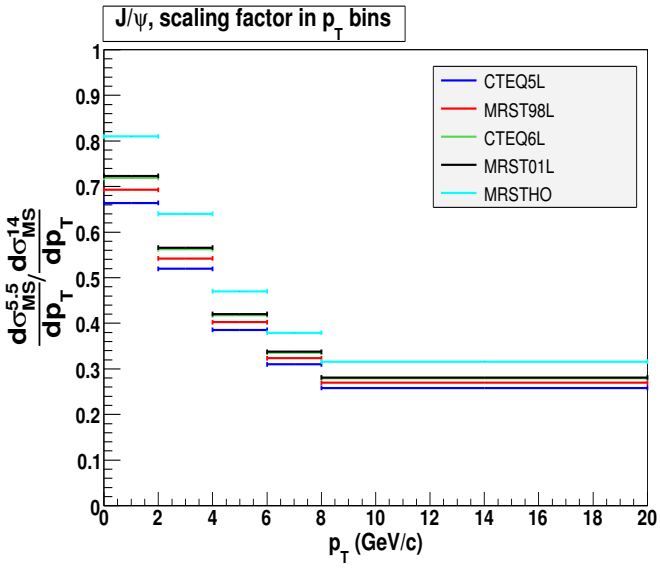

Figure 6.27: Scaling factor for the J/ψ p_T-differential cross section from 14 TeV to 5.5 TeV, calculated at LO with four different gluon distribution functions and at NLO with the MRSTHO gluon distribution function.

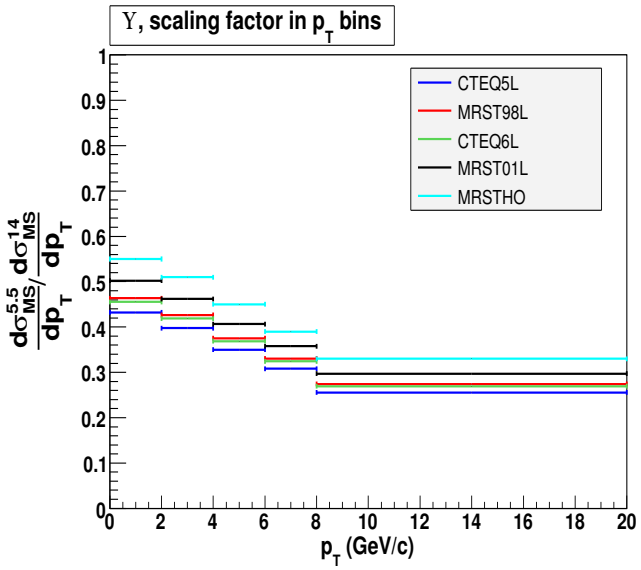

Figure 6.28: Scaling factor for the Υ p_T-differential cross section from 14 TeV to 5.5 TeV, calculated at LO with four different gluon distribution functions and at NLO with the MRSTHO gluon distribution function.

Conclusions

Trigger detectors

All the Resistive Plate Chambers produced for the trigger system of the ALICE muon spectrometer have been fully characterised by means of extensive tests, including:

- the detection of construction imperfections;
- the measurement of current, mean and local noise rate;
- the local measurement of efficiency as a function of voltage in cells of 20×20 cm^2 and at working voltage in cells of 2×2 cm^2.

All data have been stored in a database for future reference.

Selection criteria have been applied to the tested detectors, requiring an uniform efficiency throughout the whole surface, a good uniformity in the parameters of the efficiency curves, reasonable current and mean noise rate values, a limited number of localised noisy spots. According to these criteria and to the number of required detectors for each of the typologies described in Chap. 2, 17% of the detectors have been discarded, 26% of the detectors have shown sufficient performances allowing them to be used in ALICE in the most peripheral regions of the trigger system or as spare detectors, 57% of the detectors have shown good or excellent performances. The detectors assigned to the third of the above mentioned quality classes have shown:

- only very small (if any) imperfections in the efficiency map;
- mean noise rate lower than 0.4 Hz/cm^2;
- less than 7 noisy spots with rate higher than 20 Hz/cm^2;
- voltage range in which all 20×20 cm^2 cells reach 50% efficiency < 400 V;
- current drawn per surface unit smaller than 0.5 nA/cm^2.

The 72 final detectors are now installed in ALICE. A good number of spare detectors has also been selected. A future production session will provide more spare detectors in order to achieve a safe number of spares for all detector typologies.

Finally, tests carried out on detector prototypes which had been previously aged by means of long irradiation periods have shown no significant alteration of their performances.

Quarkonia detection in p-p collisions

The performances of the ALICE muon spectrometer for J/ψ and Υ detection in proton-proton collisions at $\sqrt{s}$=5.5 TeV in a run of 10^6 s have been evaluated by means of simulation, using NLO Color Evaporation Model parametrisations for the cross sections. According to the simulation, 2.8% (3.6%) of muon pairs from J/ψ (Υ) emitted over all the phase space will be detected in the muon spectrometer. The expected number of J/ψ (Υ) is about 150000 (1300). The p_T-differential cross sections for J/ψ (Υ) can be measured in fine bins (1$\div$2 GeV/c) with statistical error lower than 8% (10%) up to 15 (10) GeV/c. The rapidity-differential J/ψ (Υ) cross sections can be measured for $2.5< y <4$ in bins of 0.1$\div$0.2 (0.2$\div$0.5) rapidity units with statistical error smaller than 2% (8%). Such results only refer to the analysis of signal. If a p-p run at $\sqrt{s}$=5.5 TeV at the LHC becomes more than a hypothesis, a more refined study will be needed, taking into account background subtraction and, for J/ψ, the feed-down from the decay of open beauty mesons.

Since the above-discussed p-p run at 5.5 TeV is not in the present LHC schedule, the scaling factors which shall be used to extrapolate the quarkonia cross sections in the muon spectrometer acceptance from those obtained in p-p at 14 TeV have been evaluated. These factors resulted to be 0.63 for J/ψ and 0.43 for Υ. The extrapolation has also been performed for different p_T bins. These results have been obtained with available NLO parametrisations of the rapidity-differential cross sections, according to the Color Evaporation Model (CTEQ5, CTEQ6, MRST98, MRST01). The uncertainty on such values has been evaluated by performing the extrapolation for different choices of the Parton Distribution Function set, and by varying the factorisation scale used in the calculation. This has been done at Leading Order. The uncertainty related to the factorisation scale seems to be negligible with respect to that introduced by the PDF. The relative spread of the results obtained with different PDFs is 4% for J/ψ and 8% for Υ. For both resonances, a 15% discrepancy between NLO and LO results was found. A more refined study may be carried out by using NLO parametrisations with different PDF choices.

Appendix A

Statistical error on efficiency measurements

The error on the efficiency measurements presented in Chap. 4 is computed according to Eq. 4.5, recalled here:

$$\sigma_\epsilon = \frac{\sigma_{n_{detected}}}{n} = \sqrt{\frac{\epsilon(1-\epsilon)}{n}} \tag{A.1}$$

Such expression accounts for the statistical fluctuations of the number of detected events ($n_{detected} = \epsilon n$), according to the Bernoulli statistics. These fluctuations are estimated with the second momentum $\sqrt{n\epsilon(1-\epsilon)}$ of a binomial distribution of parameters n and ϵ.

Nevertheless, when statistical fluctuations decrease below the sensitivity error of the instrument used for the measurement, they no longer represent the main source of error: for example, when measuring distances repeatedly with a, say, 1 mm resolution, the standard deviation of the distribution of the values should be quoted as error only if it exceeds 1 mm.

In this case, the efficiency is measured by counting particles, i.e. with a resolution of ± 1 on $n_{detected}$, resulting in a resolution of $\pm 1/\mathrm{n}$ on the efficiency. The quantity 1/n can thus be taken as a sensitivity error on the measurement.

The condition for the error defined in Eq. A.1 to be reliable can thus be written as:

$$1/n < \sqrt{\frac{\epsilon(1-\epsilon)}{n}} \tag{A.2}$$

In Fig. A.1, the region of the (n,ϵ) plane where the condition A.2 is respected is shown. It emerges clearly that, for a given efficiency, there is a minimum number of events below which the dominant error is the sensitivity error. Vice versa, at fixed number of events, there is a maximum efficiency

value the error on which can be estimated with Eq. A.1. As pointed out in Sec. 4.2.2, the number of events in the most peripheral cells in the efficiency maps at working HV is about 50: in this case, Eq. A.1 holds for ϵ <98%. This condition is respected in most cases. In those case in which it is not, the sensitivity error 1/n (2% with 50 events) should be quoted.

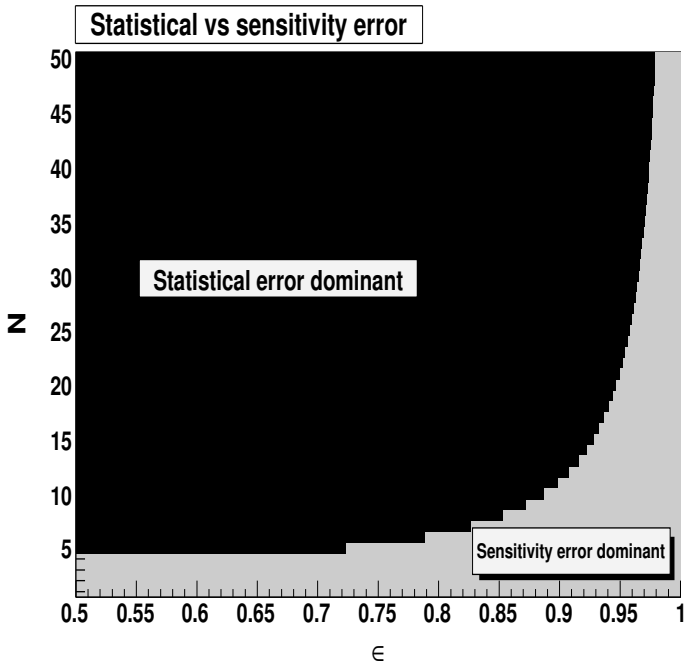

Figure A.1: The efficiency-events plane. The darker region is the one in which the condition A.2 is respected and the statistical error is dominant.

Acknowledgements

I acknowledge constant advice and encouragement from my thesis director Prof. Ermanno Vercellin. I also thank my referee Dr. Hervé Borel for careful reading of the thesis.

I acknowledge fruitful discussions with L. Magnea from the Theoretical Physics Department in Torino.

I would like to thank all the physicists and engineers at the INFN and Experimental Physics Department in Torino for constant support throughout the three years of my Ph. D. cycle: R. Arnaldi, E. Chiavassa, P. Cortese, G. Dellacasa, N. De Marco, A. Ferretti, M. Gallio, R. Gemme, P. Mereu, A. Musso, C. Oppedisano, A. Piccotti, F. Poggio, E. Scomparin, D. Stocco, G. Travaglia and F. Yermia.

I also acknowledge excellent technical support from the technicians at INFN Torino: G. Alfarone, O. Brunasso and R. Farano.

Grazie

Anche se l'ho già fatto nella versione inglese e ufficiale dei ringraziamenti, rinnovo la mia stima e gratitudine per il Prof. Ermanno Vercellin che mi ha seguito e allo stesso tempo guidato per tutta la durata della tesi. Ringrazio lui e tutto il gruppo Pinot anche per la vicinanza mostratami in momenti umanamente difficili.

Ringrazio fragorosamente papà e mamma per un'infinità di cose che scrivere non si può.

Grazie poi a tutto il resto della mia amata famiglia a Torino e a Fabriano.

Grazie a Stefania che rende tutto quanto migliore, ai miei boyz di sempre Diego, Nico, Ale, Fra, anche se siete palesemente tutti invecchiati e lavorate (o così dite) troppo, so che ci siete. Grazie a un paio di sporche dozzine di fisici passati presenti o futuri, di cui cito Steo e Pier solo per vistosa anzianità, vi elencherei tutti ma se non mi sbrigo il tipo(grafo) non mi rilega la tesi in tempo e poi i ringraziamenti me li leggo io da solo nel buio della mia stanzetta mentre gli altri dottorandi festeggiano con le pizzette che ha preparato mia madre. Grazie alla brigata del calcetto pre-aperitivo, anche se nessuno torna mai a coprire e io devo ammuffire nella mia metà campo, salvo poi farmi cazziare se, frustrato, provo qualche accelerazione di quelle che già ci fecero vincere i mondiali '58, '62,'70.

Grazie a mia mamma per i due punti della patente che si è accollata al posto mio.

Grazie a tutti.

Bibliography

[1] L. McLerran *RHIC Physics: The Quark Gluon Plasma and The Color Glass Condensate: 4 Lectures.* arXiv:hep-ph/0311028v1 3 Nov 2003

[2] U. Heinz, *From SPS to RHIC: Breaking the Barrier to the Quark-Gluon Plasma* arXiv:hep-ph/0109006v1 2 sep 2001

[3] F. Karsch (for the RBC-Belefield Collaboration), *Transition temperature in QCD with physical light and strange quark masses.* Journal of Physics G: Nucl. and Part. Phys. 34 No 8 (2007) S627-S630

[4] F. Karsch (for the RBC-Belefield Collaboration), *Transition temperature in QCD.* Presentation at *Quark Matter 2006*, Shanghai 14-20 Nov 2006 http://www.sinap.ac.cn/qm2006/

[5] For a review see L. McLerran *The Color Glass Condensate and Small x Physics: 4 Lectures.* arXiv:hep-ph/0104285v2 27 Apr 2001

[6] J. D. Bjorken, *Highly relativistic nucleus-nucleus collisions: The central rapidity region.* Physical Review D 27 (1983) 140-151

[7] J. Schukraft, *Little bang at big accelerators: Heavy ion physics from AGS to LHC.* Nucl. Phys. B 75 (1999) 46-53

[8] L. Maiani, *Towards a new state of matter* arXiv:hep-ph/0602113v1 13 Feb 2006

[9] M. Gyulassy and L. McLerran, *New forms of QCD matter discovered at RHIC.* Nucl. Phys. A 750 (2005) 30-63

[10] J. Rafelski and J. Letessier, *Strangeness and Quark Gluon Plasma.* J. Phys. G 30 (2004) S1-S28 arXiv:hep-ph/0305284

[11] D. Elia et al., *Strange particle production in 158 and 40 A GeV/c Pb-Pb and p-Be collisions.* J. Phys. G31 (2005) S135-S140

[12] R. Rapp and J. Wambach, *Chiral Symmetry Restoration and Dileptons in Relativistic Heavy-Ion Collisions.* Adv.Nucl.Phys. 25 (2000) 1 arXiv:hep-ph/9909229v1 2 Sep 1999

[13] R, Arnaldi et al., *First Measurement of the ρ Spectral Function in High-Energy Nuclear Collisions.* Phys. Rev. Lett. 96 (2006) 162302

[14] F. Abe et al., *J/ψ and $\psi(2S)$ production in $p\overline{p}$ collisions at $\sqrt{s}$=1.8 TeV.* Phys. Rev. Lett. 79 (1997) 572

[15] V.D.Barger et al., *On ψ and Υ production via gluons.* Phys. Lett. B 91 (1980) 253-258

[16] R. Gavai et al., *Quarkonium production in hadronic collisions.* Int. J. Mod. Phys. A 10 (1995) 3043-3070

[17] G. T. Bodwin et al., *Rigorous QCD Analysis of Inclusive Annihilation and Production of Heavy Quarkonium.* Phys. Rev. D 51 (1995) 1125-1171

[18] T. Matsui and H. Satz, *J/ψ suppression by quark-gluon plasma formation.* Physics Letters B 178 (1986) 416-422

[19] H. Satz, *Quarkonium Binding and Dissociation: The spectral Analysis of the QGP.* Nucl. Phys. A 783 (2007) 249c-260c

[20] For a review, see P. Shukla, *Glauber model for heavy ion collisions from low energies to high energies.* arXiv:nucl-th/0112039v1 13 Dec 2001

[21] M. C. Abreu et al., *J/ψ, ψ' and Drell-Yan production in S-U interactions at 200 GeV per nucleon.* Phys. Lett. B 449 (1999) 128

[22] M. C. Abreu et al., *The production of J/psi in 200 GeV/nucleon oxygen-uranium interactions.* Phys. Lett. B 220 (1989) 471

[23] M.C. Abreu et al., *Anomalous J/ψ suppression in Pb-Pb interactions at 158 GeV/c per nucleon.* Phys. Lett. B 410 (1997) 337-343

[24] E. Scomparin for the NA60 collaboration, *J/ψ production in In-In and p-A collisions.* J. Phys. G: Nucl. Part. Phys. 34 (2007) S463-S469

[25] M. Leitch, *RHIC results on J/ψ.* J. Phys. G: Nucl. Part. Phys. 34 (2007) S453-S462

[26] *The Large Hadron Collider Accelerator Project.* CERN/AC/93-03 (LHC) 1993

[27] *LHC design report.* http://ab-div.web.cern.ch/ab-div/Publications/LHC-DesignReport.html

[28] *ALICE-Technical Proposal.* CERN/LHCC-95-71 LHCC/P3, 15 Dec. 1995

[29] *ALICE - Technical Design Reports* http://alice.web.cern.ch/Alice/TDR

[30] *The forward muon spectrometer.* Addendum to the *ALICE Technical Proposal.* CERN LHCC-96-32; LHCC/P3-Addendum 1, 15 Oct. 1996

[31] M.P. Comets et al.,*Results of the In-Beam tests performed with the Quadrant 0 of station 1 for the ALICE Dimuon Arm* ALICE-INT-2003-035 v.3

[32] M. Boudjemline et al.,*Results of Slat CPC Prototype Test for ALICE Dimuon Spectrometer* ALICE-INT-2002-023 v1.0

[33] *Expérience ALICE pour l'étude des collisions d'ions lourds ultra-relativistes au CERN-LHC.* Ph.D. thesis Université B. Pascal Clermont-Ferrand PCCF T 0305

[34] *Technical Design Report of the Dimuon Forward Spectrometer.* CERN/LHCC 99-22 13 Aug 1999

[35] O.Roig et al., *Description and optimisation of the ALICE dimuon trigger.* ALICE-INT-1998-08

[36] R. Arnaldi et al., *A dual threshold technique to improve the time resolution of resistive plate chambers in streamer mode.* Nucl. Instr. and Meth. A 457 (2001) 117-125

[37] *ALICE Technical Design Report on Trigger, Data Acquisition, High-Level Trigger, Control system* CERN/LHCC/2003-062 7 Jan 2004

[38] P. Dupieux et al., *ALICE Muon Trigger Performance* ALICE-INT-2006-002

[39] ALICE collaboration, *ALICE: Physics Performance Report, Volume II* Journal of Physics G: Nucl. Part. Phys. 32 (2006) 1295-2040

[40] R. Guernane et al., *Quarkonia detection with the ALICE muon spectrometer in p-p collisions at* $\sqrt{s}$ *= 14 TeV.* ALICE-INT-2006-029

[41] L. Aphecetche et al., *Production of $W^{\pm}$ vector bosons in p+p and Pb+Pb collisions at LHC energies. $W^{\pm}$ detection in the ALICE muon spectrometer.* ALICE-INT-2006-021

[42] R. Santonico and R. Cardarelli, *Development of resistive plate counters.* Nucl. Instr. Meth. 187 (1981) 377-380

[43] R. Cardarelli et al., *Progress in resistive plate counters.* Nucl. Instr. Meth. A 263 (1988) 20-25

[44] Y. Pestov, *Status and future developments of spark counters with a localized discharge.* Nucl. Instr. and Meth. 196 (1982) 45-47

[45] M. Angelone et al., *Test of a resistive plate chamber under irradiation of photons and neutrons.* Nucl. Instr. and Meth. A 355 (1995) 399-405

[46] M. Bertino et al.,*Performance of resistive plate counters at beam flux up to 140 Hz/cm^2.* Nucl. Instr. and Meth. A 283 (1989) 654-657

[47] M. Iori and F. Massa, *Performance of a resistive plate counter at high ionization rates.* Nucl. Instr. and Meth. A 306 (1991) 159-168

[48] I. Crotty et al., *The non-spark mode and high rate operation of resistive parallel plate chambers.* Nucl. Instr. and Meth. A 337 (1994) 370-381

[49] R. Cardarelli et al., *Performance of a resistive plate chamber operating with pure CF_3Br.* Nucl. Instr. and Meth. A 333 (1993) 399-403

[50] I. Duerdoth et al., *The transition from proportional to streamer mode in a resistive plate chamber.* Nucl. Instr. and Meth. A 348 (1994) 303-306

[51] R. Arnaldi et al., *A low-resistivity RPC for the ALICE dimuon arm.* Nucl. Instr. and Meth. A 451 (2000) 462 - 473

[52] R. Arnaldi et al., *Front-End Electronics for the RPCs of the ALICE Dimuon Trigger.* IEEE Trans.on Nucl. Sc. 52-4 (2005) 1176-1181

[53] R. Arnaldi et al., *Spatial resolution of RPC in streamer mode.* Nucl. Instr. and Meth. A 490 (2002) 51-57

[54] R. Arnaldi et al., *Beam and ageing tests with a highly saturated avalanche gas mixture for the ALICE p-p data taking.* Nucl. Phys. B 158 (2006) 149-153

[55] S. Agosteo et al., *A facility for the test of large area muon chambers at high rates.* Nucl. Instr. Meth. A 452 (2000) 94-104

[56] R. Arnaldi et al., *Ageing tests on the low-resistivity RPC for the ALICE dimuon arm.* Nucl. Instr. and Meth. A 508 (2003) 106-109

[57] R. Arnaldi et al., *Ageing tests and gas analysis on Resistive Plate Chambers for the trigger of the ALICE dimuon arm.* Nucl. Instr. and Meth. A 533 (2004) 112-115

[58] R. Guernane et al., *Machine Induced Background in the ALICE Muon Trigger System in p-p data taking.* ALICE-INT-2003-d.v. 1.0.

[59] F. Yermia, *Machine Induced Background in the ALICE Muon Trigger System in pp Data taking.* Secondo Convegno Nazionale sulla Fisica di ALICE - Vietri s. M. - May 30 - June 1 2006 http://alicemeeting.sa.infn.it/Yermia.ppt

[60] R. Arnaldi et al., *R&D on RPC for the muon trigger system for the ALICE experiment in view of p-p data taking.* IEEE Nucl. Sc. Symp. Conf. Rec. 2 (2004) 1265-1269 Vol. 2

[61] CERN ALICE DAQ Group, *ALICE DATE User's guide.* ALICE-INT-2000-31 v.2.

[62] R. Arnaldi et al., *Overview on production and fast results of the tests on the RPCs for the ALICE dimuon trigger.* Nucl. Phys. B 158 (2006) 83-86

[63] *OPERA Experiment Proposal*, CERN/SPSC 2000-028

[64] D. Stocco, *Strategy for trigger efficiency determination from data.* The 4^{th} DiMuonNet, http://www-dapnia.cea.fr/Sphn/Alice/DiMuonNet

[65] R. Arnaldi et al., *Influence of temperature and humidity on bakelite resistivity.* Nucl. Instr. and Meth. A 456 (2000) 140-142

[66] *First ALICE detectors installed*, CERN Bulletin 37 (2006)

[67] *ROOT: an object-oriented data analysis framework.* http://root.cern.ch

[68] *The ALICE Offline project.* http://aliceinfo.cern.ch/Offline

[69] R. Vogt, *Update on Quarkonium Production Baselines.* CERN Theory Workshop on Hard Probes in Heavy Ion Collisions, http://nuclear.ucdavis.edu/present/vogt/cern_yr3.ps

[70] H.U. Bengsson and T. Sjöstrand, *The Lund Monte Carlo for hadronic processes - PYTHIA version 4.8.*, Computational Physics Communications 46-1 (1987) 43-82

[71] A. D. Martin et al., *Parton distributions: a new global analysis.* arXiv:hep-ph/9803445v2 21 Apr 1998

[72] D. Acosta et al, *Measurement of the J/ψ meson and b-hadron production cross sections in p-$\bar{p}$ collisions at $\sqrt{s}$ = 1960 GeV.* arXiv:hep-ex/0412071v1 27 Dec 2004

[73] A. Accardi et al., *Hard Probes in Heavy Ion Collisions at the LHC: PDFs, Shadowing and pA collisions.* arXiv:hep-ph/0308248v1 25 Aug 2003

[74] B.L. Combridge, *Associated Production of Heavy Flavor States in pp and $p\overline{p}$ Interactions: some QCD Estimates.* Nucl. Phys. B 151 (1979) 429

[75] L. Magnea, *private conversation.*

[76] A. D. Martin et al., *NNLO global parton analysis.* arXiv:hep-ph/0201127v1 14 Jan 2002

[77] H. L. Lai et al., *Global QCD Analysis of Parton Structure of the Nucleon: CTEQ5 Parton Distributions.* arXiv:hep-ph/9903282v3 6 Aug 1999

[78] J. Pumplin et al., *New Generation of Parton Distributions with Uncertainties from Global QCD Analysis.* arXiv:hep-ph/0201195v3 3 Feb 2002

[79] M. W. Krasny et al., *Luminosity Measurement for LHC: the theoretical precison and the experimental challenges.* arXiv:hep-ph/0610052v1 17 Oct 2006

[80] V. A. Khoze et al., *Luminosity Monitors at the LHC.* European Physics Journal C19 (2001) 313-322